Dynamics of a quasigeostrophic Antarctic Circumpolar Current

Louis-Philippe Nadeau

Doctor of Philosophy

Department of Atmospheric and OceanicSciences

McGill University

Montréal,Québec

Octobrer, 2010

A thesis submitted to McGill University in partial fulfillment of the requirements of the degree of Doctor of Philosophy

DEDICATION

Cette thèse est dédiée simultanément à Sébastien Théberge, un grand ami qui nous a quitté en cours de route, ainsi qu'à mon père, Raymond Nadeau, un modèle à qui je dois tant.

CONTRIBUTIONS OF AUTHORS

Chapter 2 is based on a paper published in Journal of Physical oceanography. Chapter 3 is based on a paper to be submitted to Journal of Physical oceanography shortly after this thesis is submitted. Chapter 4 is based on a paper that is in preparation. All articles are co-authored with David Straub. In all articles, I am responsible for the model development and I also performed all the simulations. Frequent discussions with my supervisor, David Straub, helped me significantly through this work. He also participated in the writing of the papers.

REMERCIEMENTS

En premier lieu, j'aimerais remercier mon superviseur, David Straub. David est tout d'abord un très bon ami sur lequel j'ai pu compter pour faire face aux tempêtes qui ont parsemé la route sinueuse et parfois même quelque peu aléatoire menant à la finalisation de ce manuscrit. Ses conseils sont toujours pertinents et éclairants. Sa vision singulière de l'océanographie physique est une source d'inspiration pour moi. J'ai beaucoup apprécié notre collaboration et j'espère bien la poursuivre dans l'avenir. Je tiens aussi à remercier les membres de mon comité pour leur contribution à cette thèse de doctorat: David Marshall, Peter Bartello, Jacques Derome, et sans oublier Bruno "Content" Tremblay que je remercie au passage pour ses conseils et son amitié qui m'est cher. Merci beaucoup à David Holland qui m'a permis de finir cette thèse au CIMS à New York. Le climat général à McGill n'aurait pas été aussi agréable sans la présence des "great fellooows" ou "les boys", des amis de tous les instants: Jean-François "Beaudoin" Lemieux, Jan "la chose c'est que" Sedlacek et William "the corporate" Sacher. Cela s'applique tout autant aux autres amis ayant "fait leur temps" à McGill: Amal, Farid, Alex, Julie, David Hhhhuard, Barbara.. euh non.. Barbie!, Thomas "la comète polonaise", Maria "Abracadabramowicz" et Jing "Tonic!" Yang que je remercie au passage pour la traduction chinoise de mon abrégé. Je désire aussi remercier tous les secrétaires et le personnel du département qui s'est renouvelé à un rythme étourdissant au cours de mon doctorat. Un immense merci à Michael Havas, sans qui j'en serais probablement encore à ma première simulation. Je remercie tous mes proches amis pour leur soutient inaliénable et leur source de

“plaaèisir”: Alexis, Gus, Louis, Étienne, Max, Daniel, Jérôme, Laurence, Gabrielle, Élodie, Alexandra, Julie, François Fauteux, François Lemieux, Dominique, Josiane, Nini et plus particulièrement Ceci. Un énorme merci à mes parents, Normande et Raymond, à mon frère Pierre-Olivier et son amoureuse Valérie ainsi qu’à toute la famille élargie. Merci finalement à Véro pour ton amour intense et inspirant.

ABSTRACT

The idea that basin-like dynamics may influence or control the Antarctic Circumpolar Current (ACC) is investigated with idealized analytic and numerical models. A simple 2-layer analytic model is developed to predict the transport evolution with the wind stress amplitude. At very low forcing, a non-zero minimum is predicted. This is followed by two distinct dynamical regimes for stronger forcing: a linearly increasing Stommel regime and a saturation regime in which the transport ceases to increase. The vertical distribution of the flow obtained using the geometry of the geostrophic contours (or characteristics) is key to predicting the occurrence of this transport saturation.

Many eddy-permitting numerical simulations in large domains are carried over a wide range of parameters. The simulations using a reference zonal wind stress profile agree qualitatively with the analytic model. However, quantitative discrepancies are observed in the saturation regime: i) when a topographic continental ridge is added along the western boundary and ii) when the bottom drag is varied. When a continental ridge is added, eddy fluxes associated with zonal jets enhance the bottom layer recirculation and lower the saturation transport values. When the bottom drag is increased, the lower layer recirculation is suppressed, and this increases the saturation transport values.

Experiments investigating the relative roles of the wind stress and wind stress curl in Drake Passage latitudes are also carried out. It is found that the transport is increased when adding a significant constant wind stress. In this regime dominated

by the wind stress itself, there is an offset between the numerical results and what is predicted by the analytic model. The vertical momentum flux by mesoscale eddies can be used to distinguish between different regimes: an upward momentum transfer is observed when the dynamics is dominated by the wind stress curl and a downward flux is observed when it is not. In the regime where the wind stress curl dominates, Sverdrup circulation applies over most of the domain — even in absence of meridional barriers. Also in this regime, transport is saturated, as suggested by the analytic model.

The analytic model is also generalized to a continuous stratification and numerical experiments varying the vertical resolution are carried out to test its robustness. These simulations show that the 2-layer and 5-layer models give equivalent results when inertial effects are weak. However, in the 5-layer simulations, topographically-driven inertial recirculations blocking Drake Passage reduce the transport when inertial effects are strong. This behavior disapears, however, when realistic topography is used. In this context, the numerical results agree well with the predictions of the analytic model. It is also found that when the wind stress curl dominates, meridional walls play an important role in the dynamics at weak forcing but become less and less important as the forcing increases.

ABRÉGÉ

Dans cette thèse, on étudié l'idée qu'une circulation de type bassin peut influencer et contrôler la dynamique du Courant Circumpolaire Antarctique (CCA) à l'aide de modèles analytique et numérique. Dans un premier temps, on développe un modèle analytique simple à deux couches pour estimer l'évolution du transport en fonction de l'amplitude du vent appliqué à la surface. À très faible amplitude, ce modèle prévoit un transport minimum non-nul. Deux régimes dynamique distincts succèdent à ce minimum: un régime de type "Stommel", dans lequel le transport augmente linéairement et un régime de "saturation" dans lequel le transport plafonne. On utilise la géométrie des "contours géostrophiques", pierre angulaire de la théorie, pour obtenir la distribution verticale de la circulation et estimer l'occurrence de ce régime de saturation.

On effectue ensuite un grand nombre de simulations numériques à haute résolution spatiale, en variant la plupart des paramètres du modèle afin de tester la théorie analytique. On définit un profil de vent "référence" soufflant vers l'est suivant une fonction $\sin^2(y)$, où y est la latitude. Les simulations utilisant ce profil de référence correspondent qualitativement aux prévisions de la théorie analytique. Par contre, on observe des différences quantitatives dans le régime saturation: i) lorsqu'un plateau continental est ajouté à la frontière ouest et ii) lorsqu'on varie le coefficient de friction au fond. Lorsqu'on ajoute un plateau continental, les flux de tourbillons associés aux jets longitudinaux favorisent la circulation abyssale et baissent ainsi les valeurs de saturation du transport. Lorsqu'on augmente le coefficient de friction, la circulation

abyssale est supprimée, ce qui augmente les valeurs de saturation du transport.

Dans les expériences où l'on rajoute un vent constant au profil de référence, un décalage est observé entre les résultats des simulations numériques et les prévisions du modèle analytique. Cela définit un nouveau régime où le vent lui-même est fort en comparaison à son rotationnel. Le flux vertical de quantité de mouvement des tourbillons méso-échelle peut être utilisé afin de distinguer les différents régimes. En effet, ce flux est orienté vers le haut lorsque la dynamique est dominée par le rotationnel tandis qu'il est vers le bas lorsque le vent lui-même domine la dynamique. Dans le régime dominé par le rotationnel, une circulation de type Sverdrup est observée dans l'ensemble du bassin, même en absence de péninsules. De plus, le transport y est saturé, tel que suggéré par la théorie analytique.

Le modèle analytique est ensuite généralisé au cas où la stratification est continue. On effectue des simulations numériques où la résolution verticale est variée afin de tester cette théorie généralisée. Ces simulations montrent que les modèles à 2 et 5 couches donnent des résultats similaires lorsque les effets d'inertie sont faibles. Par contre, d'intenses circulations générées au-dessus de la topographie bloquent le détroit de Drake et réduisent le transport lorsque les effets d'inertie sont importants. Cependant, ce comportement disparaît lorsqu'une topographie plus réaliste est utilisée. Dans ce contexte, les simulations numériques correspondent aux prévisions du modèle analytique. De plus, on observe que dans un régime où le rotationnel est dominant, les péninsules jouent un rôle important dans la dynamique lorsque le vent est faible tandis que leur rôle devient de plus en plus négligeable lorsque le vent augmente.

STATEMENT OF ORIGINALITY

The original contributions of this thesis include:

i) the development of a new analytic model for the dynamics and transport of the ACC. It is based on the idea that the current can be considered as the superposition of a basin-like circulation and a channel-like circulation. We focus our attention on the basin-like contribution, which we assume to obey Sverdrup dynamics, ignored in modern theories of the ACC. To the best of our knowledge, it is the first time that the vertical structure of the Sverdrup circulation has been taken into account to describe the ACC. Parts of this Sverdrup circulation that are below the level of topography will drive recirculations that cannot contribute to the ACC and must be removed from the transport calculation. Moreover, these bottom layer recirculations can be felt by the upper part of the water column, reducing further the circumpolar transport. The analytic model describes how this leads to a saturation of the transport.

ii) the development of a computationally efficient high-resolution quasigeostrophic model in a geometry similar to the Southern Ocean. This involves the implementation of the multigrid method to solve the elliptic differential equations in our model geometry.

iii) a complete set of numerical experiments considering variation of almost every model parameter in a geostrophic turbulence context. The analytic model is tested for robustness with respect to the basin dimensions, the gap width, the Rossby radius, the bottom drag, the relative amount wind stress to wind stress curl, the vertical resolution and the addition of realistic bottom topography. Careful analysis

of these experiments shows that much of the behavior observed can be explained in the general framework of the analytic model.

iv) a momentum flux analysis of the 2-layer model under variation of the bottom drag and the relative amount wind stress to wind stress curl is also carried out. A scale decomposition of the interfacial form stress term highlights the relative importance of the large scale standing eddies compared to the small scale transient eddies in the vertical transfer of eastward momentum.

TABLE OF CONTENTS

LIST OF TABLES

LIST OF FIGURES

CHAPTER 1
Introduction

The Antarctic Circumpolar Current (ACC) flows around Antarctica between latitudes of around 40 to 65 degrees South. It is the largest and strongest current system in the world ocean, extending over more than 25 000 km and having a volume transport estimated at around 150 Sv (1 Sv = 10^6 m^3/s) through Drake Passage [*Mazloff et al.*, 2010]. Serving as a connection between the major ocean basins, the ACC plays a fundamental role in the earth's climate system. The meridional overturning across the ACC is linked with every major ocean basin and its water masses are found throughout the global oceans [*Marsh et al.*, 2000]. Additionally, a large fraction of the mechanical energy input by the wind occurs in this region [*Wunsch*, 1998]. The ACC is also an important site for mixing and oceanic uptake of CO_2 [*Patra et al.*, 2005]. However, despite the fundamental role of the ACC in the earth's climate, its dynamics are still not fully understood.

The dynamics of the ACC are particularly interesting since the ACC is the only zonally reconnecting oceanic current. As will be discussed in this thesis, the main difficulty of obtaining a simple theory comes from the fact that nonlinear baroclinic eddies are of leading order in its dynamics. Usually, two main diagnostics are considered when theorizing on the ACC circulation: its zonal and its meridional mass transport. These diagnostics are intimately linked since the vertical shear of the

zonal current is dependent on the meridional density structure, which is also central to the meridional overturning circulation.

In this thesis, we focus our attention on the zonal transport of the ACC. In the following, we briefly review some theories as to what sets this transport. These can be artificially divided in two groups: basin-like or channel-like theories. We now explain the origins of this artificial division. Figure 1–1 shows a sketch of the large scale ocean circulation in both hemisphere. Most of the world oceans are bounded

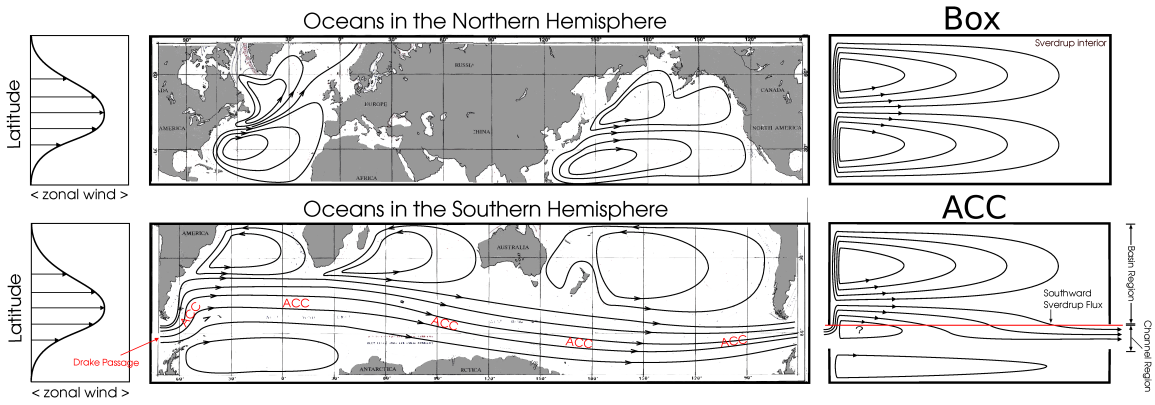

Figure 1–1: Sketch of the large scale ocean circulation in both hemispheres. The left panels show a scketch of the typical zonal wind profile at mid-latitudes. The right panels show the geometries that will be used in this thesis.

zonally by continental coasts. For example, this is the case for the Atlantic and Pacific oceans in the northern hemisphere. Under a mid-latitude zonal wind jet forcing, the large scale circulation in these closed "box" oceans forms double gyres (see Figure 1–1). At first order, this large scale circulation pattern obeys the Sverdrup balance, which can be obtained from the quasigeostrophic reduced-gravity potential vorticity

equation

$$D_t \left[\nabla^2 \psi - \frac{1}{L_\rho^2} \psi + \beta y \right] = \widehat{k} \cdot \nabla \times (\text{Forcing} - \text{Dissipation}), \tag{1.1}$$

where $D_t() = \frac{\partial}{\partial t}() + \mathrm{J}[\psi, ()]$ is the total time derivative, ψ is the streamfunction,[1] L_ρ is the Rossby radius of deformation and β is the northward spatial derivative of the Coriolis parameter. This equation describes the motion of a thin layer of fluid on a horizontal plane. Neglecting dissipation and considering large horizontal scales at equilibrium, (1.1) reduces to

$$\beta \frac{\partial \psi}{\partial x} = \frac{\widehat{k} \cdot \nabla \times \tau}{\rho_0 H}, \tag{1.2}$$

where τ is the wind stress blowing over the ocean, ρ_0 is the reference density and H is the total ocean depth. Equation (1.2) is called the Sverdrup balance. Using a sinusoidal zonal wind profile, $\tau = \tau^x \sim \sin^2(\pi y / L_y)$, solution of (1.2) gives a double gyre streamfunction pattern similar to the one shown in the upper right panel of Figure 1–1. Note that the western boundary currents are obtained adding bottom friction or viscosity[2] in (1.2).

Figure 1–1 shows how the flow pattern is changed in the southern hemisphere, where streamlines are allowed to reconnect zonally through Drake passage, forming

[1] The streamfunction is related to the zonal velocity, $u = \frac{-\partial \psi}{\partial y}$, and the meridional velocity, $v = \frac{\partial \psi}{\partial x}$.

[2] The solution adding bottom drag is known as the Stommel model whereas the solution adding viscosity is known as the Munk model.

the ACC. In this thesis, we will refer to the region north of Drake Passage as the basin region and the region inside the Drake Passage latitude band as the channel region. Basin-like theories of the ACC basically assume that the remains of the gyre-like circulation in the basin region feeds and controls the strength of the ACC. The original idea dates to *Stommel* [1957], who suggested that the transport of the ACC is given by the southward Sverdrup flux into the channel region. In his picture, all latitudes are blocked by meridional walls. However, when latitudes are unblocked, one cannot apply the Sverdrup balance directly in the channel region. In a box configuration, the Sverdrup circulation is obtained by solving a simplified vorticity equation assuming that ψ is constant along the boundary. When there is an open channel, the streamfunction value at the northern boundary does not need to equal the value at the southern boundary. This introduces an additional unknown that cannot be determined by looking at the vorticity budget alone [*Gill*, 1968]. One then needs to consider the zonal momentum balance in the unblocked latitudes.

Channel-like theories link the ACC to a zonally reconnecting channel, and focus on the zonal momentum budget, rather than the vorticity budget of the current. In this view, the vertically integrated solution is a balance between zonal surface stresses and the pressure difference induced by the presence of bottom topography [*Munk and Palmén*, 1951]. This pressure difference term in the zonal momentum balance equation is called the topographic form drag. It is a net zonal momentum sink since the zonal pressure difference across topographic features tends to exert a positive torque on the solid earth. Associated with this is a negative torque on the ocean and, consequently, a poleward mass flux. When zonal momentum balance

is considered as a function of height, some mechanism is needed to transfer the momentum input at the surface to the deep ocean, where it can be removed by topography. This is generally assumed to be accomplished by the interfacial form drag, which can be seen as the form drag occurring at the interface between two layers of different density.

Transient eddies play a central role in the form drag mechanism [*Johnson and Bryden*, 1989; *Marshall et al.*, 1993; *Straub*, 1993]. As the winds blow at the surface, an eastward current is accelerated in the upper layers. This creates a vertical shear that leads eventually to baroclinic instability. The transient eddies then produced by this baroclinic instability are assumed to transmit downward the zonal momentum produced by the wind stress. This process continues until the momentum is transferred into the deep water where topographic form drag can balance the upper wind stress. Note that transient eddies are important even in situations where standing eddies accomplish most or all of the downward transfer of eastward momentum [*Straub*, 1993].

To see the consequence of this channel dynamics to the total zonal transport, let us consider a simple 2-layered rigid lid ocean with η being the interface between the layers. As the wind blows at the surface, the meridional slope of the interface $\alpha = \partial\eta/\partial y$ will grow. The condition of baroclinic instability will reduce in this case to a critical slope $\alpha_c = -\beta h/f_0$ where h is the height of the second layer. Following this baroclinic instability argument, we find two ways to estimate the transport in function of the strength of the wind stress: i) for weak wind stress, baroclinic instability prevents the vertical shear from developping further than the

critical slope of the interface α_c. This condition for baroclinic instability leads to

$$\text{Transport} \approx \beta L_\rho^2 H_{tot} L_y, \tag{1.3}$$

as derived by *Straub* [1993], where H_{tot} is the total depth of the ocean, $L_\rho = \sqrt{g' H_1 H_2 / (f_0^2 H_{\text{tot}})}$ is the Rossby radius of deformation, and L_y is the width of the channel. ii) For stronger wind stress, the shear develops further than the baroclinic instability condition α_c and the transport is then related to the wind stress following a square root relation [*Johnson and Bryden*, 1989]:

$$\text{Transport} \propto \sqrt{\tau}. \tag{1.4}$$

However, studies of the transport dependence with the wind stress (in simple models [e.g., *Tansley and Marshall*, 2001; *Hogg and Blundell*, 2006] and more complex GCM [e.g., *Hallberg and Gnanadesikan*, 2006]) have shown that the circumpolar transport is nearly constant even at moderate to strong forcing. This shows that (1.4) is not a good prediction. Moreover, the transport as computed by (1.3) is of the order of 10 Sv using typical Southern Ocean values, which is an order of magnitude too small. This suggests that other mechanisms than transient eddies are acting to remove zonal momentum from the system.

A second look at Sverdrup theory

Because the Sverdrup balance does not apply in a channel-like domain, recent studies on the ACC start by claiming that the Sverdrup framework fails in the Southern Ocean and that it is not relevant to the ACC [e.g., *Marshall and Radko*, 2003; *Olbers et al.*, 2004; *Hogg and Blundell*, 2006]. This, however neglects the fact

that the ACC is bounded to the north and south by regions where continental barriers do not preclude Sverdrup dynamics.

Basin-like theories are usually based on linear Sverdrup theory. However, it is obvious that, as the forcing increases, there will be departure of the system from this linear regime. Indeed, this departure has been studied deeply for the case of a double gyre in a closed rectangular basin. For this case, it is observed in numerous studies that an inertial recirculation develops on the west of the gyres in the surface flow [e.g., *Pedlosky*, 1996]. This recirculation is associated with the eastward extension of the western boundary current, that manifests itself as a turbulent eastward jet in the instantaneous fields. As the wind forcing increases, there is a deeper penetration of this turbulent jet into the domain, and the inertial recirculation becomes larger. In a 2-layered model, the eddies produced in the surface layer inside this inertial recirculation region are known to drive the circulation in the lower layer. *Rhines and Young* [1982] synthesized this phenomenon in a theory involving lines called characteristics (or geostrophic contours) that are defined by

$$\Phi = \psi_B + \beta L_\rho^2 y, \tag{1.5}$$

where ψ_B is the barotropic streamfunction and L_ρ is the Rossby radius of deformation (the derivation of Equation (1.5) is in Appendix 1). When the wind forcing is weak, Φ is dominated by $\beta L_\rho^2 y$ and the characteristics follow latitude circles. As the wind stress becomes stronger, ψ_B slowly increases and distorts these zonal characteristics. Theory suggests that there is essentially no motion in the lower layers in regions where the characteristics are blocked (i.e. if the contours extended back to the

eastern boundary). Then, to get the lower layers in motion there must exist a region where the characteristics close upon themselves (or do not extend to the eastern boundary); that is, ψ_B must be strong enough to have sufficiently distorted the Φ contours.

Following this theory, if the wind stress is strong enough, a significant portion of the Sverdrup circulation will be in the lower layers. If, in addition, the circumpolar flow is blocked by topography in these lower layers, this will create recirculations.[3] The horizontal extent of the recirculations is not limited to the latitudes blocked by meridional walls, so that parts of these recirculations can appear in the channel region.

The earlier studies of *McWilliams et al.* [1978] and *Treguier and McWilliams* [1990] identifies the crucial role of standing eddies on circumpolar currents. In a zonally reconnected channel, *Treguier and McWilliams* [1990] showed that the form stress increases with the wavelength of the bottom topography. For their larger scale topographies, standing eddies provided the dominant contribution to the total downward momentum flux whereas transient eddies produced an upward momentum flux. Associated with this was a significant reduction of the zonal transport.

In the Southern Ocean, meridional boundaries such as the Patagonian peninsula suggest that Sverdrup dynamics might apply north of Drake Passage latitudinal band. As mentioned above, if sufficiently strong, part of the Sverdrup flux will feed

[3] In this thesis, the term recirculation or recirculating streamlines is generally used in opposition to open circumpolar streamlines

abyssal recirculations. Associated with these are large scale deformations of the thermocline. In the channel latitudes, these deformations then provide an interface against which pressure torques can act to transmit eastward momentum downwards. In other words, the recirculations can be seen as large scale standing eddies, which one anticipates will play a role in the zonal momentum balance. Our main objective in this thesis is to study this, and other possible influence of Sverdrup, or basin-like circulation on the circumpolar current.

Scope of the thesis

As mentioned earlier, the zonal transport is closely linked to the meridional overturning across the ACC since both ultimately depend on its meridional density structure. For example, a strong stratification implies a decoupling between the upper part of the ocean and the abyss. The mechanisms for downward transmission of zonal momentum are less effective in this case and a stronger transport will result. Then, diapycnal overturning induced by buoyancy forcing may also play an important role in setting the ACC zonal transport [*Hallberg and Gnanadesikan*, 2001; *Henning and Vallis*, 2005]. Even without buoyancy forcing, the diapycnal overturning and the meridional density structure may vary in function of the wind stress itself. Recent work addressing the ocean's meridional overturning circulation as it crosses the ACC has applied residual-mean theory to channel models of the ACC [e.g., *Karsten et al.*, 2002; *Marshall and Radko*, 2003; *Olbers and Visbeck*, 2005].

In this thesis, we neglect the effect of diapycnal overturning by considering a fixed stratification quasigeostrophic ocean. This is a strong constraint and one should be careful in making quantitative comparison of the results presented in this work to

the actual Southern Ocean. One should also keep in mind that results obtained here can change quantitatively when using a more realistic general circulation model. Our goal is then to understand the simpler case of a fixed stratification, quasigeostrophic ACC, in order to isolate the general behaviors controlling its zonal transport and dynamics. Results of this can then be used as a basis for subsequent studies in a more realistic context.

Synopsis of the Thesis

In Chapter 2, we present a new analytic model in which the ACC is considered as a superposition of a basinlike and channellike contributions in a two layer context. The robustness of this analytic model is then tested over a wide range of parameters using a numerical model we develop. In Chapter 3, this numerical study is carried further by testing for sensitivity to parameters that do not appear in the analytic model. This includes the effect of the bottom friction and the addition of a constant wind stress. Chapter 4 begins with the presentation of a generalization of the analytic model to a continuously stratified context. We then test aspects of this with a multi-layer quasigeostrophic numerical model. Experiments using realistic topography and basin dimensions are also carried out. The Chapter ends with the presentation of numerical simulations showing that Sverdrup balance can apply over most of the domain even when no latitudes are blocked by meridional walls. Finally, a summary of the main results and conclusions of this thesis is given in Chapter 5. Some possible future work is also discussed in this final chapter.

CHAPTER 2

Basin and Channel Contributions to a Model Antarctic Circumpolar Current

This chapter introduces the 2-layer analytic model. It also presents a robustness analysis of this analytic model. It is based on the paper: Nadeau, L.-P., and D. Straub, 2009: Basin and channel contributions to a model Antarctic circumpolar current. Journal of Physical Oceanography, 39, 986–1002.

Basin and Channel Contributions to a Model Antarctic Circumpolar Current

Louis-Philippe Nadeau[1] and David N. Straub[1]

[1]Department of Atmospheric and Oceanic Sciences, McGill University, Montréal, QC, Canada

Abstract

We revisit the idea that basin-like dynamics may play a major role in determining the Antarctic Circumpolar Current (ACC) transport. A simple analytic model is developed to describe the relationship between the wind stress and transport. At very low wind stress, a non-zero minimum is predicted. This is followed by two distinct dynamical regimes for stronger forcing: a Stommel regime, for which transport increases linearly with forcing strength and a saturation regime, where the transport levels off. The baroclinic structure of the Sverdrup flux into the Drake Passage latitude band is central to the analytic model and the geometry of characteristics, or geostrophic contours, is key to predicting the transition between the two regimes. A robustness analysis is performed using an eddy-permitting quasigeostrophic model in idealized geometries. We carry out many simulations in large domains over a range of forcing strengths. The simulations agree qualitatively with the analytic model, with two main discrepancies being related to zonal jet structures and to a western boundary inertial recirculation. Eddy fluxes associated with zonal jets modify the baroclinic structure and lower the saturation transport value. Inertial effects increase the transport, although this effect is mainly limited to smaller domains.

2.1 Introduction

Most theories for what sets Antarctic Circumpolar Transport (ACC) can be classified as either basin- or channel-like. Basin-like theories[1] date to *Stommel* [1957], who views the ACC as fed by a southward Sverdrup transport into the Drake

[1] Also known as Sverdrup-like theories [e.g., *Hughes*, 2002].

Passage latitude band. The resulting eastward current then flows through Drake Passage and connects with the western boundary current along the eastern coast of Patagonia. The details of the dynamics in the Drake Passage latitude band are seen as non-essential, with the transport being determined by the basin-like dynamics to the north. Specifically, the transport is linearly related to the zonally integrated wind stress curl just north of Drake Passage. Computing this integral gives an estimate that is compatible with the range of values of the observed transport [*Baker*, 1982]. This idea has been refined over the years in more recent papers [*Webb*, 1993; *Warren et al.*, 1996; *Hughes*, 2002]; however, the fundamental argument is always that Sverdrup dynamics apply to the Southern Ocean and determine the transport.

Channel-like theories point out that Sverdrup dynamics require a western boundary layer and as such Sverdrup theory must fail somewhere in the Drake Passage latitude band. This has led *Johnson and Bryden* [1989] and others [*Straub*, 1993; *MacCready and Rhines*, 2001; *Rintoul et al.*, 2001; *Karsten et al.*, 2002; *Marshall and Radko*, 2003; *Olbers et al.*, 2004] to consider the ACC (or at least part of it) as a zonally reconnecting channel, with topographic form drag [e.g., *Munk and Palmén*, 1951] acting as the momentum sink. It is widely recognized that in this geometry, transient eddies are needed to establish a vertical transmission of momentum to the topography and to close the meridional circulation [e.g., *Marshall et al.*, 1993; *MacCready and Rhines*, 2001]. In the absence of eddies, solutions are dependent on artificially large and somewhat arbitrarily chosen viscous and diffusive coefficients.

In a paper that motivates our study, *Tansley and Marshall* [2001] perform a series of experiments to test the various ideas for what sets the ACC transport.

They use a purely wind-driven 2-layer eddy-permitting model and consider a wide range of wind forcing in various geometries. Of particular relevance to us are their simulations in which a model Patagonia and Antarctic Peninsula are present, so that a zonally reconnecting latitude band lies adjacent to regions of blocked geostrophic contours to the north and south. In this geometry, their results show that transport does not follow any of the theories mentioned above (see their Fig. 15). For example, for forcing above a certain threshold, transport appears to saturate (i.e., vary weakly) instead of growing linearly with the wind stress as predicted by Stommel or following some other power laws [e.g., *Johnson and Bryden*, 1989; *Rintoul et al.*, 2001]. Note that attempts to verify such power laws have also been made in coarse-resolution models without success [*Gnanadesikan and Hallberg*, 2000; *Gent et al.*, 2001].

A posteriori, this is perhaps not surprising. The square root law predicted by Johnson and Bryden applies in a channel, whereas observations show the ACC to make a sharp northward turn just east of Drake Passage, where it joins the Falkland/Malvinas Current. This lends weight to the idea that the ACC is related to this western boundary current, as suggested by Stommel, so that channel-like theories are unlikely to tell the whole story. Conversely, Stommel's theory assumes that all of the Sverdrup transport into DP latitudes feeds the circumpolar flow, whereas this need not be the case. For example, part of the southward Sverdrup transport might occur in an abyssal layer where topography precludes circumpolar flow. Additionally, the Southern Ocean is known to be an eddy-rich environment. As such, it is not too surprising that linear Sverdrup theory, which ignores this strong turbulence, fails.

In this article, we consider the ACC transport as the sum of a basin-like and a channel-like contribution. Our focus is primarly on the basin-like dynamics and its role in determinig the total transport. The starting point is a comparison between the wind-driven circulation in closed-basin and Southern Ocean geometries. That is, we are interested in whether insight from the much-studied closed ocean basin problem with gyre-like circulations can help us to understand the mechanisms determining ACC transport. In the basin case, Sverdrup dynamics apply far from boundaries. These assume large horizontal length scales, so that relative vorticity can be neglected at least outside of the boundary layers and as a first approximation. In a two layer flat bottom quasigeostrophic ocean, one recovers the Sverdrup relation for the barotropic streamfunction ψ_B

$$\beta \frac{\partial \psi_B}{\partial x} = \frac{\widehat{k} \cdot \nabla \times \boldsymbol{\tau}}{\rho_0 H}, \tag{2.1}$$

where H is the total ocean depth, $\boldsymbol{\tau}$ is the horizontal wind stress at the surface, ρ_0 is the reference density and β is the northward spatial derivative of the Coriolis parameter. The lower layer streamfunction, ψ_2, obeys a characteristic equation [e.g., *Rhines and Young*, 1982; *Pedlosky*, 1996]:

$$\mathrm{J}\left[\psi_2, \Theta\right] = 0, \tag{2.2}$$

where J[ ] is the Jacobian operator and

$$\Theta = \psi_B + \beta L_\rho^2 y \tag{2.3}$$

is the characteristic function in which L_ρ is the baroclinic Rossby radius. ψ_B and Θ are known functions of the forcing and it is assumed that passive boundary layers can be appended to satisfy boundary conditions. The characteristic function, Θ, corresponds to a streamfunction for the characteristic velocity and contours of Θ are called characteristics (also called geostrophic contours).

Where Θ contours extend back to the eastern boundary, characteristics are said to be blocked. In this case, (2.2) implies that the lower layer is at rest. Where characteristics do not extend back to the eastern boundary, eddy-driven gyres and inertial recirculation are free to develop in the ψ_2 field [e.g., *Rhines and Schopp*, 1991]. Thus, Sverdrup transport across a blocked characteristic is top-trapped, whereas this need not to be the case for Sverdrup transport across a free characteristic. In our Southern Ocean geometry, this distinction should also apply to Stommel's idea that a southward Sverdrup transport into the Drake Passage latitude band feeds the ACC. Moreover, if topography effectively prohibits circumpolar flow at depth, one should anticipate that only the upper ocean part of the Sverdrup flux feeds the ACC.

Our main interest is thus to refine Stommel's theory taking into account the ideas discussed above and to compare its predictions with results from eddy-permitting numerical simulations. We simplify by considering a two layer formulation in an idealized geometry, allowing us to carry out multiple simulations at eddy-permitting resolution in large domains. The following section presents our numerical model and compares results for a test simulation in basin and Southern Ocean like geometries. An analytic model for the ACC transport is presented in Section 2.3. This is compared with numerical results for a wide range of forcing strengths and different sized

domains in Section 2.4. Various robustness tests are also presented. Finally, a brief summary ends this paper in Section 2.5.

2.2 Numerical Model and Experimental Design

The model is based on a 2-layer version of the quasi-geostrophic potential vorticity equations *Pedlosky* [1996]:

$$D_t \left[\nabla^2\psi_1 - F_1(\psi_1 - \psi_2) + \beta y - F_0\psi_1\right] = -A_h\nabla^6\psi_1 + \frac{\widehat{k}\cdot\nabla\times\boldsymbol{\tau}}{\rho_1 H_1} \quad (2.4)$$

$$D_t \left[\nabla^2\psi_2 + F_2(\psi_1 - \psi_2) + \beta y + \frac{f_0}{H_2}h_{\rm b}\right] = -A_h\nabla^6\psi_2 - r\nabla^2\psi_2, \quad (2.5)$$

where $D_t() = \frac{\partial}{\partial t}() + \mathrm{J}[\psi, ()]$ is the total time derivative, $F_0 = \frac{f_0^2}{gH_1}$, $F_1 = \frac{f_0^2}{g'H_1}$, $F_2 = \frac{f_0^2}{g'H_2}$, f_0 is the mean Coriolis parameter, g is the gravitational acceleration, $g' = g\frac{\Delta\rho}{\rho}$ is the reduced gravity, (H_1 and H_2) are layer thicknesses, $h_{\rm b}$ is bottom topography, A_h is a lateral biharmonic viscosity coefficient and r is a bottom drag coefficient.

2.2.1 Numerical implementation and geometry

A third order Adams-Bashforth time stepping scheme is used [*Press et al.*, 1996]. All the Jacobian operators are computed using the Arakawa scheme that conserves kinetic energy and enstrophy [*Arakawa*, 1966]. No normal flow and free slip conditions (i.e., $\nabla^2\psi = \nabla^4\psi = 0$) are applied at solid walls. A multigrid method is used to do the elliptic inversion [*Briggs et al.*, 2000]. To facilitate this multigrid inversion, only rectangular shaped domains are considered. The implementation of mass and momentum conservation laws of the quasigeostrophic equations in a multiply connected domain is similar that of *McWilliams* [1977]. Only wind forcing is considered

and the wind stress takes the form of

$$\boldsymbol{\tau} = \widehat{i}\ \tau_0 \sin^2(\pi y/L_y), \qquad y \in [0, L_y], \tag{2.6}$$

where L_y is the meridional extent of the domain. This is similar to other ACC (channel) studies [e.g., *Treguier and McWilliams*, 1990] and gives the familiar double gyre forcing typical of basin gyre studies upon taking the curl. All runs are carried out at eddy-permitting resolution and model parameters can be found in Table 2–1.

Table 2–1: Model parameters

Parameter	Symbol	Value
Rossby deformation radius	L_ρ	32 km
Horizontal resolution	$\Delta x = \Delta y$	15 km
Length of channel	L_x	$(5 \text{ to } 20) \cdot 960$ km
Width of channel	L_y	$(2 \text{ to } 4) \cdot 960$ km
Width of Drake passage	L_{gap}	240 km
Position of $\nabla \times \tau = 0$	$L_y/2$	960 to 1920 km
Top layer	H_1	1200 m
Bottom layer	H_2	2800 m
Coriolis parameter	f_0	$-1.3 \cdot 10^{-4}$ s^{-1}
Beta parameter	β	$1.5 \cdot 10^{-11}$ m^{-1}s^{-1}
Gravitational acceleration	g	9.8 m/s^2
Reduced gravity	g'	0.02 m/s^2
Reference density	ρ_1	1035 kg/m^3
Bottom friction coefficient	r	10^{-7} s^{-1}
Bi harmonic dissipation coefficient	$A_h = \beta \cdot \Delta x^5$	$1.14 \cdot 10^{10}$ m^4/s

We wish to compare idealized basin and Southern Ocean geometries. To this end, most experiments are made both in a closed-basin and a corresponding "Southern

Ocean" domain. To form the Southern Ocean domain, a segment of the meridionally-oriented walls are cut and a repeating channel boundary condition is imposed. This can be thought of as a channel with two "peninsulas", one corresponding to Patagonia and the the other to the Antarctic Peninsula (see Fig. 2–1).

Figure 2–1: Geometry for the closed-basin (Box) and Southern Ocean (ACC) experiments.

Because of our multigrid method of doing the elliptic inversion, the width of the peninsulas is constrained to be an integer multiple of 2^4, where five levels are used in our V-cycle [*Briggs et al.*, 2000]. For simplicity, we take the peninsulas width to be zero. While that may seem counter-intuitive, its numerical implementation is straight-forward since the value of ψ is equal on both sides of the peninsula (no normal flow boundary condition implies $\partial_y \psi = 0$ on meridional walls).

As it is well known that topographic form drag plays a dominant role in the zonal momentum budget in the Drake Passage latitudes, we introduce topography (see Fig. 2–1). Following a number of studies [e.g., *Wolff et al.*, 1991; *Straub*, 1993; *Krupitsky*

and Cane, 1997; *Tansley and Marshall*, 2001], we introduce a topographic ridge that is sufficiently high so as to block lower layer potential vorticity contours. Since the lower layer is not forced directly, this effectively constrains the circumpolar flow to the upper layer. The specific topography chosen is a Gaussian ridge mimicking the Scotia Ridge and following the western boundary as a half-Gaussian that might be thought of as a continental rise. To make the comparison cleaner, an identical ridge is also introduced in the closed-basin experiments. As such, our closed basin experiments differ somewhat from the traditional flat-bottomed double gyre problem since the topography introduces an asymmetry between the subtropical and subpolar gyres [see *Becker and Salmon*, 1997]. Comparison with the more standard flat bottom basin case is given in Section 2.4.

2.2.2 A preliminary Box-to-ACC comparison

We now discuss the result of a preliminary Drake Passage opening experiment in order to compare solutions in our closed basin and Southern Ocean geometries. We consider a weakly forced case in a 3840km $\times$ 9600km domain. The limit of weak forcing is considered since Sverdrup dynamics might reasonably be expected to apply. The model was integrated until statistical equilibrium was reached and then long time averages (i.e., 100 yr) were taken. Figure 2–2 shows the characteristic contours and time-averaged streamfunctions for each layer. Note that the characteristic function is not known *a priori* in the ACC case since the barotropic streamfunction is not determined by (2.1) in the Drake Passage latitude band. The contours plotted for the ACC case use the model time averaged ψ_B field in (2.3) rather than its estimate from linear Sverdrup theory (as plotted in the Box case). Also note that the interpretation

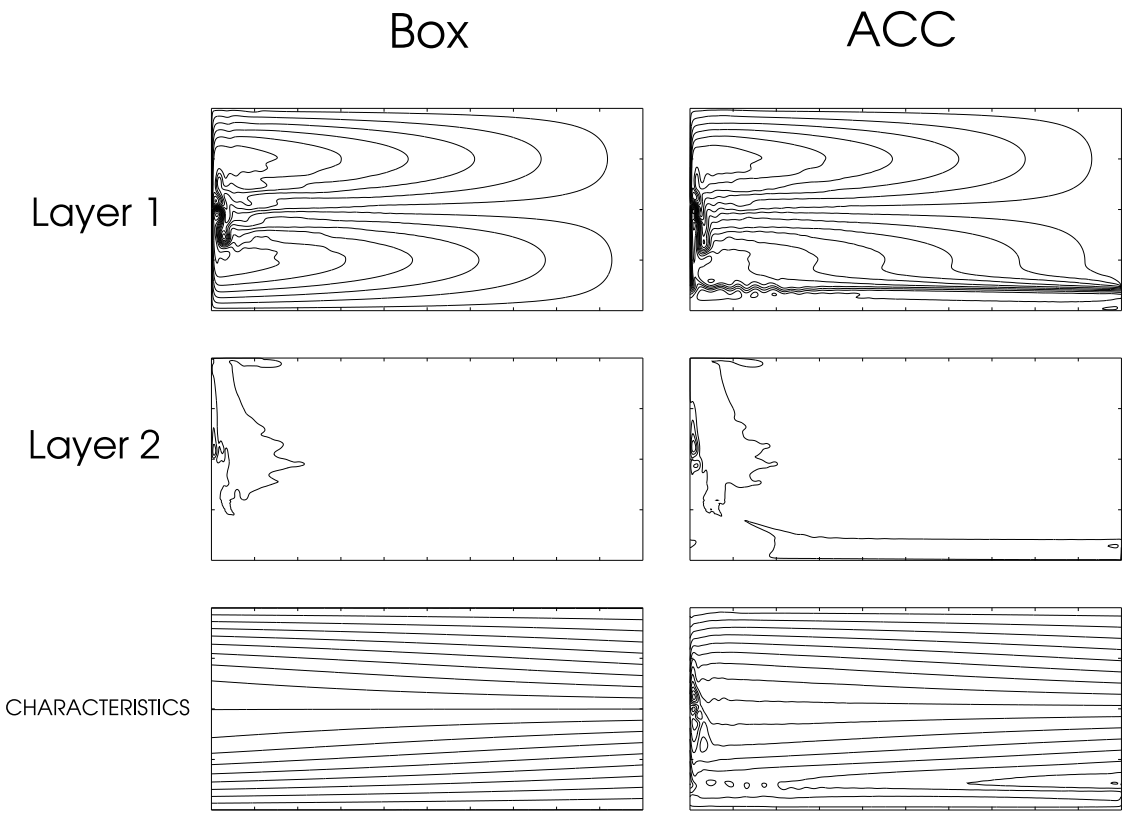

Figure 2–2: Time averaged streamfunction and characteristics for the Drake Passage opening experiment in a weakly forced case ($\tau_0 = 0.08$ N/m^2). The contours of Θ plotted for the ACC case use the model time averaged ψ_B field in (2.3) while for the Box case, its estimate from linear Sverdrup theory (2.1) is used.

of characteristics over the bottom topography is unclear since topography is neglected in the derivation of Eq. 2.3 (but see also *Dewar* [1998] and Section 2.4.2).

As expected, the Sverdrup circulation is observed for the time mean interior flow in the Box case in Fig. 2–2. Indeed, except for a small region near the western boundary, eddy activity does not significantly affect the long term averaged fields. Moreover, it is evident that areas of blocked characteristics (most of the domain)

correspond to areas where the lower layer is at rest, consistent with *Rhines and Schopp* [1991]. Note also that, as anticipated given our choice of topography, there is an absence of circumpolar transport in the lower layer: the meridional ridge of Fig. 2–1b prevents any streamlines from reconnecting zonally. Comparing ψ_1 for the Box and ACC cases suggests as useful the idea that the ACC might be thought of as the sum of a basin contribution and a channel contribution. The basin part, north of Drake Passage[2] , is remarkably similar to the gyre-like circulation of the Box case, with a Sverdrup interior and a weak inertial recirculation to the west. The eastward jet heading towards Drake Passage includes both streamlines collected from this basin Sverdup flux and a smaller number of streamlines that remain in or near Drake Passage latitudes. The former will be referred to as the basin contribution and the latter will be referred to as the channel contribution to the circumpolar transport.

2.3 Analytic models

We now want to build on the close correspondence between the Box and ACC solutions north of our model Drake Passage to work out an analytic prediction for the ACC transport. This correspondence may be less evident in cases where the Drake Passage opening is significantly wider. We thus restrict the disscussion to cases where the L_{gap} is relatively small compared to the basin latitudinal extent,

[2] Note that although there is a second basin-like part feature associated with the Antarctic peninsula in the southernmost part of the domain, we will consider it as irrelevant to the ACC considering its smallness.

although the effect of widening Drake passage is considered at the end of Section 2.4. Moreover, we consider that the maximum of the wind stress to be north of the Drake passage so that there is a southward Sverdrup flux into the channel region.

To a first approximation, we will consider the total ACC transport as being the sum of basin-like and channel-like contributions

$$T = T_{\text{Channel}} + T_{\text{Basin}}. \tag{2.7}$$

Below we argue that T_{Channel} can be considered roughly as a constant background contribution while T_{Basin} increases linearly with the forcing strength until a threshold is reached, after which the transport saturates, becoming independent of the forcing strength. Where this transition occurs is linked to the geometry of the characteristics.

2.3.1 Channel contribution

One of the geometries considered by *Tansley and Marshall* [2001] was a channel with a blocking ridge which prevented circumpolar flow in the abyssal layer. In this geometry, they found Straub's [1993] prediction to work in weakly forced cases. That is, marginal instability gives the interface height field slope to be approximately $-\beta H_2/f_0$, so that thermal wind gives the transport to be approximately

$$T_{\text{Channel}} \approx \beta L_\rho^2 H L_{\text{gap}}. \tag{2.8}$$

Since this limit applies for weak forcing, we consider it to be a minimum estimate.

For stronger forcing, a stronger source of eddies is required. Assuming the eddy source to be baroclinic instability in the vicinity of the current, this implies a stronger interface tilt and correspondingly stronger transport. In a flat bottomed channel, the

tilt appears to increase like $\tau_0^{1/2}$ as predicted by Johnson and Bryden [*Tansley and Marshall*, 2001]. In our ACC geometry, however, a basin contribution also adds to the transport — and hence to the interface tilt. Following Stommel, this should increase linearly with τ_0 (i.e., faster than $\tau_0^{1/2}$) at least over a range of τ_0. It then seems reasonable to assume that this provides the additional source of baroclinic instability needed to fuel a more vigorous eddy field. That is, it seems plausible that (2.8) sets a minimum transport which must be added to a basin contribution (see below).

2.3.2 Basin contribution

Based on the preliminary result presented in Section 2.2, we consider as a first approximation that Sverdrup dynamics applies north of Drake Passage (DP). More specifically, we consider ψ_B to be given by (2.1) and the lower layer to be at rest on blocked geostrophic contours. Since our choice of topography precludes circumpolar flow in the lower layer, we define the "basin contribution" to the ACC as only the upper layer portion of the Sverdrup flux into DP latitudes.

Stommel Regime

For weak forcing, characteristics are nearly zonal and blocked nearly everywhere in the domain (Fig. 2–2). As such, the lower layer is at rest in the DP region so that the Sverdrup transport into the DP latitude band is top-trapped. In this limit the basin contribution is similar to that predicted by Stommel:

$$T_{\text{Stommel}} = \left[\int_{x_{\text{west}}}^{L_x} \frac{\widehat{k} \cdot \nabla \times \boldsymbol{\tau}}{\rho_0 \beta} dx \right]_{y=y_{\text{DP}}}, \tag{2.9}$$

where x_{west} is a longitude near the western boundary and y_{DP} gives the northern extent of the DP latitude band. As mentioned, T_{Stommel} increases linearly with τ_0.

We now argue that this Stommel regime is valid from weak to moderate forcing until the transport reaches a threshold value at which it saturates. This threshold occurs when we can no longer assume that the Sverdrup transport into the DP latitudes is everywhere top-trapped along $y = y_{\text{DP}}$.

Saturation Regime

Figure 2–3 shows the characteristic function (2.3) and barotropic streamfunction (2.1) for three values of τ_0. The thick lines in each of the ψ_B panels show the southern branch of a separatrix in the characteristic field. We expect the lower layer to be at rest on blocked geostrophic contours — e.g., to the south of the separatrix and north of $y = y_{\text{DP}}$ (shaded area in Fig. 2–3). For forcing stronger than a threshold value, the separatrix reaches $y = y_{\text{DP}}$ somewhere east of the western boundary layer. At this point, we can no longer assume all the Sverdrup transport into the DP latitudes to be top-trapped. Let x_0 (lower right panel in Fig. 2–3) denote the longitude at which the separatrix intersects $y = y_{\text{DP}}$. For $x > x_0$, Sverdrup flux into DP is top-trapped, whereas to the west it is not. Recall that in T_{Basin}, we are interested in the upper layer portion of the Sverdrup flux across $y = y_{\text{DP}}$. Let T_w be the portion lying west of x_0 and T_e be the portion to the east: $T_{\text{Basin}} = T_w + T_e$.

To solve for T_e, one can compute the upper layer mass flux entering in the channel region

$$T_e = -H_1 \psi_1(x, y_{\text{DP}})\Big|_{x=x_0}^{x=L_x}. \tag{2.10}$$

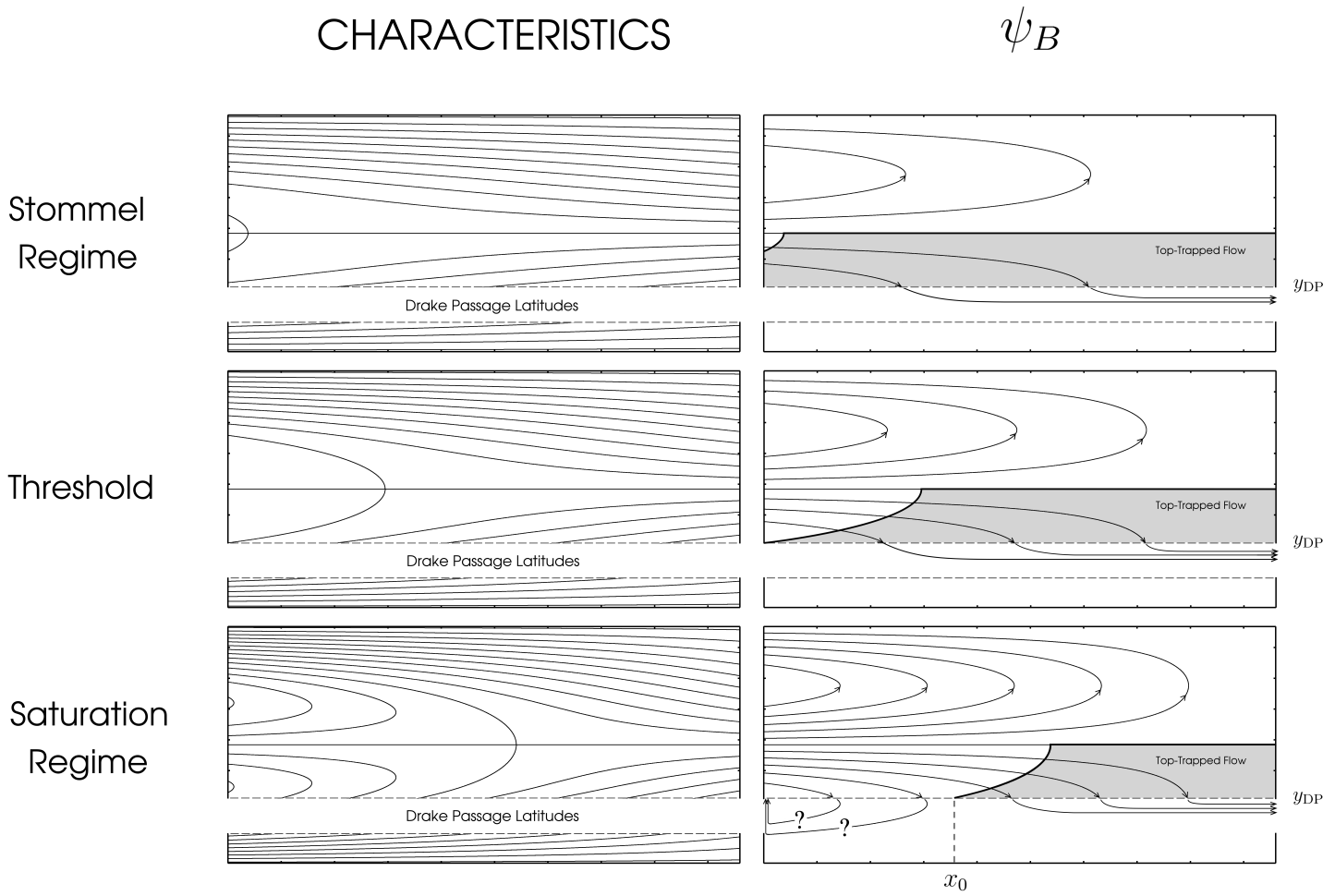

Figure 2–3: The two basic circulation regimes (Stommel and Saturation) for the ACC case. Note that the streamlines shown in the DP latitude band are drawn for illustration purposes only. They are not solutions of (2.1). x_0 is the longitude at which the separatrix Θ contour intersects the northern limit of Drake Passage ($y = y_{\mathrm{DP}}$)

Since the flow is top-trapped to the east of x_0 and taking ψ_B to be zero at $x = L_x$ on the northern peninsula, we have

$$T_e = -H\psi_B(x, y_{\rm DP})\Big|_{x=x_0}^{x=L_x} = H\psi_B(x_0, y_{\rm DP}). \tag{2.11}$$

Then using (2.3) at $(L_x, L_y/2)$ and $(x_0, y_{\rm DP})$,

$$\Theta_{\rm separatrix} = \beta L_\rho^2 \frac{L_y}{2} = \beta L_\rho^2 y_{\rm DP} + \psi_B(x_0, y_{\rm DP}), \tag{2.12}$$

so that T_e is given by

$$T_e = H\beta L_\rho^2 \left[\frac{L_y}{2} - y_{\rm DP}\right]. \tag{2.13}$$

Note that this is proportional to L_ρ^2 and to the meridional distance between $y_{\rm DP}$ and the latitude at which the separatrix characteristic intersects the eastern boundary. Note also that (2.13) is independent of the forcing strength. This is due to two counteracting effects: stronger wind forcing causes both an increase in the Sverdrup velocity and a shift of x_0 to the east, such that the two effects cancel.

What sets T_w is less obvious, although one possibility is that it may be small. For example, the upper layer Sverdrup flux in this region could feed a recirculation, as illustrated schematically in Fig. 2–3. A plausibility argument for this comes from consideration of ψ_2. Since topography precludes a lower layer circumpolar flow, that part of the Sverdrup flux across $y = y_{\rm DP}$ occurring in the lower layer must form part of a closed recirculation or gyre. Viewed from the perspective of upper layer dynamics, this ridge in the ψ_2 field would act as an effective topography, steering the upper layer flow so that it too ultimately returns westward as part of a recirculation.

Taking this as the null hypothesis, we have that $T_{\text{basin}} = T_w + T_e \approx T_e = T_{\text{saturation}}$ since (2.13) is independent of the forcing, τ_0.

Overall, the basin contribution to the ACC is then given by T_{Stommel} from weak to moderate forcing and by $T_{\text{saturation}}$ for stronger forcing

$$T_{\text{Basin}} = \begin{cases} T_{\text{Stommel}} = \left[\int_{x_{\text{west}}}^{L_x} \frac{\widehat{k}\cdot\nabla\times\boldsymbol{\tau}}{\rho_0\beta} dx\right]_{y=y_{\text{DP}}} & : \quad \tau_0 < \tau_{0[\text{threshold}]} \\ T_{\text{saturation}} = H\beta L_\rho^2 \left[\frac{L_y}{2} - y_{\text{DP}}\right] & : \quad \tau_0 > \tau_{0[\text{threshold}]} \end{cases} . \tag{2.14}$$

The transition between these two regimes occurs when the separatrix Θ contour reaches y_{DP} at (or just east of) the western boundary. At this point, the two estimates of transport are identical and the threshold value of τ_0 can be found by simply equating T_{Stommel} to $T_{\text{saturation}}$ — i.e., using (2.6) and (2.14). In sum, a physical interpretation for the saturation regime is that, for τ_0 greater than a threshold value, additional forcing feeds a recirculation but does not serve to increase circumpolar flow.

2.4 Numerical results

We now want to test our analytic predictions using the numerical model of Section 2.3 with the geometry shown in Fig. 2–1b. We begin with a basin dimension of $[L_y \times L_x] = [3840\text{km} \times 9600\text{km}]$. Since this is approximately $[4000\text{km} \times 10000\text{km}]$, we will refer to this using the shorthand $[4 \times 10]$. The runs are performed at a spatial resolution of 15 km with $L_\rho = 32$ Km and all other model parameter are the same as Table 2–1. After a spin-up phase, the system reaches an equilibrium state to which statistics can be applied. The distributions for 100 yr of the transport time series at equilibrium display Gaussian statistics with well defined means and standard

deviations (not shown). The average and standard deviation of the transport is shown as a function of τ_0 in Fig. 2–4. The analytic prediction — sum of Eqn. 2.8

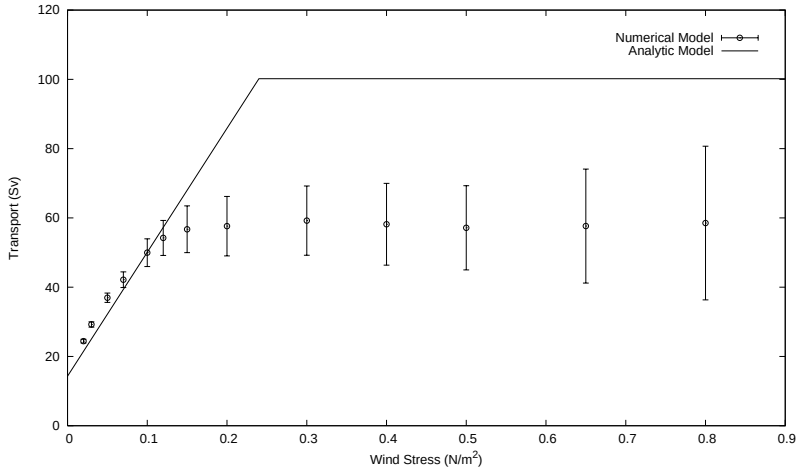

Figure 2–4: Mean circumpolar transport (circles) as a function of the wind stress amplitude, τ_0, for the $[4 \times 10]$ basin (i.e., $[L_y \times L_x] = [3840\text{km} \times 9600\text{km}]$). Also shown are standard deviations and the analytic prediction.

and 2.14 — is also shown.

The general shape of the analytic prediction is basically respected by the numerical results — i.e. there is a non-zero minimum at very weak wind stress followed by a growing phase and a saturation phase. However, from Fig. 2–4, it is obvious that the observed saturation occurs at a smaller value than predicted by the simple theory. In the following, we argue that this behavior is due to transient eddies associated with zonal jets in the ocean interior which alter the baroclinic structure of the flow.

2.4.1 Impact of transient eddies

Fig. 2–5 shows mean contours of Θ and ψ_2 in the observed saturation regime ($\tau_0 \gtrsim 0.1$ N/m^2). Note that the lower layer is not at rest over regions of blocked

characteristics, in contrast to predictions of *Rhines and Young* [1982] and numerical simulations of *Rhines and Schopp* [1991]. Specifically, $\psi_2 \neq 0$ to the south of the analytic separatrix (thick lines) and north of $y = y_{\rm DP}$ (dotted line). Figure 2–

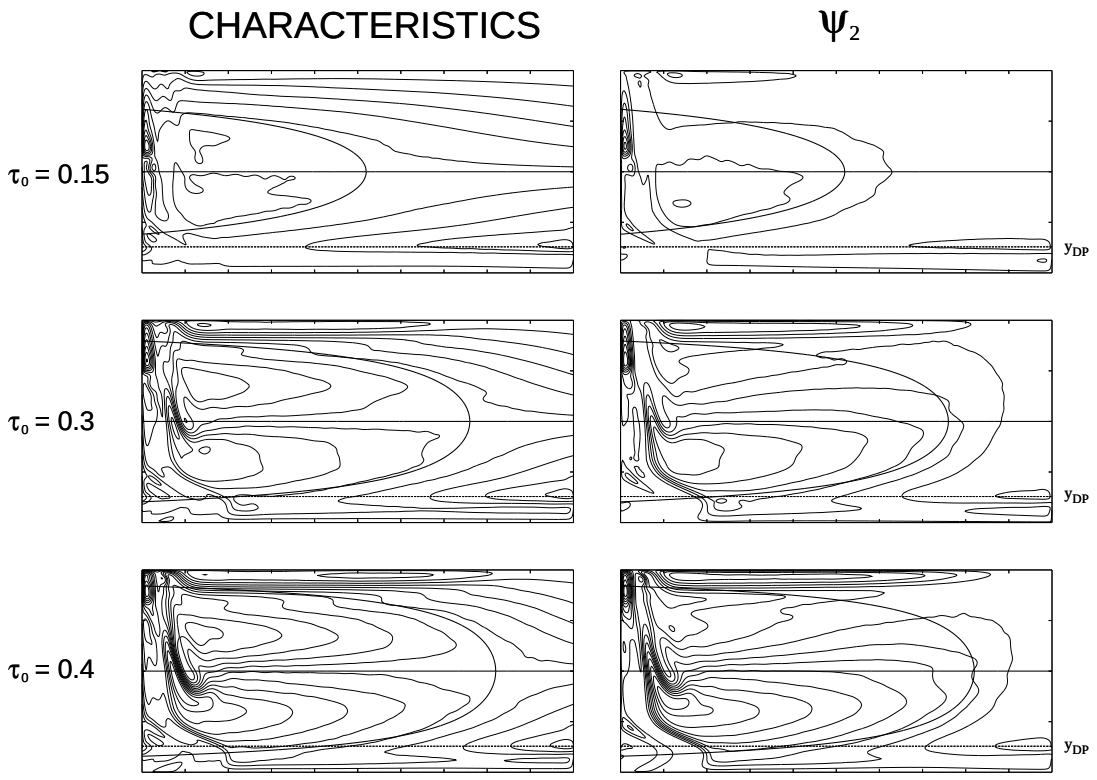

Figure 2–5: Characteristics and ψ_2 contours for three different values of the wind stress amplitude (τ_0) in the observed saturation regime. The analytic separatrix computed with $\psi_B = \psi_{\rm Sverdrup}$ from (2.1) is represented by a thick solid line in each panel.

5 also shows the contours of the characteristic function (2.3) computed with the time averaged ψ_B field. In the basin part, away from the western boundary, the analytic separatrix (superimposed on the contours of Θ in Fig. 2–5) matches the

observed division between blocked and free contours. This results since the time average barotropic solution remains in Sverdrup balance for the large scale interior circulation north of $y_{\rm DP}$. The baroclinic structure, on the other hand, is significantly altered relative to the theory. Because of this, (2.11) no longer follows from (2.10) and (2.13) becomes an overestimate. That is, there is a reduction in $T_{\rm saturation}$ compared to the theory (Fig. 2–4). Below, we show this to be related to an eddy forcing of the lower layer.

To investigate the influence of transient eddies on our numerical simulations, we perform a time decomposition of (2.4) and (2.5) at statistical equilibrium. Ignoring dissipation terms,

$$\mathrm{J}(\overline{\psi_1}, \overline{\nabla^2\psi_1}) + \mathrm{J}\overline{(\psi_1', \nabla^2\psi_1')} + F_1\left(\mathrm{J}(\overline{\psi_1}, \overline{\psi_2}) + \mathrm{J}\overline{(\psi_1', \psi_2')}\right) + \beta\partial_x\overline{\psi_1} = \overline{\text{Forcing}} \quad (2.15)$$

$$\mathrm{J}(\overline{\psi_2}, \overline{\nabla^2\psi_2}) + \mathrm{J}\overline{(\psi_2', \nabla^2\psi_2')} + F_2\left(\mathrm{J}(\overline{\psi_1}, \overline{\psi_2}) + \mathrm{J}\overline{(\psi_1', \psi_2')}\right) + \beta\partial_x\overline{\psi_2} = 0, \quad (2.16)$$

where overbars denote time averages and primes denote transients. Note that the term involving $\mathrm{J}(\overline{\psi_2}, h_{\rm b})$ has been omitted since $h_{\rm b}$ is zero in the interior of the domain. Note also that (2.16) can be thought of as a generalization of the characteristic equation (2.2). A scale analysis suggests that eddy advection of stretching vorticity should dominate over relative vorticity advection [cf., *Pedlosky*, 1996]. Indeed, long time averages (200 yr) of our model bear this out: $F_2\mathrm{J}\overline{(\psi_1', \psi_2')}$ clearly dominates in the region of blocked characteristics in the lower layer and the characteristic equation (2.2) becomes

$$\mathrm{J}\left(\overline{\psi_2}, \overline{\Theta}\right) = -F_2\mathrm{J}\overline{(\psi_1', \psi_2')}. \quad (2.17)$$

In the upper layer, the eddy activity is much stronger and longer averages are needed in order to smooth out the noise produced by the advection of relative vorticity. Nevertheless, here again, stretching vorticity dominates in the region of interest. This symmetry between the two layers explains why the time averaged barotropic Sverdrup balance still applies, consistent with standard theory.

Zonal jets

The modified baroclinic structure of the flow appears related to the presence of zonal jets in the instantaneous ψ fields. For instance, Fig. 2–6 shows a snapshot of the potential vorticity in both layers for $\tau_0 = 0.15$ N/m^2 (corresponding to the upper panels of Fig. 2–5). A clear signal of zonal jets is visible in both layers. These jets are expected in β-plane turbulence [*Rhines*, 1975] and have been found both observationally in satellite altimetry data [*Maximenko et al.*, 2005] and numerically [e.g., *Panetta*, 1993; *Nakano and Hasumi*, 2005; *Nadiga*, 2006]. From Fig. 2–6, we see that the jets extend beyond the separatrix and over the region of blocked contours where $\psi_2 \neq 0$ (cf. Fig.2–5).

It is important to note that jets not only appear for the basin part of the ACC circulation but are also observed in the closed basin configuration. Figure 2–7 shows the mean streamfunctions obtained with the Southern Ocean configuration and the closed-basin configuration with and without bottom topography. As before, the similarity between the ACC and closed-basin with topography geometries is evident. This indicates that the modifications to the baroclinic structure by transient eddies are not due to the opening of Drake Passage. The greater change occurs when bottom topography is removed in the closed basin case. Indeed, as *Rhines*

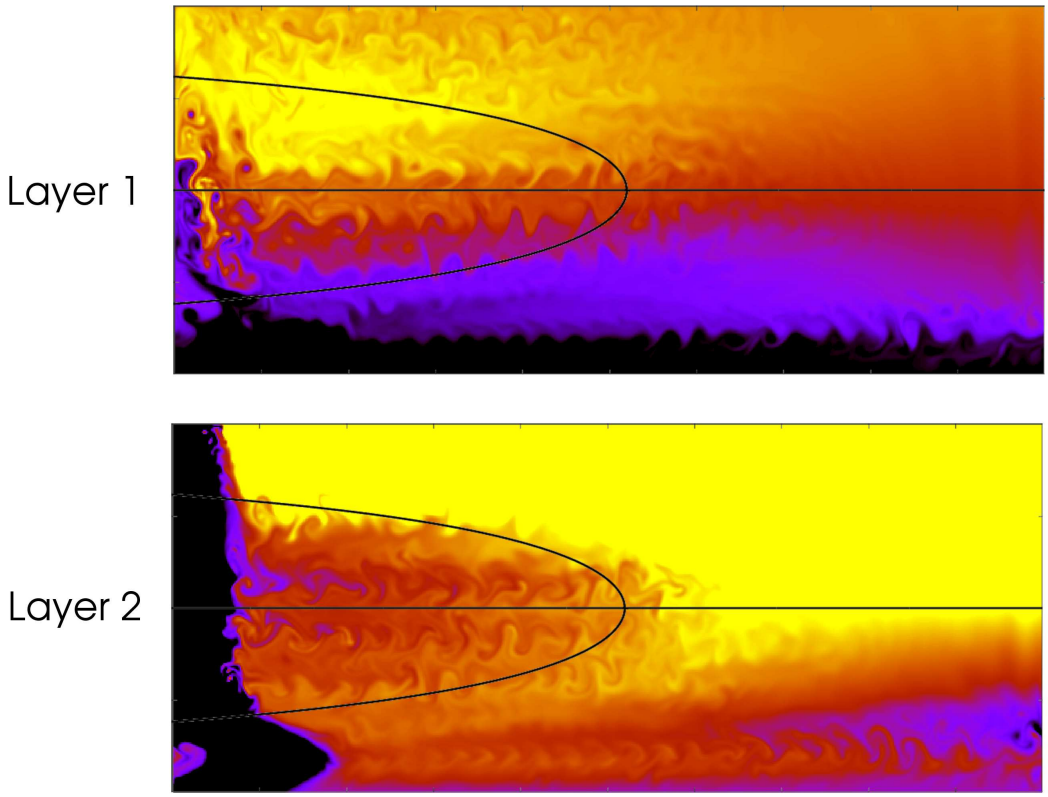

Figure 2–6: Instantaneous fields of potential vorticity in both layers. A clear signature of zonal jets is visible. The solid line is the analytic separatrix.

and Schopp [1991] observed, there is essentially no flow over blocked characteristics in this case. Moreover, the strength of the jets is reduced and their distribution becomes symmetric about the center latitude. This suggests that it is the bottom topography which leads to a southward displacement and increase in strength of the jets. We speculate that this is related to our continental rise topography causing lower layer potential vorticity contours to bend northward near the boundary. As such, contours in the southern portion of the domain — where the jets are strong

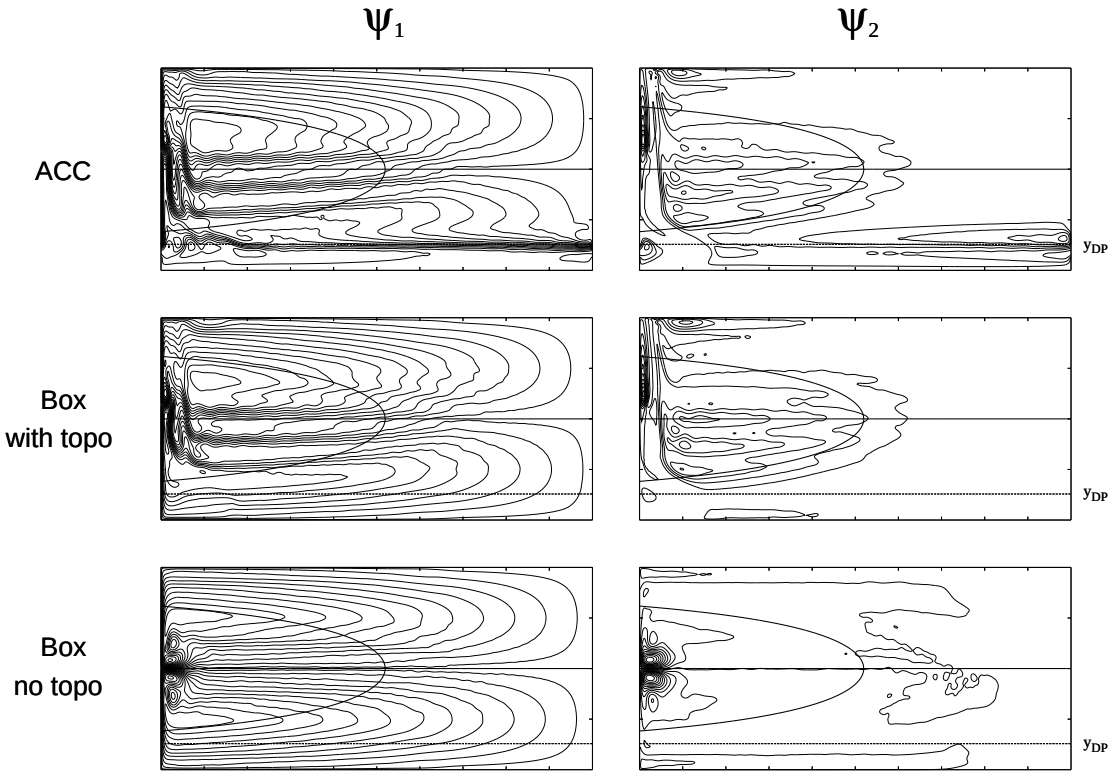

Figure 2–7: Mean streamfunctions for three different geometries: ACC , Box with topography and Box without topography. Note that the averages are taken over 30 years rather than the 200 years for Fig. 2–5. Over this smaller time interval, zonal jets are clearly visible in the streamfunctions. Thicker lines in each panel correspond to the analytic separatrix.

— extend back to the western boundary confluence region, where eddy activity is intense. In other words, it seems plausible that information from the confluence region is communicated into the interior along these contours. This is consistent with jets forming in the southern gyre in the case with topography and contrasts the flat bottom case (cf. Fig. 2–7) where eddy influences are limited to a narrow region near the center latitude.

Associated with the southward displacement of the jets is an increase in eddy activity which in turn leads to a change in the baroclinic structure of the flow. As we saw above, in the ACC geometry, this leads to a reduction of $T_{\text{saturation}}$. In the Box geometry, an asymmetry between the northern and southern gyres results. For instance, in the upper layer, the northern gyre transport is ∼72 Sv while in the southern gyre it is only ∼46 Sv. This is consistent with the premature ACC transport saturation [3] seen in Fig. 2–4.

Transport specification from the model results

The modified baroclinic structure of the flow east of x_0 implied (2.11) no longer to follow from (2.10). We now ask whether (2.10) can nonetheless be used to compute T_{Basin}. Fig 2–8 compares T_{Basin} calculated using (2.10) and model output to the total transport. The two curves follow one another, except for an offset approximately equal to T_{Channel}. This is consistent with an inspection of mean ψ_1 contours, which reveals that $T_w \approx 0$ for all wind stress amplitudes (not shown). Note, however that the x-position seperating recirculating contours from those feeding the ACC need not correspond precisely to x_0. Small errors in the western limit of the integral (2.10) do not have a large effect on the transport. This is because the southward flux across y_{DP} in the upper layer is relatively small in the region where the lower layer is in motion (i.e., near x_0). Because of this, (2.10) remains useful for estimating T_{Basin} even when eddy effects are prevalent.

[3] Note that for a Drake Passage opening in the north of the basin, we would expect a higher saturation phase.

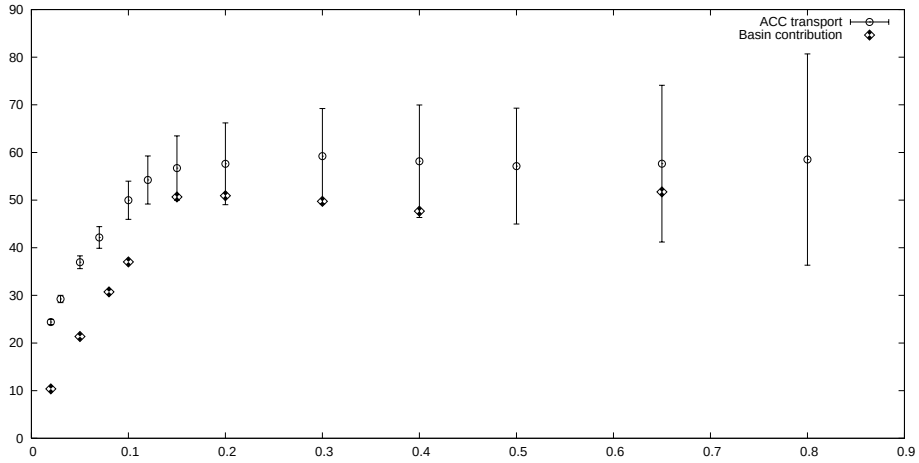

Figure 2–8: T_{basin} as computed with Eq. (2.10) and simulated ψ_1 fields compared to the mean transport presented in Fig. 2–4. Note that, for low wind stress we choose a x_0 to be just east of the topography on $y = y_{DP}$.

2.4.2 Robustness

Below, we test the sensitivity of our numerical simulations to different parameters affecting the transport. For example, the analytic model predicts three main factors setting the basin contribution: 1) L_x will affect how steep the initial Stommel growth will be, 2) the distance between the maximum of the wind forcing ($L_y/2$ in our case) and the Drake Passage northern latitude band (y_{DP}) will determine the value the saturation phase and 3) the ocean depth and Rossby radius also affect the saturation level. The influence of adding bottom topography in the interior of the basin is also considered.

We begin with the influence of the basin length. Figure 2–9 presents results obtained for three different basin lengths: $[4 \times 10]$ which has the same dimensions as in Fig. 2–4, $[4 \times 5]$, where the basin length has been cut by half and $[4 \times 20]$, where the basin length has been doubled.

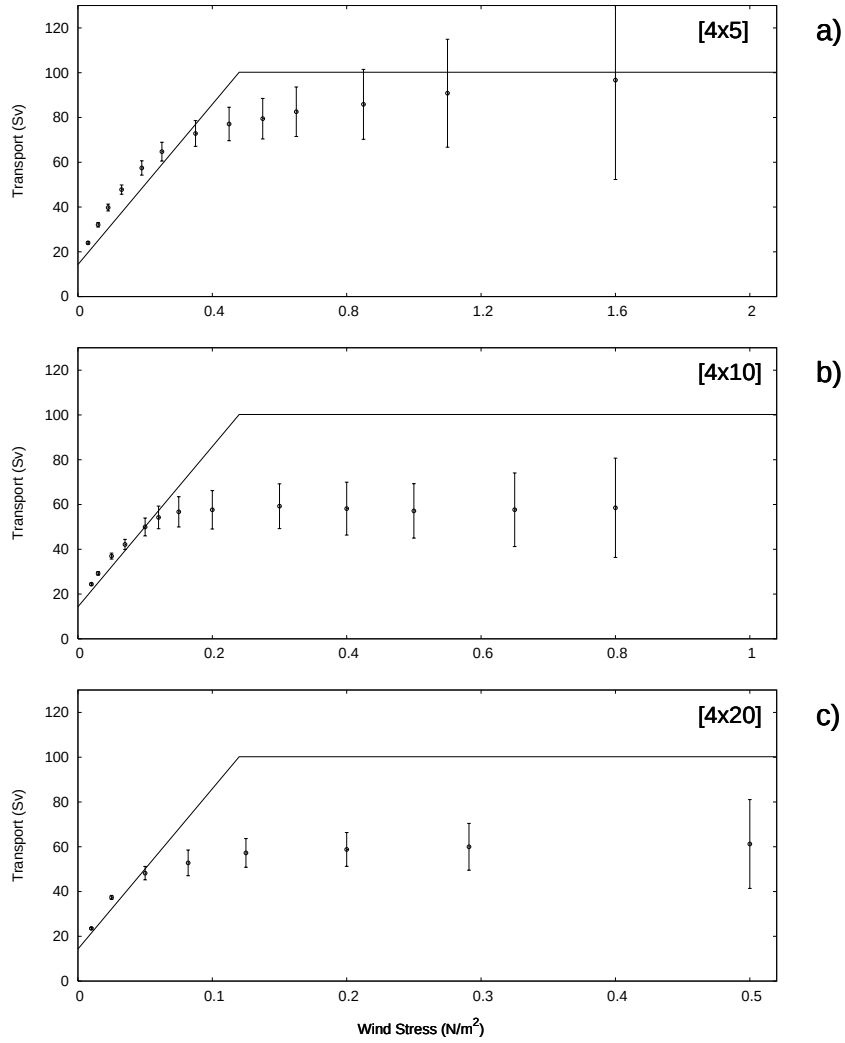

Figure 2–9: Mean circumpolar transport as a function of the wind stress amplitude for three basin lengths: a) $[4 \times 5] = [3840\text{km} \times 4800\text{km}]$, b) $[4 \times 10] = [3840\text{km} \times 9600\text{km}]$ (already presented in Fig. 2–4) and c) $[4 \times 20] = [3840\text{km} \times 19200\text{km}]$. Note that the wind stress scale varies between panels. Also shown are standard deviations and the analytic predictions.

Results for $[4 \times 20]$ are very similar to $[4 \times 10]$. There is a non-zero minimum at very weak wind stress followed by two distinct circulation regimes at stronger wind stress: a growing phase that fits Stommel's prediction and a saturation phase. The latter occurs at lower τ_0 than predicted by the theory and, again, this is due to the effect of transient eddies (not shown). On the other hand, the $[4 \times 5]$ case is significantly different. Its growing phase is steeper than Stommel's prediction while its saturation phase seems to fit the analytic prediction. In the following, we argue that these differences are related to the effects of an inertial recirculation at the western boundary. This effect is more significant for smaller domains and plays a lesser role when L_x is increased.

The inertial recirculation

We first focus on the weak wind stress regime, where Stommel's prediction underestimates the initial growing phase (Fig. 2–9a). Figure 2–10 shows a comparison between the upper layer streamfunctions in the ACC and Box configurations at weak wind stress for the $[4 \times 5]$ domain size. In the closed basin case (upper panel), strong eddy activity at the confluence of the two boundary currents creates an inertial recirculation on the western side of the basin. When Drake Passage is opened (lower panel), some of the streamlines associated with this recirculation appear to unfold and add to the basin contribution. To illustrate this idea, we define the curve C (thick latitudinal line in each panel of Fig. 2–10) and compute the mass flux across it. In both cases, this flux corresponds approximately to T_{Stommel} (cf., Section 2.3). That the circumpolar transport is larger that T_{Stommel} is then related to additional

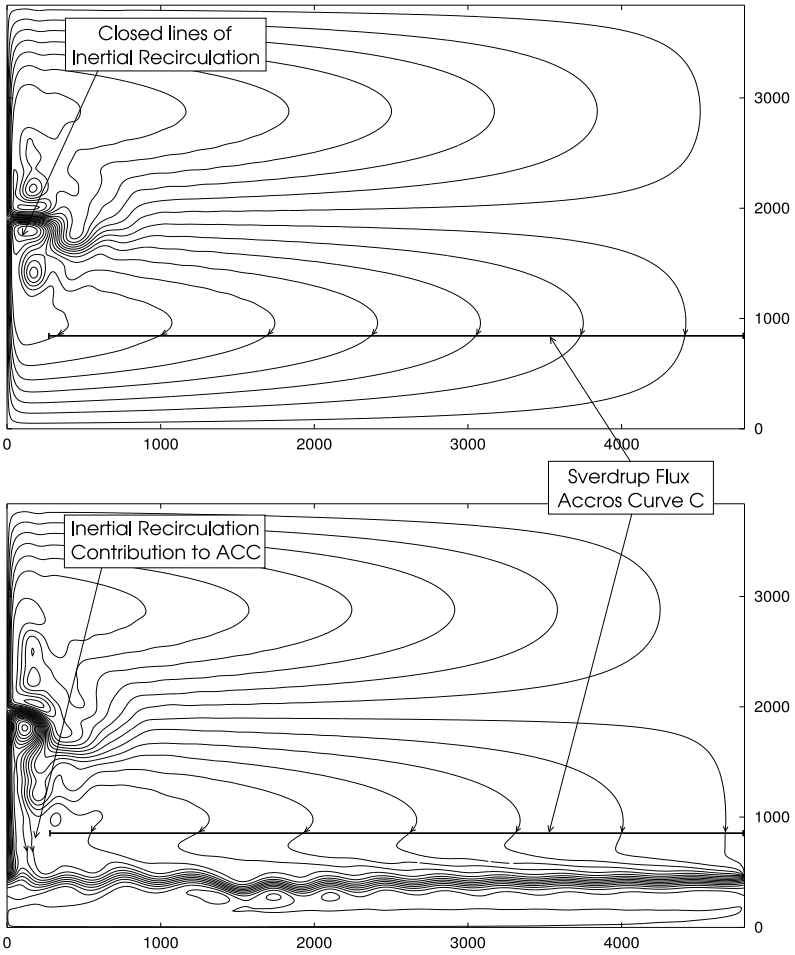

Figure 2–10: Contribution of the inertial recirculation to the circumpolar transport with the $[4 \times 5]$ domain size at weak wind stress ($\tau_0 = 0.06$ N/m^2).

streamlines entering Drake Passage to the west of C. Further evidence that the underestimate of Stommel's prediction is related to the inertial recirculation comes from considering the Box case. There, the total upper layer transport of the southern gyre also increases with τ_0 at a rate faster than T_{Stommel} and similar to what is seen in Fig. 2–9a (not shown).

In sum, for small L_x, we end up with two competing effects: inertial effects increase the transport while eddy effects tend to lower $T_{\text{saturation}}$. Therefore, the apparent fit between the observed and predicted saturation values in the $[4 \times 5]$ case is most likely due to these two compensating effects. However, the strength of the inertial recirculation does not depend strongly on the basin length (not shown), whereas Stommel's contribution does. Therefore, as the basin length is increased, the inertial recirculation will become negligible in comparison to the Sverdrup flow entering the channel region. We emphasize that the inertial recirculation influence is probably limited in the actual Southern Ocean considering its vast zonal extent. That this effect is weak for $[4 \times 20]$, which has dimensions close to the Southern Ocean, supports this claim.

Influence of L_ρ

Figure 2–11 shows the transport values obtained when varying the Rossby radius to test its influence on the saturation level. We chose large basin dimensions $[4 \times 10]$ to avoid the superfluous effect of the inertial recirculation. The horizontal grid spacing is kept at $\Delta x \cong L_\rho/2$ so that eddies have similar resolution in each case. For a given Rossby radius, we compute the average value of four experiments performed with different wind stress amplitudes (τ_0) taken in the saturation regime. Moreover, the wind stress amplitudes are chosen so that the same set of four separatrix contours is obtained for each L_ρ. Figure 2–11 shows that the relationship between the saturation value and L_ρ is approximately quadratic, as predicted by Eq. 2.13. However, comparing results with this analytic prediction shows that the premature ACC transport saturation seen in Fig. 2–4 is also observed for all chosen

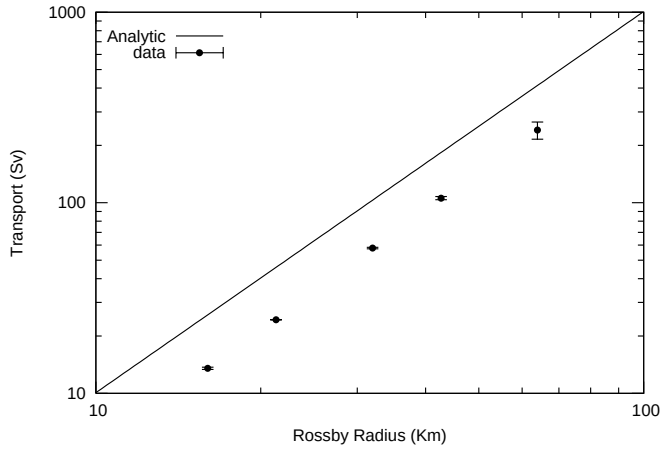

Figure 2–11: Mean and standard deviation of the transport saturation value (dots) as a function of L_ρ. Note that both scales are logarithmic. Also shown is the analytic prediction Eq. 2.13.

values of L_ρ. This suggests that the effect of transient eddies on the transport is independent of the Rossby radius.

The addition of a mid basin ridge

Apart from the Scotia Ridge, the ACC encounters other major topographic obstacles, e.g., the Kerguelen Plateau and the Pacific–Antarctic Ridge. *Hughes* [2002] argued that the transport depends on the relative amount of form stress falling across Scotia Ridge, i.e. as opposed to across other topography. On the other hand, *Tansley and Marshall* [2001] tested the effect of downstream topography on the circumpolar transport with basin dimensions similar to a $[2 \times 5]$ domain and found it to be rather small and unpredictable. We now revisit this experiment in the context of the much larger $[4 \times 20]$ basin. The topography added is a 2 km high meridionally oriented Gaussian ridge at $L_x/2$. Fig. 2–12 shows the transport values obtained in this experiment. Few changes are observed compared to the case without the ridge:

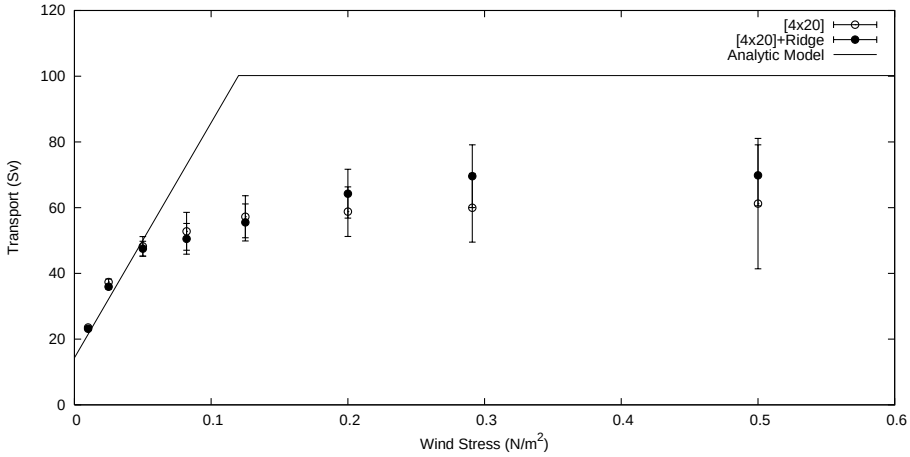

Figure 2–12: Mean circumpolar transport as a function of the wind stress for the $[4 \times 20]$ ACC geometry with and without a 2 km high meridionally oriented Gaussian ridge in the middle of the basin.

the main difference is that for τ_0 values greater than 0.2 N/m^2, saturation transport are raised slightly (factor of $\sim$15%). Fig. 2–13 shows the streamfunctions and the characteristic contours with and without the mid basin ridge for wind forcing strength $\tau_0 = 0.2$ N/m^2. Note that the introduction of topography in the basin interior makes the characteristic problem more subtle. Following Dewar *Dewar* [1998] one can define characteristics by assuming the lower layer to be at rest (Θ_{topo}, Fig 2–13g). The ψ_1 field then follows from the Sverdrup relation and the rest state potential vorticity field for the lower layer defines characteristics. Where these are blocked (and ignoring eddy effects) the assumption of a motionless lower layer is consistent. Where they are closed, one expects circulation to develop in the lower layer. A comparison of 2–13d,g is consistent with this. Interestingly, the small increase in transport seen for $\tau_0 \geq 0.2$ Fig. 2–12 appears to be associated with the closed contours overlying the ridge. The lower layer circualation associated with this feature is considerably

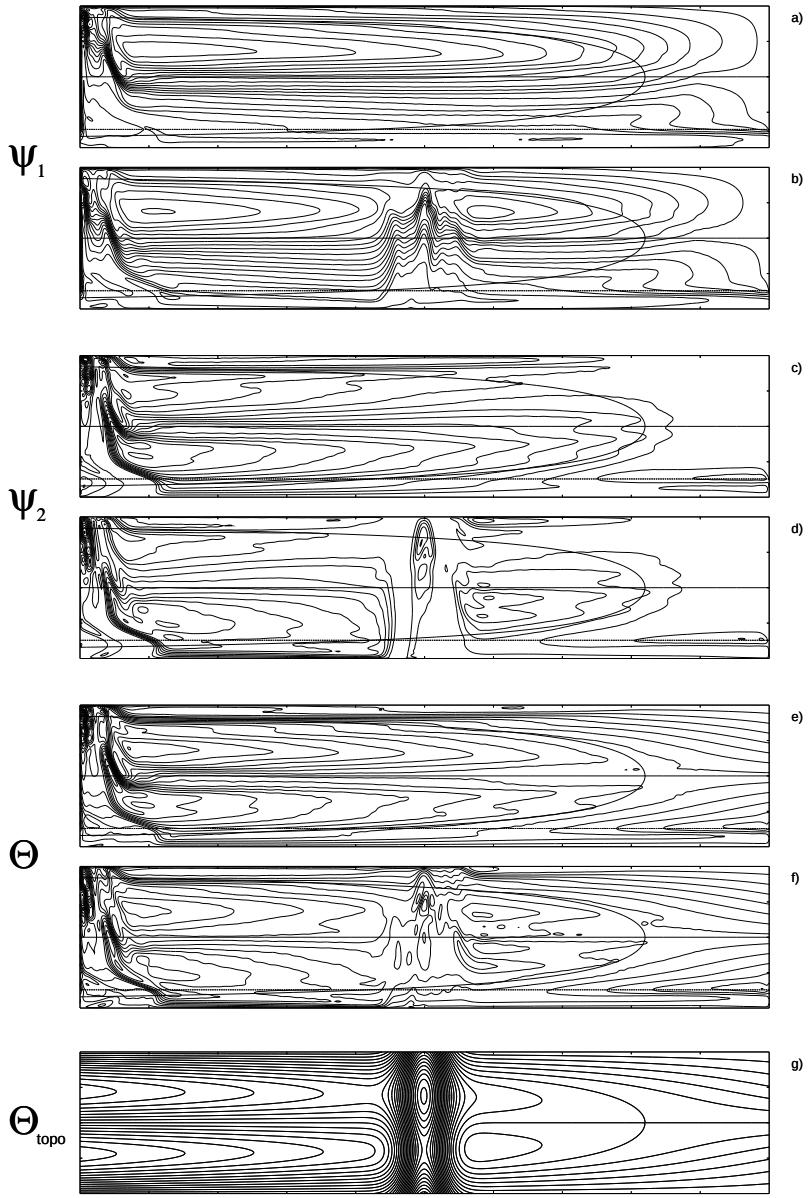

Figure 2–13: Contours of ψ_1, ψ_2 and Θ for the $[4 \times 20]$ basin case at $\tau_0 = 0.2$ N/m^2 with (b, d and f) and without (a, c and e) a 2 km high mid-basin ridge. Pannel g) shows $\Theta_{\rm topo} = \beta y + \frac{1}{L_\rho^2}\psi_B + \frac{f_0}{H_2}h_{\rm b}$.

smaller for $\tau_0 = 0.1$ and is absent altogether for weaker forcing. It then seems possible that other choices of topography (i.e., that evoke closed characteristics) may lead to larger discrepancies between simulations and theory. For our choice of topography, however, the effect of the ridge appears localized to its longitudes. This contrasts the "continental rise" topography which, as we have seen, affects the strength and distubution of the zonal jets and leads to lower layer motion outside of the seperatrix contour.

Distance between $y_{\rm DP}$ and $L_y/2$

As mentionned in the introduction, this article focuses on basin-like dynamics. As such, we chose geometries for which Drake Passage occupies only a small range of latitudes. By this choice, we wanted to isolate the basin contribution in order to analyse its behaviour. It can be argued however that the actual width of the Drake Passage is larger and that the distance between $y_{\rm DP}$ and $L_y/2$ is smaller than what we have used until now. Coming back to the analytic model saturation regime (see Section 2.3), the sum of the channel and basin contributions gives

$$\begin{aligned} T &= H\beta L_\rho^2 \left[L_y/2 - y_{\rm DP} + L_{\rm gap} \right] \\ &= H\beta L_\rho^2 \left[L_y/2 - y_{\rm south} \right], \end{aligned} \tag{2.18}$$

where $y_{\rm south}$ is the southern edge of Drake Passage. In other words, in the saturation regime, the relative contributions of the channel and basin are proportional to their meridional extents. Thus, the analytic theory predicts no change in the total transport saturation value as $L_{\rm gap}$ is increased by moving $y_{\rm DP}$ northward.

Figure 2–14 shows analytic predictions and numerical results obtained for a progressive widening of the gap in the $[4 \times 10]$ geometry. We open the channel from

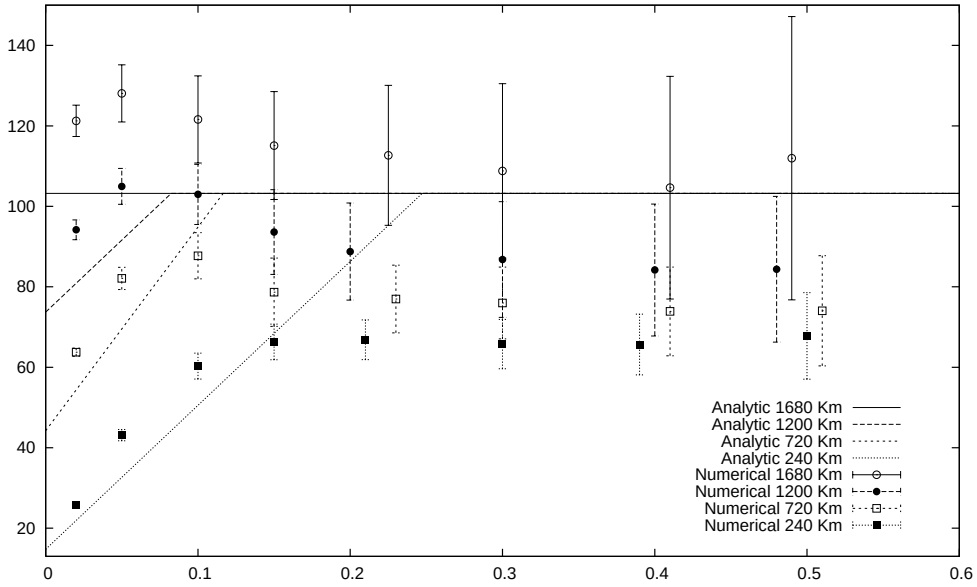

Figure 2–14: Mean circumpolar transport and standard deviation as a function of the wind stress amplitude in the $[4 \times 10]$ geometry for four different gap widths: $L_{\rm gap} = 240$km, 720km, 1200km and 1680km. Also shown are their respective analytic predictions. Note that the width of the gaussian ridge has been narrowed for this experiment to facilitate the match between the tip of the peninsula and the bottom topography. This results in a slight increase in transport in the $L_{\rm gap} = 240$km case (cf. Fig. 2–4)

.

$L_{\rm gap} = 240$km — the value used until now — to $L_{\rm gap} = 1680$km, which corresponds to $y_{\rm DP} = L_y/2$. Larger values of $y_{\rm DP}$ lead to saturation values closer to the analytic prediction. This is consistent with our earlier results. The undersaturation seen for narrow gaps was associated with the basin contribution being reduced relative to the theory. For wide gaps, the theoretical basin contribution is small and reducing it has little effect on the total transport.

The case $L_{\text{gap}} = 1680$km is of particular interest since T_{Basin} is identically zero. Figure 2–14 shows that the transport overshoots the analytic prediction (2.8) at low τ_0 and then slowly decreases until saturating near the analytic value for stronger forcing. This result differs drastically from the pure channel case (i.e,. with a wall at $y = L_y/2$). Indeed, in their channel plus ridge geometry, *Tansley and Marshall* [2001] found the transport to increase rapidly for weak forcing and then follow a power law ($\tau_0^{1/13}$, see their Fig. 11) at stronger forcing. Thus, for forcings corresponding to our saturation regime, the pure channel gives transports well in excess of (2.8), whereas our results do not. This suggest that the northern gyre plays an important role even when $T_{\text{Basin}} = 0$. We speculate that the presence of the adjacent gyre serves as a source of eddies for the channel latitudes. With this source of eddies, increased interface tilt (fueling increased baroclinic instability) is not required to close the meridional circulation, as assumed in channel-like theories of ACC transport (cf. Section 2.3). Conversely, for weak forcing, channel-like dynamics appear to dominate so that the interface tilt (and transport) increases with the forcing strength.

The Southern Ocean likely lies between the $L_{\text{gap}} = 240$km and $L_{\text{gap}} = 1680$km extremes and a behavior intermediate to the two is expected. Indeed, both the $L_{\text{gap}} = 720$km and $L_{\text{gap}} = 1200$km cases exhibit such behavior. For example, each curve shows a Stommel regime at weak forcing, followed by a weak overshoot and undersaturation for stronger forcing.

2.5 Conclusion

The main objective of this paper was to revisit Stommel's idea that basin dynamics play a significant role in determining the ACC transport. We develop an

analytic model in which the total transport is comprised of basin and channel contributions. The channel contribution is determined by marginal stability argument proposed by *Straub* [1993] and is independent of the forcing strength. The basin contribution depends critically on the geometry of the separatrix characteristic. Two regimes result. For weak forcing the separatrix extends across the basin and for strong forcing it crosses $y = y_{\mathrm{DP}}$. This defines $x = x_0$, which is a point just east of the western boundary layer (on $y = y_{\mathrm{DP}}$) in the weak forcing regime and the point at which the separatrix crosses $y = y_{\mathrm{DP}}$ for strong forcing. The basin contribution then corresponds to the upper layer portion of the Sverdrup flux across $y = y_{\mathrm{DP}}$ and east of $x = x_0$. For weak forcing, it increases linearly with τ_0, following Stommel's (1957) prediction. For strong forcing, transport saturates. That is, increasing winds causes both an increase in the total Sverdrup flux across y_{DP} and an eastward migration of x_0. The two effects cancel and T_{Basin} becomes independent of wind strength. Physically, instead of adding to the circumpolar flow, stronger forcing feeds a recirculation west of x_0.

Numerical results are broadly consistent with the analytic model, though some discrepancies are observed. This is not surprising given the turbulent nature of the flow. The first main discrepancy relates to zonal jets. Transient eddies modify the characteristic equation (2.2), allowing for lower layer flow outside of the separatrix. The barotropic transport and by extention the geometry of the characteristics are, however, not strongly affected by the eddies. Instead, some of the Sverdrup flux east of x_0 occurs in the lower layer and T_{basin} is reduced relative to our analytic estimate. A second discrepancy occurs in small domains, where inertial effects add to T_{basin}.

Comparison between closed basin and Southern Ocean configurations suggests that some of the streamlines associated with the inertial recirculation in the Box case unfold and add to the circumpolar flow when Drake Passage is opened. The overall effect is then to increase the transport in both the weak and strong wind regimes. However, this effect is negligible for large basin lengths where the Sverdrup flux is large compared to this inertial recirculation. In sum, for large basins the saturation value is lower than the analytic prediction due to transient eddy effects, while for small basins inertial effects are more important and transport is closer to the analytic prediction.

Various other robustness tests were also carried out. In particular, we tested robustness of our results to i) the presence of an additional ridge far from the western boundary, ii) variations in the strength of the stratification and iii) the width of the gap at Drake Passage. Generally speaking results remained broadly consistent with the theory. While the additional meridional ridge affected the solution locally, transport values were much as before. Simulations over a range of Rossby radii showed a remarkable consistency with the theory (which has transport scaling like the square of the Rossby radius). Finally, although the width of Drake Passage did influence the results somewhat, transports nonetheless remained close to predicted values. Disagreement was largest for weak forcing, where model transport was larger than theory, but was small elsewhere.

Obviously, the Southern Ocean is far more complex than is our simple two layer quasigeostrophic model and many effects we neglected may be important to determining the observed transport. Even in the quasigeostrophic context, effects relating

to stratification, surface density, vertical resolution, rough topography, bottom drag and horizontal dissipation may all play a role. Additionally, realistic wind fields will certainly affect results and equations such as (2.13) should not be applied naively. For example, in the case of a nonsymmetric wind field, $L_y/2$ the y-position of $\Theta_{\text{separatrix}}$ at $x = L_x$ need not correspond to the latitude of maximum zonally averaged wind stress. Despite these caveats, the clear correspondence between our Box and ACC geometries stongly suggests that gyre-like dynamics are fundamental to the Antarctic Circumpolar Current.

CHAPTER 3

Influence of wind stress, wind stress curl, and bottom friction on the transport of a model Antarctic Circumpolar Current

This chapter presents further robustness analysis of the analytic model. It is based on a paper that will be submitted to Journal of Physical Oceanography soon after the submission of this thesis.

Influence of wind stress, wind stress curl, and bottom friction on the transport of a model Antarctic Circumpolar Current

Louis-Philippe Nadeau[1] and David N. Straub[1]

[1]Department of Atmospheric and Oceanic Sciences, McGill University, Montréal, QC, Canada

Abstract

Recent numerical simulations support a conceptual model suggesting that the transport in a quasigeostrophic model of the Antarctic Circumpolar Current (ACC) becomes independent of wind forcing amplitude in a strongly forced regime. In this regime, circumpolar transport is fed by a portion of the upper ocean Sverdrup flux into Drake Passage latitudes. Here, additional simulations are considered to test the robustness of this result; specifically, the role of bottom friction and the relative roles of the wind stress and wind stress curl in Drake Passage latitudes are considered. Except for very weak wind stress curl, time averaged circumpolar streamlines in the upper ocean support the idea that the ACC is linked to the southward Sverdrup flux north of the model Drake Passage. How this Sverdrup flux is partitioned between circumpolar and recirculating streamlines, however, is found to be sensitive to both the bottom friction coefficient and the relative strength of the curl-containing portion of the wind stress field and the magnitude of the wind stress itself in the Drake Passage latitude band. Related to this is an eddy-driven abyssal recirculation gyre. This is also sensitive to bottom friction and to the wind stress to wind stress curl ratio, and can extend into the upper ocean (i.e., diverting a portion of the southward Sverdrup flux —that might otherwise feed the ACC— into a recirculation).

The weakly forced regime is also considered, as are the relative roles of large and small scale eddies in transporting momentum vertically through the water column. It is found that the vertical momentum flux of mesoscale eddies at Drake Passage

latitudes can be used to distinguish between different regimes: they transmit momentum upwards when the dynamics is dominated by the large scale recirculation gyre and have a downward flux when it is not.

3.1 Introduction

Various factors, such as topographic form drag, interfacial form drag, wind and buoyancy forcing, diapycnal mixing, bottom drag and mesoscale eddies conspire to determine the eastward transport of the Antacrtic Circumpolar Current (ACC). There has long been a concensus that topographic and interfacial form drag are key to closing the momentum or angular momentum budget. There also appears to be a concensus that both stratification [e.g., *Gnanadesikan and Hallberg*, 2000; *Hallberg and Gnanadesikan*, 2001] and mesoscale eddies play a crucial role [e.g., *Doos and Webb*, 1994; *Henning and Vallis*, 2005; *Hallberg and Gnanadesikan*, 2006]. An exception is in a regime where forcing is weak and dyapycnal fluxes are strong. In this regime, transients appear less important, [*Hallberg and Gnanadesikan*, 2001]. The importance or relative importance of other factors is less clear. For example, the relative roles of the typically smaller scale transient eddies and the typically larger scale standing eddies in the vertical transport of momentum is unclear. *Treguier and McWilliams* [1990] showed that standing eddies are dominant in the momentum balance when increasing the wavelength of the topography. In this case, the zonal transport is decreased significantly. Also unclear are the relative roles of the wind stress curl compared to the wind stress itself.

Of particular relevance to us is the study of *Hallberg and Gnanadesikan* [2006]. Using a 1/6° resolution primitive equation model in a realistic Southern Ocean geometry, they show that an increase or decrease of 20% in the wind stress results in changes of less than 3% to the zonal transport. This suggests that the ACC transport is in a saturation regime. Saturation regimes are also found in more idealized quasi-geostrophic models, which do not allow for feedbacks between the wind forcing and the stratification [e.g., *Tansley and Marshall*, 2001; *Hogg and Blundell*, 2006]. *Hogg and Blundell* [2006] considered a zonally reconnecting channel with topography and attributed this behavior to eddy saturation. Eddy saturation theories [e.g., *Straub*, 1993; *Marshall et al.*, 1993] suggest a regime where the interface slope is approximately given by the condition of baroclinic instability. This, in turn, determines (the baroclinic portion of) the transport. When a basin region is also present to the north of the reconnecting channel (e.g., by adding eastern and western boundaries), a saturation is observed [e.g., *Tansley and Marshall*, 2001]. In this case, however, the link with eddy saturation theories is less clear. In a recent set of experiments, *Nadeau and Straub* [2009] (hereafter, NS09) showed that saturation in this setting could instead be explained by appealing to Sverdrup dynamics in the basin-like portion of the domain, and by taking into account the vertical structure of the southward Sverdrup flux into Drake Passage latitudes.

That Sverdrup dynamics clearly break down in the channel portion of the Southern Ocean has led to its often being dismissed as altogether irrelevant to the ACC; however,the possibility remains that basin-like dynamics in regions adjacent to the ACC may nonetheless play a significant role. The idea that this may be the case

dates back to *Stommel* [1957], *Wyrtki* [1960] and *Gill* [1968]. They suggest scenarios whereby a southward Sverdrup flux turns eastward, joining —or in fact forming— the ACC. In Stommel's and Wyrtki's picture, there is no band of unblocked latitude circles, whereas in Gill's picture, a 'channel region' (where Sverdrup dynamics do not apply) lies adjacent to a basin-like region (where Sverdrup dynamics do apply). We will refer to this general framework as 'Stommel's idea or model'.

Evidence supporting this picture comes from the clear east-west asymmetry of the ACC. For example, model simulations show the majority of the current to make a sharp northward turn just east of Drake Passage [e.g., *Killworth*, 1992; *Hallberg and Gnanadesikan*, 2006; *Mazloff et al.*, 2010]. This is consistent with Stommel's picture, whereby the ACC feeds into the Falkland-Malvinas Current. A similar northward turn feeding a western boundary region is also seen along the continental margin southeast of New Zealand. A recent series of experiments, *Allison et al.* [2010], used a general circulation model (GCM) to examine the effect of the Pacific and Indian basins. When these were removed (i.e., replaced with land north of Cape Horn), the transport was considerably reduced. We take this as further evidence suggesting an important role for basin dynamics in the ACC.

The analytic model of NS09 explains well the saturation behavior seen in their simple two layer quasigeostrophic model; however, their model simulations did not test for the possible effect of adding a zero-curl wind stress to the wind forcing profile. Basin dynamics are mainly determined by the wind stress curl, whereas channels dynamics also depend strongly on the wind stress itself. Thus, one might anticipate

that increasing the eastward wind stress in the channel (i.e., Drake Passage) latitudes will increase the 'channel contribution' to the total transport. In this paper, we investigate the effect of both the wind stress and the wind stress curl in a simple quasigeostrohic model with an idealized Southern Ocean geometry (a zonally reconnecting channel with walls to represent Patagonia and the Antarctic Peninsula).

A brief review of the analytic model of NS09 is presented below, and Section 2 then briefly describes the numerical model used for this study. Section 3.3 presents results. First, a study of the influence of the bottom drag is considered. We find that bottom drag influences the strength of a recirculation in the southwest portion of the domain (east of Drake Passage), and that this influences the transport. Following this, the relative roles of wind stress and wind stress curl are considered. For a fixed wind stress curl, adding an eastward wind stress increases the transport. Conversely, for a fixed wind stress magnitude in (the middle of) the Drake Passage latitude band, addition of a double gyre forcing is found to decrease the transport.

3.1.1 Analytic model

It is useful to first give a brief review (following NS09) of why saturation occurs in the strongly forced regime. In their two layer quasigeostrophic model, circumpolar flow was blocked in the lower layer by a Scotia-Ridge-like topography. Simulations comparing cases where Drake Passage was open with cases where it was not showed nearly identical circulation patterns over much of the region north of the model Drake Passage latitude band. Moreover, adjacent to Drake Passage latitudes and away from the western boundary region, the time averaged barotropic flow closely obeyed the Sverdrup relation. The Sverdrup flux into the Drake Passage latitude

band was entirely top-trapped for weak forcing, whereas for stronger forcing it was distributed over both layers in the western portion of the domain, and remained top-trapped in the east. A simple theoretical argument then suggested that only the top-trapped portion of the Sverdrup flux fed the circumpolar transport. This is unlike previous Sverdrup theories, in which all the southward Sverdrup flux is assumed to feed the ACC. Instead, that portion of the Sverdrup flux which is not top-trapped was assumed to feed a closed recirculation, which extends through both layers. As such, it does not add to the circumpolar transport (see Figure 1). Geostrophic

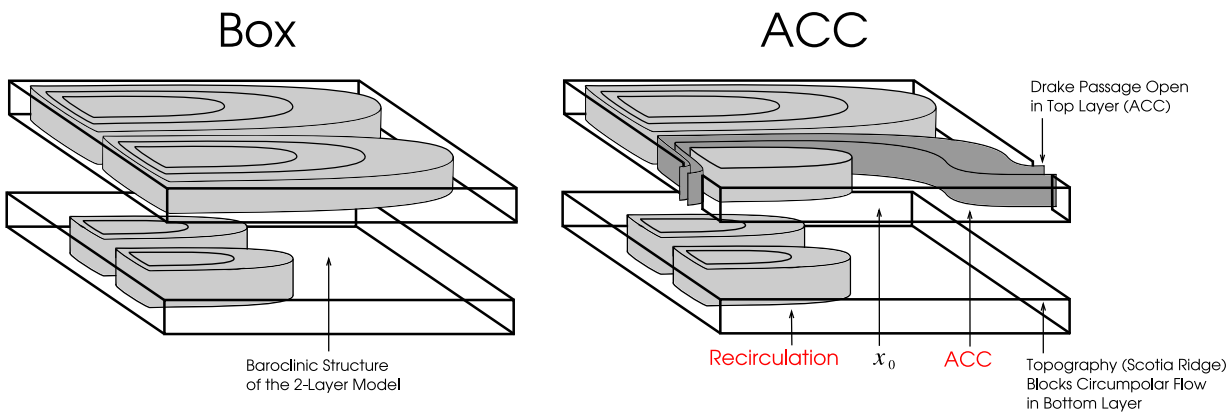

Figure 3–1: Sketch of the baroclinic circulation for the closed-basin (Box) geometry and a corresponding ACC geometry for the 2-layer case. Topography blocks circumpolar flow in the lower layer, so that the abyssal portion of the Sverdrup flux into Drake Passage latitudes feeds a closed recirculation. Associated with this is a ridge in the interface height field, which steers the upper layer flow in this region — so that it too feeds a recirculation.

contours were readily obtainable and determined the zonal position, x_0, separating the top-trapped part (to the east) from the rest of the Sverdrup flux entering the channel region. A 'basin' contribution to the ACC, T_{basin}, was then the zonal integral of the Sverdrup flux east of x_0. Simulations showed this to be a reasonable estimate; even in situations where eddies drove a weak abyssal flow east of x_0, the net basin contribution to the transport was nonetheless well represented by the simple theory.

The total circumpolar transport was then given by the sum of this 'basin' contribution with a 'channel' contribution, unrelated to the gyres:

$$T = T_{\text{channel}} + T_{\text{basin}}. \tag{3.1}$$

T_{channel} was found to roughly coincide with the analytic prediction of *Straub* [1993]. T_{basin} increased linearly with the forcing strength (in agreement with Stommel's idea) for weak forcing, and then reached a saturation value, T_{sat}, for stronger forcing. T_{sat} was given by

$$T_{\text{sat}} \sim \beta L_\rho^2 H L. \tag{3.2}$$

Here, β is the meridional derivative of the Coriolis parameter, f, H is the fluid depth, L_ρ is the Rossby radius and L is the meridional distance from the north side of Drake Passage to the zero wind stress curl line (lying further north; for simplicity, the wind stress is assumed to be a function of the meridional coordinate, y only).

3.2 Numerical model

The numerical experiments are performed using the 2-layer quasi-geostrophic model described in NS09. It is based on the quasi-geostrophic equations, truncated

to only two layers (or levels) in the vertical, *Pedlosky* [1996]:

$$D_t\left[\nabla^2\psi_1 - F_1(\psi_1-\psi_2) + \beta y - F_0\psi_1\right] = -A_h\nabla^6\psi_1 + \frac{\widehat{k}\cdot\nabla\times\boldsymbol{\tau}}{\rho_1 H_1} \quad (3.3)$$

$$D_t\left[\nabla^2\psi_2 + F_2(\psi_1-\psi_2) + \beta y + \frac{f_0}{H_2}h_{\rm b}\right] = -A_h\nabla^6\psi_2 - r\nabla^2\psi_2, \quad (3.4)$$

where $D_t() = \frac{\partial}{\partial t}() + \mathrm{J}[\psi,()]$ is the total time derivative, $F_0 = \frac{f_0^2}{gH_1}$, $F_1 = \frac{f_0^2}{g'H_1}$, $F_2 = \frac{f_0^2}{g'H_2}$, f_0 is the mean Coriolis parameter, g is the gravitational acceleration, $g' = g\frac{\Delta\rho}{\rho}$ is the reduced gravity, (H_1 and H_2) are layer thicknesses, $h_{\rm b}$ is bottom topography, A_h is a lateral bi-harmonic viscosity coefficient and r is a bottom drag coefficient.

Integration of the above equations involves solving an elliptic equation for each vertical mode at each time step; and for this, a multigrid method is used. Additionally, because the elliptic inversion in non-unique, additional mass and momentum conservation laws are needed to close the problem. We follow a precedure similar to that describe by *McWilliams et al.* [1978]. Specifically, the momentum budget is closed using the zonal momentum equation averaged over a latitude circle in the channel

$$\oint_0^{L_x}\left[D_t[u_{0k}] - f_0 v_{1k} - \beta y v_{0k} = -g\partial_x\eta_1 - \delta_{N,k} r u_{0k} - A_H\nabla^4 u_{0k} + \delta_{1,k}\frac{\boldsymbol{\tau}}{\rho_1 H_1}\right]dx \quad (3.5)$$

where $[u_0, v_0] = [-\partial_y\psi, \partial_x\psi]$ is the horizontal velocity and $\eta_k = \frac{f_0}{g_k}\psi_k$ is the interface height so that $\oint_0^{L_x}[\partial_x\eta_1]dx$ cancels. The perturbation meridional velocity, v_1, is taken from mass flux conservation across the latitude circle in channel

$$\oint_0^{L_x}\left[(H_k v_{1k}) - v_{0k}(\eta_k - \eta_{k-1})\right]dx = -\frac{d}{dt}\left[\iint_{\rm A}[\eta_k - \eta_{k-1}]dxdy\right], \quad (3.6)$$

where A is the area south of the latitude where the above integral is taken.

A limitation of quasigeostrophic models is that stratification is fixed. Even without buoyancy forcing, it is known that wind can affect stratification [e.g., *Hallberg and Gnanadesikan*, 2001; *Henning and Vallis*, 2005]. In turn, stratification is linked to transport. This indirect effect of wind forcing on ACC transport is absent in our model. On the other hand, the 2-layer quasigeostrophic framework is a simple comprehensible system for which it is easier to understand the basic behavior. It also allows us to cheaply perform a large number of eddy-permitting simulations. Model parameters can be found in Table 3–1.

Table 3–1: Model parameters

Parameter	Symbol	Value
Rossby deformation radius	L_ρ	16 and 32 km
Horizontal resolution	$\Delta x = \Delta y$	15 km
Length of channel	L_x	9600 km
Width of channel	L_y	3840 km
Width of Drake passage	L_{gap}	240 and 720 km
Position of $\nabla \times \tau = 0$	$L_y/2$	1920 km
Top layer	H_1	1200 m
Bottom layer	H_2	2800 m
Coriolis parameter	f_0	$-1.3 \cdot 10^{-4}$ s^{-1}
Beta parameter	β	$1.5 \cdot 10^{-11}$ m^{-1}s^{-1}
Gravitational acceleration	g	9.8 m/s^2
Reduced gravity	g'	0.02 and 0.005 m/s^2
Reference density	ρ_1	1035 kg/m^3
Bottom friction coefficient	r	0.5 to 10 $\times$ 10^{-7} s^{-1}
Bi harmonic dissipation coefficient	$A_h = \beta \cdot \Delta x^5$	$1.14 \cdot 10^{10}$ m^4/s

Topography is chosen to be a Gaussian ridge mimicking the Scotia Ridge, and is similar to that used in NS09. (A difference is that topography in NS09 included a continental rise along the eastern side of the Patagonia peninsula, and this is absent here.) The reference wind forcing is also similar to that used in NS09, that is,

$$\boldsymbol{\tau} = \widehat{i}\ \tau_0 \sin^2(\pi y/L_y). \tag{3.7}$$

A zero-curl (uniform eastward) wind stress will also be added to this reference profile in order to isolate the effect of the stress and the curl, respectively. The specific manner in which we alter the forcing will be described in section 3.3

3.3 Results

3.3.1 Bottom friction

In a flat bottom channel setting, bottom friction removes momentum input to the upper ocean by the wind. Increasing r then decreases the zonal transport. When topography is added, the effect of the bottom friction is less clear. *Hogg and Blundell* [2006] observed a 20% increase in transport when r was increased by a factor 2.5, and suggested that this phenomenon is due to eddy saturation (cf, discussion in the introduction). When continental barriers partially block the channel, NS09 suggest that T_{basin} is given by the upper-ocean-trapped portion of the southward Sverdrup flux into Drake Passage latitudes. An increase in the bottom drag might then be expected to decrease the strength of the lower layer recirculating gyre. As such, more bottom drag would seem to imply that more of the Sverdrup flux remains top-trapped, and thus, a larger T_{basin}. This would result in an increase in the saturation value of transport in the strongly forced regime. An analytic prediction is hard to

obtain in this case; however, qualitatively, one expects an increase in r to lead to larger saturation values for the transport. Below, results from a series of simulations forced using Eq. (3.7) and with varying coefficients, r, is presented.

Transport

Figures 3–2a,b show the zonal transport in the top and bottom layers, plotted as a function of the forcing amplitude and for different values of bottom friction. We take r =r = $10^{-7}\mathrm{Nm}^{-2}$ as a reference value, and consider experiments with $r = 0.5, 1, 2, \text{and} 10 \times$ r. For the reference simulation, transport has a similar behavior to that described in NS09. When forcing weak, transport increases more or less linearly with the forcing amplitude. When forcing is stronger, the upper layer transport reaches a saturation regime, in which transport remains constant for any further increase of wind forcing. The transport of the lower layer becomes increasingly negative, but with much smaller values than the top layer.

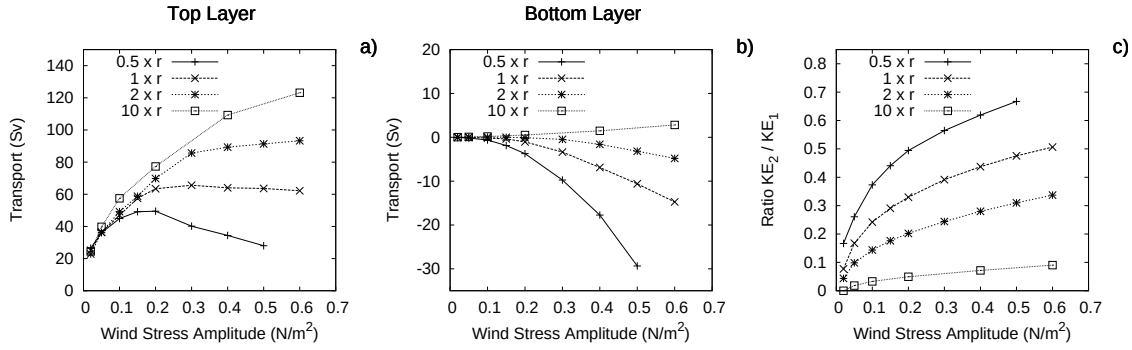

Figure 3–2: Average zonal transport across Drake Passage at equilibrium (a) in the top layer and (b) in the bottom layer for different values of bottom friction: 0.5×r= $5 \cdot 10^{-8}$, 1×r= $1 \cdot 10^{-7}$, 2×r= $2 \cdot 10^{-7}$ and 10×r= 1^{-6} s^{-1}. Also shown is (c) the ratio of kinetic energy in the lower layer to that in the upper layer. All experiments use the reference wind Eq. (3.7), the x axis correspond to different values of τ_0.

When the bottom stress is increased from this reference value, there is no change in the weak wind stress part of the curve. This is consistent with NS09, since in this regime the Sverdrup flux into the channel region is top-trapped at all longitudes. As such, an increase in the bottom drag doesn't alter the vertical structure of the Sverdrup flow. Note from Figure 3–2 a) that the transition between the weak and strong forcing regimes occurs at larger τ_0 for increasing values of the drag coefficient. The nature of the strongly forced regime is also dependent on r. For intermediate values, a saturation is found (transport independent of τ_0), as seen in NS09. By contrast, for weak values, transport decreases with τ_0, and for strong values, transport increases with τ_0 (at least over the range considered). This behavior appears to be related to an influence of bottom drag on a recirculating gyre, as discussed below.

We emphasize that it is the vertical distribution of the flow that determines T_{basin}. A stronger recirculation gyre would be expected to decrease the transport since a smaller fraction of the southward Sverdrup flux would remain top-trapped. Conversely, a weaker gyre would have the opposite effect. Since there is no forcing in the abyssal layer, it follows that the lower layer recirculations are eddy-driven. Then, since increasing bottom friction dampens eddies, one expects large r to be associated with weak recirculation and therefore strong transport in the 'saturation' regime. Figure 3–2 (c) shows the ratio of the average kinetic energy in the bottom layer to that in top layer. As expected, the ratio decreases with increasing r, consistent with the argument above.

The upper panels of Figure 3–3 show the barotropic streamfunction, ψ_B, for two values of bottom stress ($0.5 \times \text{r} = 5 \cdot 10^{-8}$ and $10 \times \text{r} = 1^{-6}$ s^{-1}) at $\tau_0 = 0.4$ N/m^2.

In the interior, and north of Drake Passage, the two are very similar. The bot-

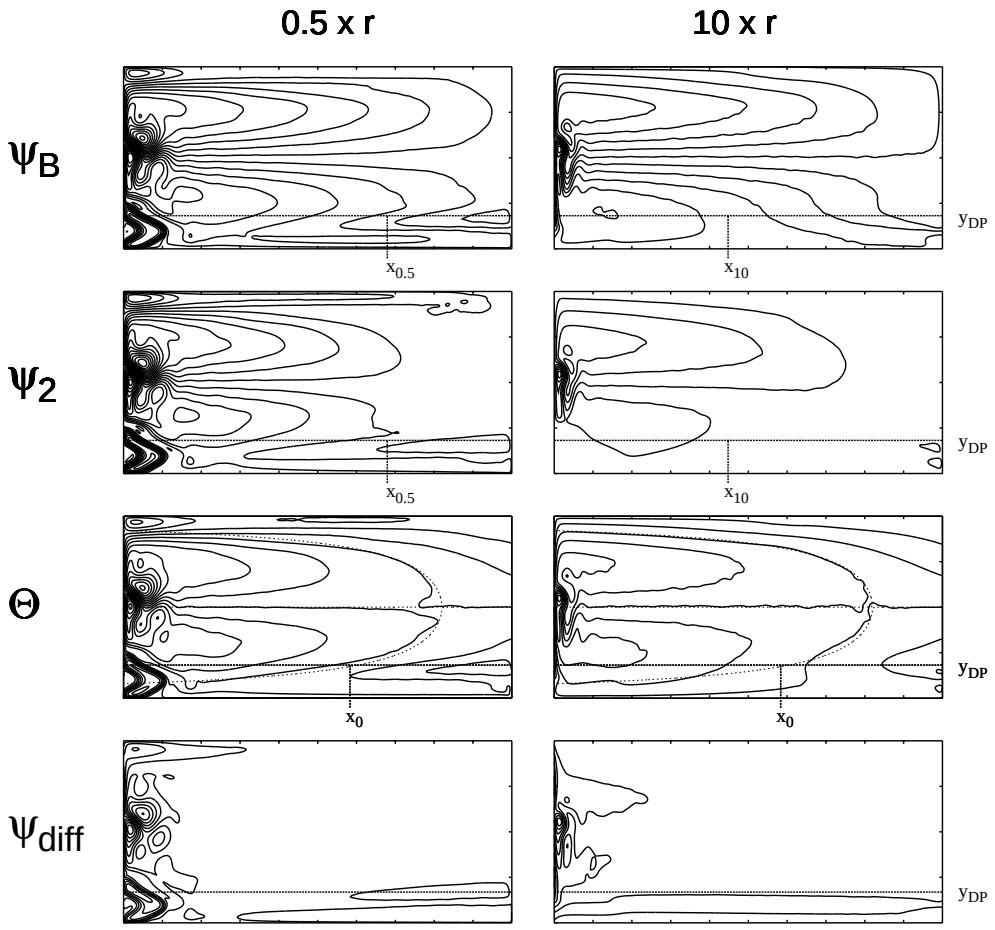

Figure 3–3: Time mean barotropic streamfunction ψ_B, bottom streamfunction ψ_2, characteristics, Θ, and difference between the analytic and modeled barotropic streamfunction, ψ_{diff}, at $\tau_0 = 0.4$ N/m^2 for two different bottom friction values: 0.5×r= $5 \cdot 10^{-8}$ and 10×r= 1^{-6} s^{-1}. Note that the scale of ψ_2 panels is changed slightly compared to that for ψ_B panels to help visualize the circulation. The longitudes, $x_{0.5}$, and x_{10}, mark the division between recirculating and circumpolar streamlines on y_{DP} for the case 0.5×r and 10×r, respectively. The longitude x_0 is the analytic prediction.

tom panels show the difference between the Sverdrup streamfunction and observed barotropic streamfunction, labeled as ψ_{diff}. As predicted by classical wind-driven theory in a basin setting, the interior barotropic flow is in Sverdrup balance in the basin part of the domain. The vertical structure of the Sverdrup flux is different in the two cases. The points $x_{0.5}$ and x_{10} mark the division between recirculating streamlines (to the west) and circumpolar streamlines (to the east). This also coincides with the eastward extent of the abyssal recirculation along the northern edge of the Drake Passage latitude band, $y = y_{\text{DP}}$. In NS09, this position was predicted by the characteristics (or geostrophic contours), which here depend only on the forcing strength. The characteristics, Θ, calculated using the time averaged streamfunction are shown in the third row panels. Since the interior is in near-Sverdrup balance, the seperatrix contour corresponds nicely with its analytic analog. The zonal boundary between recirculating and circumpolar streamlines is to the west of this when r is strong and to the east when r is weak. At intermediate values of r, the seperatrix corresponds well to this boundary. Consistent with this, we observe transport to plateau in a 'saturation regime' for intermediate values of r. For very weak and very strong r; however, this analytic prediction breaks down, and a plateau is not evident in the strongly forced regime. Note, however, that even in these cases, circumpolar streamlines are all connected to the Sverdrup circulation lying to the north.

Momentum Transfer

It is interesting to see if we can extract a signature of the recirculating gyre in the momentum balance. Using brackets $\langle\ \rangle$ to represent zonal and temporal averages, the dominant momentum balance at statistical equilibrium in each layer can be written

as

$$\langle \psi_{1x}\psi_{1yy}\rangle - \frac{f_0^2}{g'H_1}\langle \psi_2\psi_{1x}\rangle - \frac{1}{\rho_0 H_1}\langle \tau\rangle = 0 \tag{3.8}$$

$$\langle \psi_{2x}\psi_{2yy}\rangle - \frac{f_0^2}{g'H_2}\langle \psi_1\psi_{2x}\rangle + \frac{f_0}{H_2}\langle \psi_{2x}h_b\rangle = 0, \tag{3.9}$$

where the first two terms in each equations are the Reynolds stress and interfacial form stress, respectively. The third terms of the equations represent wind forcing and topographic form drag. Figures 3–4a,b show the various terms for our strong (10×r) and weak (0.5×r) bottom drag simulations, plotted as functions of merdional distance across the Drake Passage latitude band. In the strongly damped case, topographic

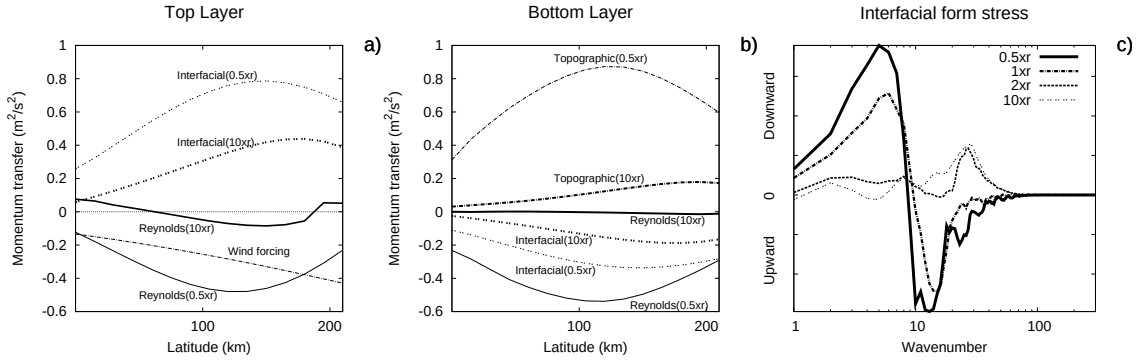

Figure 3–4: Momentum balance as a function of latitude (a) in the top layer, and (b) the bottom layer at $\tau_0 = 0.4$ N/m^2 for two different bottom friction values: $0.5\times$r$= 5\cdot 10^{-8}$ and $10\times$r$= 1^{-6}$ s^{-1}. Also shown is (c) the spectral decomposition of the interfacial form stress term for all the values of bottom friction.

form drag balances the surface wind forcing, and interfacial form stress transmits momentum from the upper to the lower layer. In the weak bottom drag simulation, the Reynolds stress plays a more important important role in both layers, and in fact is larger than the interfacial stress. For all other values of the drag coefficient, the Reynolds stress terms are a factor of two or more smaller than the interfacial drag.

Also, in all of our simulations, the bottom stress term is small compared to other terms in the zonal momentum balance..

Figure 3–4c decomposes terms in the zonal momentum balance according to zonal wavenumber. To do this, we first exress snapshots of the streamfunction in each layer as a Fourier series, $\psi_n = \sum_k A_n(k)\cos(k) + B_n(k)\sin(k)$, for several latitudes in the channel. The interfacial form stress is then calculated as $T(k) = 0.5k(A_1(k)B_2(k) - B_1(k)A_2(k))$. An average of of this over time and latitude is shown in the figure. We plot $kT(k)$ as a function of $\ln(k)$; normalized in this way, the area under the curve is proportional to the stress. For the strong drag case, the interfacial stress is very weak at large spatial scales ($k < 10$) and peaks between wavenumbers 20 and 30. In this case, small scale eddies ($k \sim 25$) accomplish most of the vertical transmission of momentum down to the bottom layer. For lower values of r, $T(k)$ shows a more complex behavior. Near $k = 15$, a peak of upward momentum transfer is evident and seen to strengthen with decreasing r. Additionally, at low k a strong downward momentum flux is seen to develops as r is decreased.

We also calculated $T(k)$ using time averaged streamfunctions. The result is similar to that in Figure 3–4c for k less than 20, but with very little transfer at higher wavenumbers (not shown). The momentum flux at large scales is thus associated with the time averaged flow; whereas, fluxes at small scales are associated with transients. That is, the upperward momentum transfer at around $k \sim 15$ and the downward transfer at low k are associated with the time mean flow, whereas transfers at high wavenumber are associated with transients. The lower layer time mean flow is dominated by a large scale recircluation and a tighter recirculation closely linked

to the topography. We thus infer that the recirculating gyre is responsible for the downward momentum flux at low k and the topographic recirculation is responsible for the upward momentum flux at around $k \sim 15$. This is consistent with both the low k peak and the gyre strengthening as r is decreased. Moreover, refering back to Figure 3–3, a vigorous recirculation over the topography is seen to develop in the lower layer as r is decreased.

To recap, for strong drag, the bulk of the downward momentum flux is accomplished by mesoscale transient eddies, and for weak drag, it is accomplished by a large scale form drag associated with the time mean flow. As r is decreased, two upward momentum fluxes also develop. One is steady, and apparently linked to a topographically-trapped recirculation. The other represents a change of sign in the interfacial stress associated with mesoscale transient eddies.

Variability

The bottom panel of Figure 3–5 shows time series of the transport for different values of bottom drag. As discussed above, zonal transport decreases with r in the saturation regime. Conversely, the variability of the transport is increases strongly with decreasing r in this regime. In particular, a large vascillation of short timescale appears in our $r = 0.5\times$r simulation. To better understand this, we compare the streamfunction averaged over periods where transport is low with that averaged over periods when it is high (specifically, one standard deviation above or below the mean). The averaged ψ_B fields for these periods when transport is maximal and minimal is shown in the upper left panels of Figure 3–5. Negative values correspond to dashed contours. From the figure, it appears that there is a strong basin mode

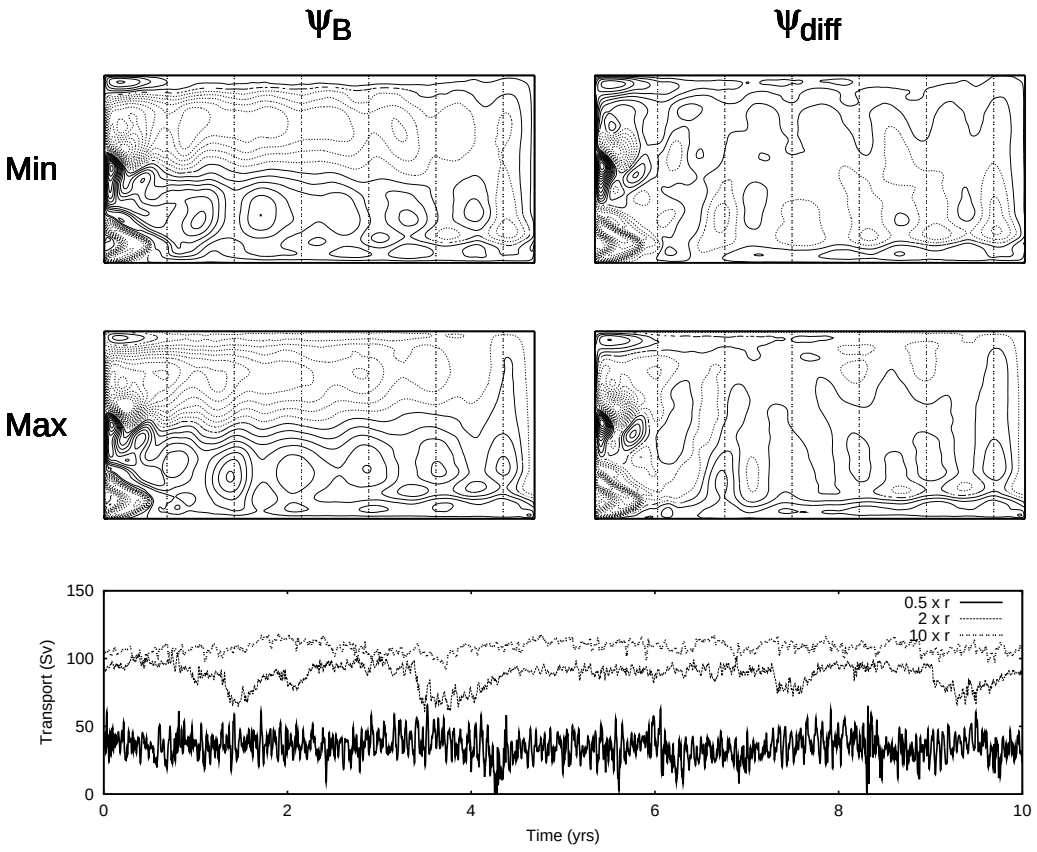

Figure 3–5: Averaged maximal and minimal ψ_B and $\psi_{\rm diff} = \psi_B^{\rm model} - \psi_B^{\rm analytic}$ for $0.5\times$r at $\tau_0 = 0.4$ N/m^2. Solid contours are positive and dashed are negative. Also shown are time series of the upper layer transport for $0.5\times$r, $2\times$r and $10\times$r.

(zonal wavenumber ~ 6) superimposed on the Sverdrup circulation. This is evident in both the maximum and minimum ψ_B fields. Thin dotted lines in the figure show that features in the ψ_B(min) field appear approximately aligned with similar features (having the opposite phase) in the ψ_B(max) field. This is more evident in the right

panels, in which the Sverdrup gyres have been removed. It is clear from the figure that minima in the transport occur when the basin mode is in one phase phase and maxima occur when it is in the other. A movie of this oscillation shows what appears to be large scale barotropic Rossby waves propagating westward and breaking at the western boundary (not shown). Both the strength of this oscillation and of the variability in transport decrease as the bottom drag coefficient is increased. The strength of the recirculating gyre also decreases as r is increased; however, it is not clear whether the oscillation identified above plays any role in the maintaining the gyre.

3.3.2 Effect of a zero-curl wind stress

In a channel setting, transport is widely thought to be controlled mainly by the wind stress, rather than by the wind stress curl. It is not immediately clear that this should also be the case in our geometry, where a basin-like gyre (driven by the curl) lies to the north of the channel region. *Henning and Vallis* [2005] showed that adding a basin portion to the north of a channel slows down the rate at which channel stratification increases with wind stress. This will have a direct effect on the transport, since transport is strongly related to the Rossby radius. In our model, however, stratification is fixed. We are interested to see how transport changes when a constant eastward wind stress is added. We will also be interested in whether or not any changes in transport can be linked to changes in the recirculating gyre identified in the previous section. More specifically, we perturb the reference wind Eq. (3.7) by adding a constant, uniform eastward wind stress. We will see that this does affect the transport. In the weakly forced regime, the channel portion of the transport is

found to be influenced by the zero curl wind. In the strongly forced regime, the zero curl wind affects the position, x_0, seperating that part of the southward Sverdrup flux which feeds the circumpolar flow from that part that feeds a recirculation.

Taking $y = y_C$ to be the center of the Drake Passage latitude band, and referring back to Eq. (3.7), we define a reference value for the eastward wind stress in the channel region as $\tau_1 \doteq \tau_0 \sin^2(\pi y_C/L_y)$. A "zero stress" profile is then given by subtracting $\widehat{i}\tau_1$ from the wind stress profile in Eq. 3.7. In this way, we produce a series of wind stress profiles having identical curl, but different values of stress in the channel:

$$\boldsymbol{\tau} = \widehat{i}\ \tau_0(\sin^2(\pi y/L_y) - \alpha \sin^2(\pi y_C/L_y)). \tag{3.10}$$

Thus, for example, $\alpha = 0$ corresponds to our original forcing profile, and $\alpha = 1$ corresponds to zero stress on $y = y_C$. Note that the stress in the center of the channel is proportional to $\tau_0(1 - \alpha)$. We consider a range of coefficients, α's: 1,0.5,0,-0.5, and -1. The corresponding wind profiles will be referred to as the "zero stress", "0.5×stress", "1×stress", "1.5×stress" and "2×stress" profiles. In all cases, we will take r to be the reference value: $r = 10^{-7}\mathrm{s}^{-1}$. The reference wind stress experiment, "1×stress", is then identical to the 1×r experiment of the previous section. All experiments have been carried out for $L_\rho = 16$ km and $L_\rho = 32$ km.

Transport

Upper layer transport values obtained for this set of experiments is shown in figure 3–6. For both L_ρ, the various curves appear similar, except for an offset related to the addition of the zero-curl wind stress. The general form of a Stommel regime

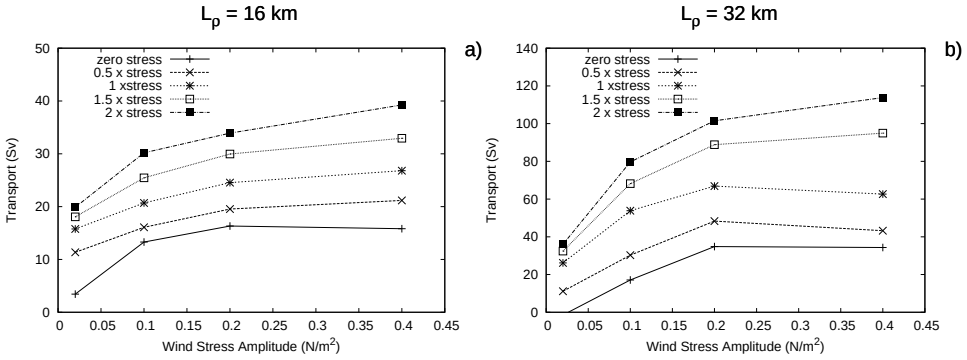

Figure 3–6: Average zonal transport at equilibrium in the top layer at (a) $L_\rho = 16$ km and (b) $L_\rho = 32$ km for a fixed wind stress curl profile with different values of stress in the middle of the channel.

followed by a saturation regime seems roughly respected for both stratifications and irrespective of the channel wind stress. As expected from the analytic model, for lower L_ρ the transition to a saturated regime occurs at a lower value of τ_0. As such, the Stommel regime is shorter (extends over a smaller range of τ_0) in the $L_\rho = 16$ km simulations. Also consistent with the analytic model, the saturation value for the transport is significantly smaller in the $L_\rho = 16$ km simulations. As expected from channel theories, increased stress in the channel corresponds to increased transport (at fixed τ_0). Thus, for a fixed wind stress curl, more stress in the channel translates to more circumpolar transport. Conversely, note that for a fixed value of stress in the channel, more curl seems to imply less transport (e.g., compare $\tau_0 = 0.1$,0.2, and 0.4 on the "2×stress" , "1×stress" and "0.5×stress" curves, respectively.) It thus appears that, while to a large extent, the curl determines how transport depends on the strength of the forcing (i.e., on the value of τ_0 in Equation), the stress in the channel is nonetheless important in setting the transport level.

Figure 3–7 shows sample time averaged barotropic streamfunctions for our 0×stress, 1×stress and 2×stress simulations. Specifically, we show the fields corresponding to $L_\rho = 16$ km and for two values of τ_0. At very small wind amplitude ($\tau_0 = 0.02$

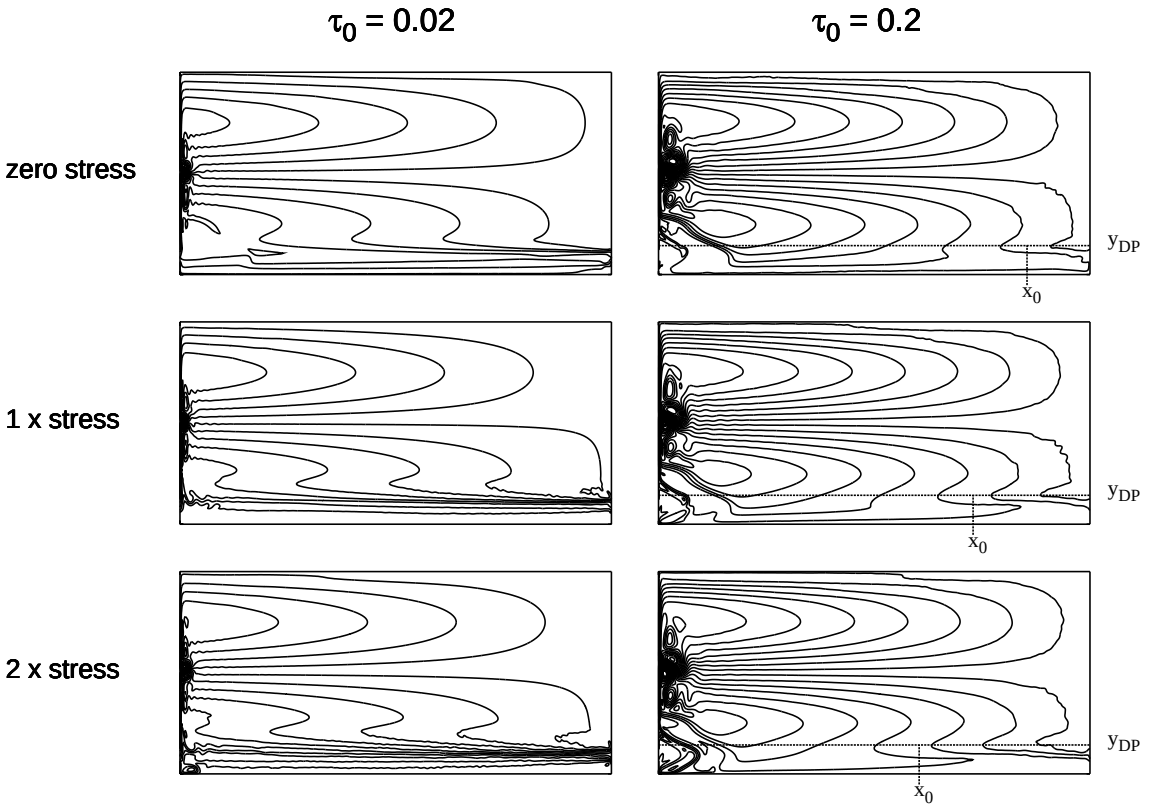

Figure 3–7: Time mean barotropic streamfunction ψ_B using $L_\rho = 32$ km at $\tau_0 = 0.02$ and $\tau_0 = 0.2$ N/m^2 for the zero stress, 1×stress, and 2×stress experiments at $L_\rho = 16$ km. The longitude x_0 marks the division between recirculating and circumpolar streamlines on $y_{\rm DP}$.

N/m2), adding a zero-curl wind stress mainly affects the channel contribution to the transport. In the zero stress experiment, a counter current is observed along southern boundary. In the 1×stress and 2×stress experiments, the channel contribution is

observed to increase with the stress, while the basin contribution is left unaffected. At stronger forcing amplitudes, adding a zero-curl stress affects the strength of the recirculation. This is seen in Figure 3–7 as a displacement of the point, x_0, marking the division between recirculating and circumpolar streamlines. As the stress in the channel is increased, the recirculation shrinks and x_0 moves to the west.

Thus, in a sense, increasing the stress is equivalent to increasing the bottom drag: both lead to a westward displacement of x_0 and to an increase in the transport. There is, however, a difference. Changing r led to changes in the zonal extent of the abyssal recirculation. Here, this recirculation is similar between the three experiments. It extends roughly to position of x_0 in the 1×stress experiment, and is well predicted by the seperatrix characteristic, as in NS09 (not shown). What differs between the three experiments is that, in the zero stress experiment, some of the top-trapped Sverdrup flux entering the channel region recirculates, whereas in the 2×stress experiment, some of the southward Sverdrup flux that is not top-trapped nonetheless feeds the circumpolar transport. Thus, although all of the circumpolar transport in the saturation regime stems from the Sverdrup flux north of the channel, and the vertical structure of this flow is well predicted by the wind stress curl, the assumption that only that portion of the Sverdrup flux which is top-trapped feeds the ACC breaks down.

Momentum Transfer

We next investigate how the addition of a zero-curl wind affects the momentum balance. Figure 3–8 shows a momentum analysis similar to that in Figure 3–4, but for different values of the stress along $y = y_C$. The analysis is performed on our

$\tau_0 = 0.2$ N/m^2 and L_ρ=32 km simulations. Referring to Figure 3–6, this corresponds to the weak-forcing edge of the saturation regime. Results for the zonally averaged

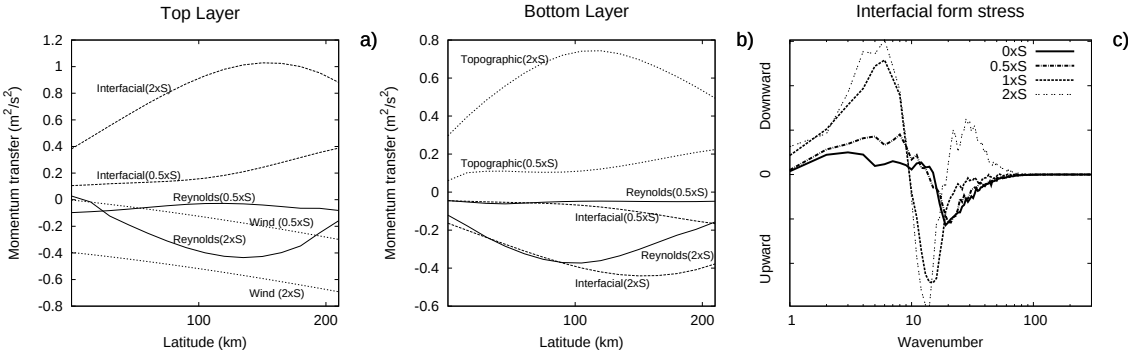

Figure 3–8: Momentum balance as a function of latitude (a) in the top layer, and (b) in the bottom layer at $\tau_0 = 0.2$ N/m^2 for the cases 0.5×stress and 2×stress. Also shown is (c) the spectral decomposition of the interfacial form stress term.

momentum balance in both layers are similar to what was observed in figure 3–4. In all cases, the momentum input at the surface is balanced primarily by the topographic form stress. However, here the Reynolds stress is smaller than the interfacial stress for both cases.

The right panel of Figure 3–8 shows shows a spectral decomposition of the interfacial form stress term. Note that, unlike in Figure 3–4; here, the stress integrated over all wavenumbers differs between the experiments. Nonetheless, several features seem familiar. For example, a peak of upward momentum transfer between wavenumber 10 and 20 develops as the stress is increased. As before, this is associated with the appearance of a circulation over the topography which strengthens as the stress is increased (not shown). A peak of downward momentum flux at large scales and a change in the sign of the small scale momentum transfer (from downward for strong

stress to upwards for weak stress) is also similiar to what was seen in Figure 3–4. Finally, the high k features disappear when time averaged fields are used to do the calculation, i.e., they are associated with transients (not shown). Figure 3–9 shows a decomposition of the interfacial form drag across the channel into standing and transient contributions for our 0.5×stress and 2×stress experiments. As anticipated from Figure 3–8c, the transient eddy momentum flux is upward in the low stress case and downward in the high stress case. Note also that, in the high stress case, transients are more important than time mean features in the overall zonal momentum balance (in the channel).

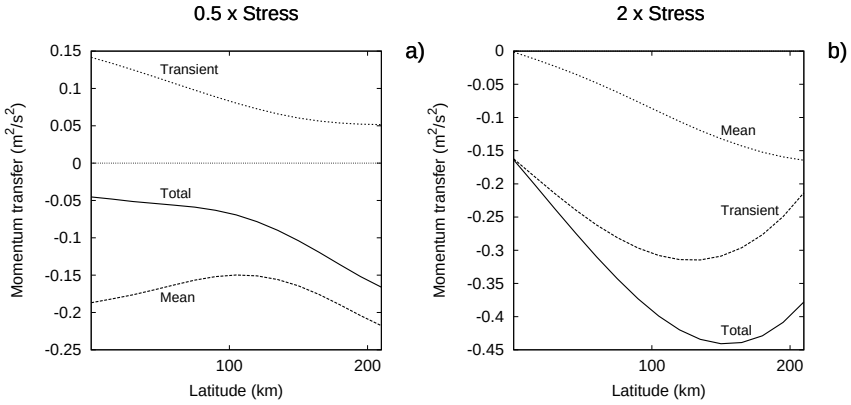

Figure 3–9: Time decomposition of the interfacial form stress term for the cases 0.5×stress and 2×stress.

3.3.3 Effect of wind stress curl

In the previous section, we saw that adding a uniform eastward wind stress while holding the wind stress curl constant led to an increase in transport. In this section, we show that the converse is also true. Specifically, increasing the double-gyre-like forcing while keeping the stress along $y = y_C$ fixed tends to decrease the transport.

This trend was noted in passing in the previous section, but will be considered in more detail here. Also, in the previous section, we chose a fairly narrow channel width (240 km). Since this might tend to lessen the role of channel-like dynamics on determining the transport, a more realistic value (720 km) is considered here. Because the channel is wider, we also changed the precise form of the topography. Specifically, it is wider and elogated so as to extend across the wider gap at the model Drake Passage.

Transport

We begin by comparing simulations forced using our reference wind profile (Equation 3.7) with experiments forced using a uniform eastward wind stress. For a given value of τ_0, the uniform stress corresponds to the stress along $y = y_C$ in the reference profile. Figures 3–10a,b show upper layer transports for these experiments; the Rossby radius were fixed at either $L_\rho = 16$ km or $L_\rho = 32$ km. Experiments forced using the uniform wind stress are labeled 'zero curl'; whereas experiments forced using the reference wind stress profile are labeled 'curl'. For the 'curl' experiments, the 240 km gap results are included for comparison. For both stratifications, transport is significantly higher in the zero curl experiments. As expected, a clear saturation at higher levels of forcing is seen for the reference wind profile. Saturation is less evident in the zero curl experiments. Note that the difference in transport is large. In the saturation regime, experiments forced by the reference wind stress profile have smaller transports by a factor of two or more than experiments for which the wind stress in the channel is comparable, but for which there is no curl. Note also that the saturation seen in the 'curl' experiments appears independent of the

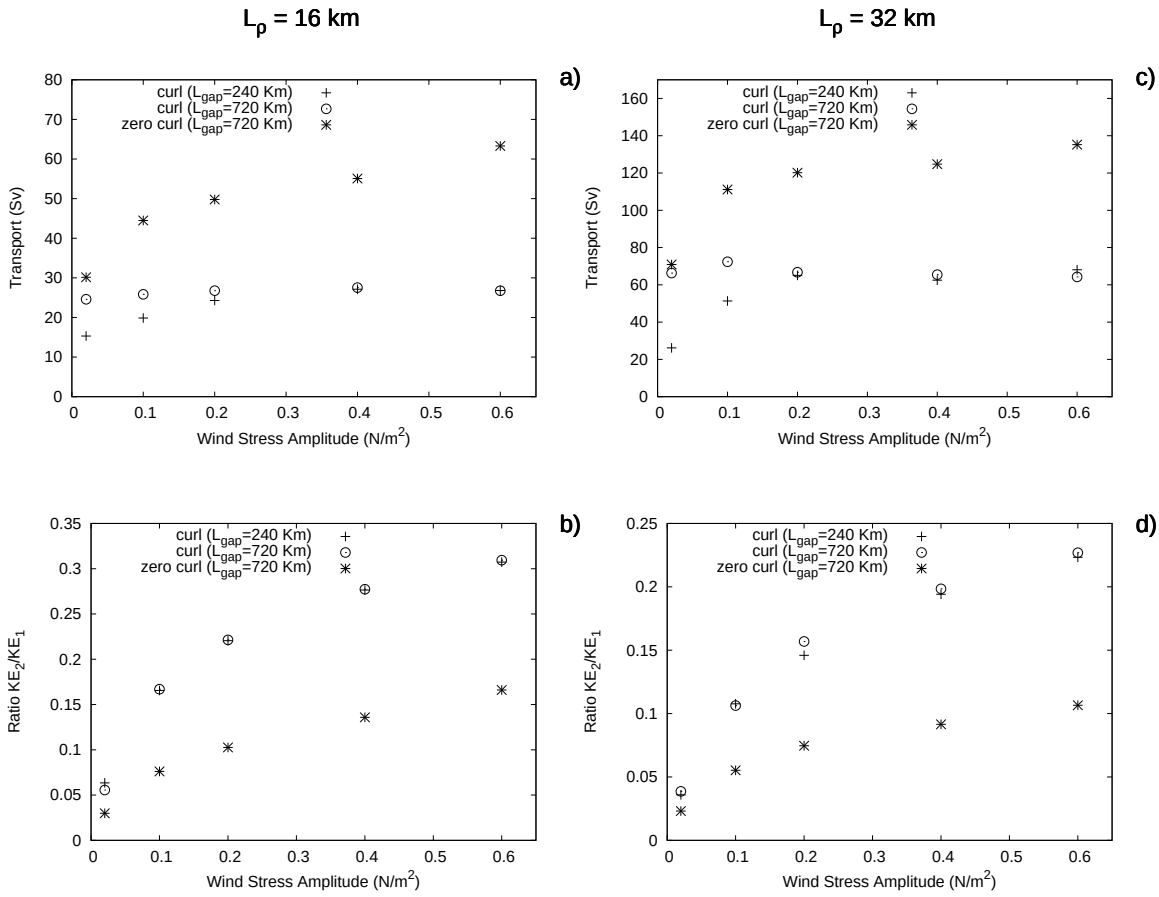

Figure 3–10: Panels (a) and (c) show the average zonal transport in the top layer. Panels (b) and (d) show the ratio of kinetic energy in the lower layer to that in the upper layer . Panels (a) and (b) correspond to $L_\rho = 16$ km, whereas (c) and (d) correspond to $L_\rho = 32$ km.

width of the gap. This is as expected in the analytic model of NS09. Also consistent with this model is that the Stommel regime (clear at low values of the forcing in the 240 km case) is almost absent in the 720 km gap experiments. This is because the basin part of the domain is smaller in latitudinal extent (cf. discussion in NS09).

Figures 3–10c,d show the lower-to-upper layer ratio of the kinetic energy density (i.e., without taking into account the different layer thicknesses) for this series of experiments. The ratio is significantly larger when a wind stress curl is present. It thus appears that the curl serves to increase the amount of eddy activity in the lower layer. Specifically, more eddy activity is seen near the western boundary layer and inside the seperatrix geostrophic contour (not shown). As we will see, this is linked to the appearance of a recirculation gyre that extends into the surface layer. As previously, the recirculating gyre has a strong influence on the circumpolar transport; specifically, it lowers the transport relative to the zero curl simulations.

In the previous section, we compared different simulations having identical wind stress curls, but different levels of wind stress. Here, we compare simulations having identical stresses in (the center of) the channel, but with different amplitudes of the curl. We start with different simulations on the zero curl curves of Figure 3–10. To these, we add a double gyre wind stress curl profile. The amplitude of the double gyre forcing is then varied while keeping constant the stress in the middle of the channel. The experiments are labeled 'stress 0.02', 'stress 0.1', 'stress 0.2', and 'stress 0.4' (cf the horizontal axis in Figure 3–10). Transport values obtained for this set of experiments are shown in Figure 3–11. Except for the very strong stress case, the upper layer transport decreases rapidly as the amplitude of the wind curl profile is increased. Note that there is also westward transport in the lower layer that increases with amplitude and does not depend much on the amplitude of the stress applied in the middle of the channel.

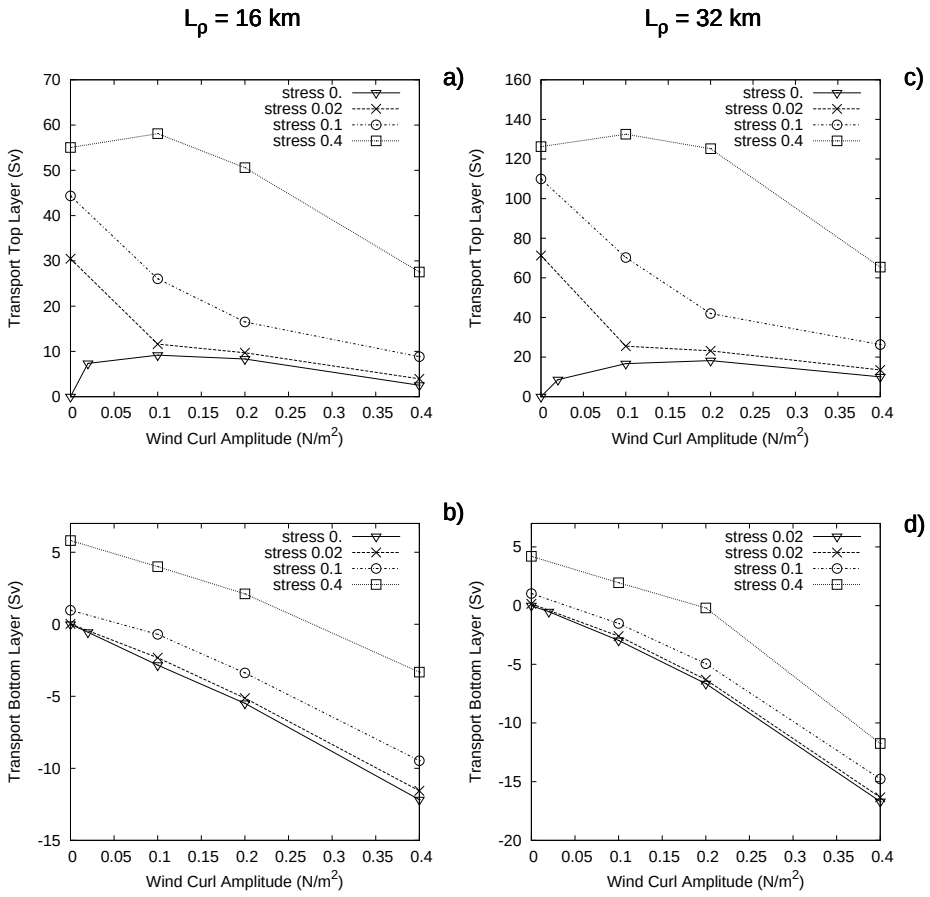

Figure 3–11: Average zonal transport (a and c) in the top layer and (b and d) in the bottom layer for different values of wind stress curl starting from a constant profile.

Upper layer streamfunction and velocity magnitude corresponding to the stress 0.1 experiments (with $L_\rho = 32$km) are shown in Figure 3–12. In the zero curl simulations (upper panels), motion in the basin portion of the domain is very weak. The circumpolar transport is comprised of two zonal jets near the channel latitudes and a strong southern boundary current. The southern boundary current is particularly strong in the western half of the domain (i.e., immediately east of the gap), where it

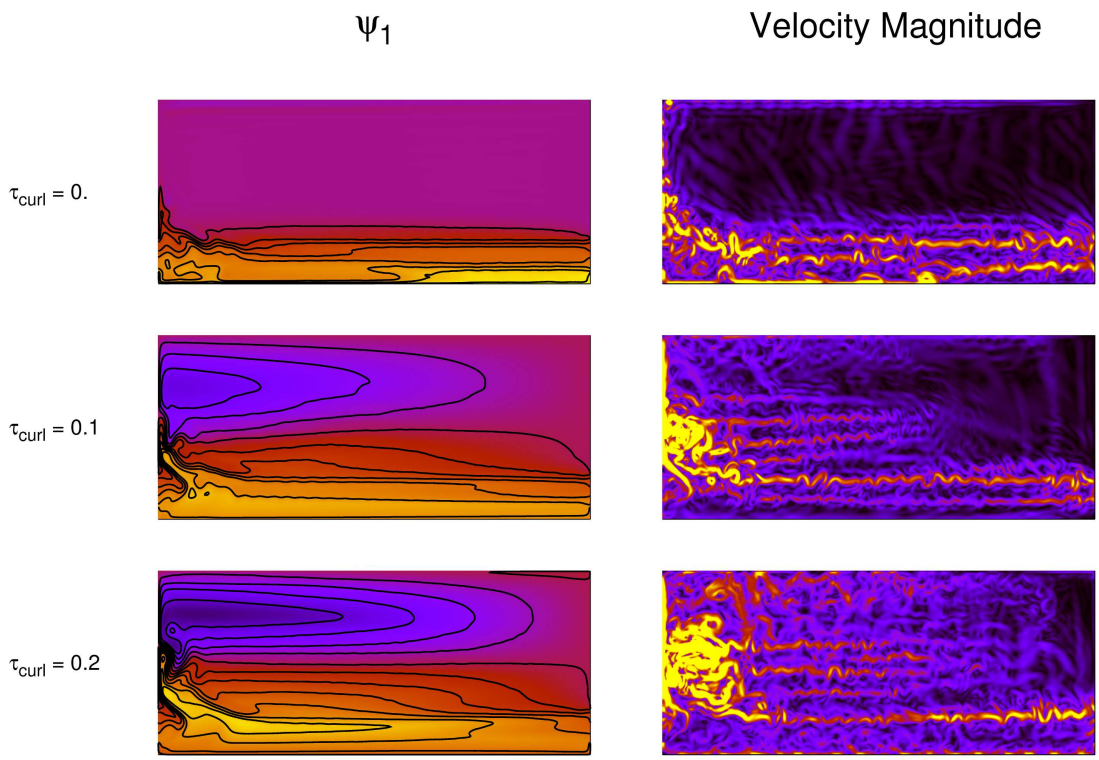

Figure 3–12: Upper layer streamfunction and velocity magnitude for the stress 0.1 experiment with three values of wind stress curl: $\tau_{\rm curl} = 0$, $\tau_{\rm curl} = 0.1$ and $\tau_{\rm curl} = 0.2$. On the velocity plots, every value higher than 0.5 m/s is yellow.

corresponds to almost 40% of the total upper layer transport. This boundary current becomes smaller as the wind stress curl is progressively added and changes direction at $\tau_{\rm curl} = 0.2$.

As anticipated, north of the gap a Sverdrup circulation appears and increases in strength with the curl. With it, a recirculating gyre also appears. For lower values of τ_{curl}, the recirculation is seen only in the lower layer. For higher values, this recirculation deforms the interface sufficiently that it is felt by the upper layer.

For example, it is clearly visible in the lower left panel of Figure 3–12. The right hand panels show instantaneous velocity magnitudes. Zonal jets become increasingly predominant in the basin region as the curl of the wind is increased. Associated with the jets is increased eddy activity (not shown). We speculate that these eddies are instrumental in setting up the recirculating gyres. Apparently, the upper layer recirculation serves to entrain streamlines that might otherwise (e.g,. for the weaker curl simulations) have been circumpolar. In any event, there appears to be shift in the dynamical regime of the channel region when curl is added, relative to the zero curl experiments. This is explored further below.

Momentum Transfer

To better understand this dynamical shift, we consider the zonal momentum balance in the channel region for this set of experiments. Figures 3–13a,b show the main terms of the zonal momentum equation (Eqns. 3.8 and 3.9) in the channel region for the 'stress 0.1' experiment and for $\tau_{curl} = 0$ and $\tau_{curl} = 0.4$. The main

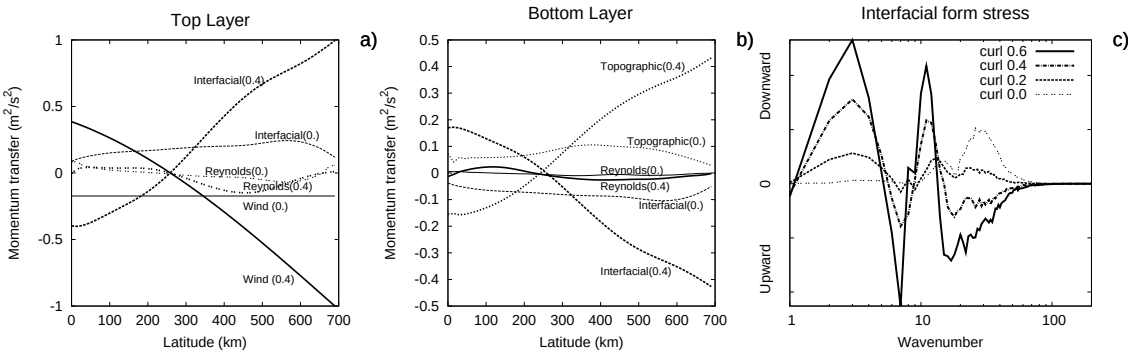

Figure 3–13: Momentum balance as a function of the across-channel distance in (a) the top layer, and (b) the bottom layer for the stress 0.1 experiment. Also shown is (c) a spectral decomposition of the interfacial form stress term.

balance in both experiments is that the wind stress inputs momentum which is transferred downward via an interfacial form stress and removed by the topographic form drag. The Reynolds stress is weaker by comparison, although it makes a non-negligible contribution to the overall balance in the zero curl experiment. Note that the wind stress becomes westward in the southern part of the channel in the $\tau_{curl} = 0.4$ experiment. This can explain the small counter current observed at the southern bounday in this case (not shown).

Panel c shows a spectral decomposition of the interfacial stress for different amplitudes of the wind stress curl. As before, positive values correspond to downward transfers of eastward momentum. The peak of upward momentum at wavenumber seven is associated with a bottom circulation over the ridge. Recall that this was also seen previously, albeit at higher wavenumbers (cf. Figs 3–4 and 3–8). That this phenomenon has moved to smaller wavenumbers here is a consequence of the ridge being wider than was the case in our 240 km gap experiments. As a result of this shift to larger wavenumbers, this peak of upward momentum now cuts in half the low wavenumber peak of downward momentum that we had attributed to the recirculating gyre (roughly, wavenumbers 1-15). As the curl goes to zero, this low wavenumber structure vanishes and the interfacial drag is accomplished solely by a downward momentum flux associated with small scale eddies. Also as found previously, the sign of the stress associated with the mesoscale eddies changes between the zero or low curl experiments and the simulations with stronger curls. That is, transients transfer momentum upward in the regime where the curl dominates.

A time decompostion of the interfacial form stresses in Figure 3–13c is shown in Figure 3–14. In the zero curl case, most of the downward momentum transfer

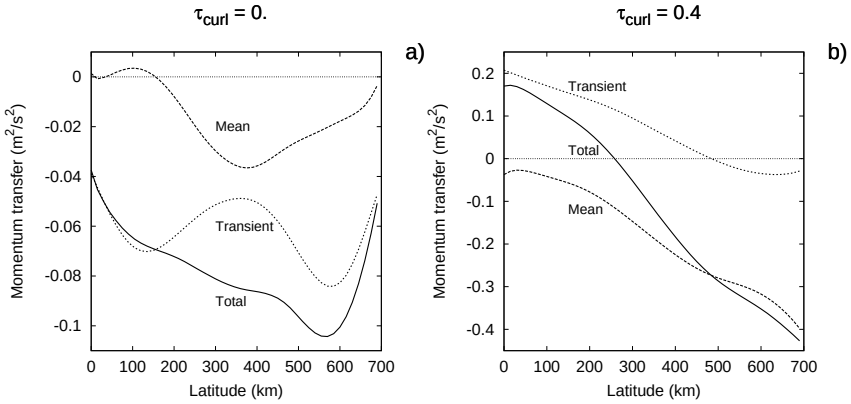

Figure 3–14: Time decomposition of the interfacial form stress term for the cases $\tau_{curl} = 0.$ and $\tau_{curl} = 0.4$

between layers is accomplished by transient eddies, with standing eddies playing a secondary role. When the wind curl is strong, however, standing eddies account for most of the downward momentum transfer. This has previously been observed by *Treguier and McWilliams* [1990]. They considered a zonally reconnecting channel with large scale topography and found the downward momentum flux by the standing eddies to be partially offset by an upper momentum transfer by the transient eddies. In our problem, the standing eddies appear to be associated with a recirculating gyre an a topography driven reciculation.

3.4 Discussion

In this paper, the influence of a basin region to a channel flow has been studied using an idealized model and geometry. This idealized setting allowed us to perform a large number of eddy permitting simulations. Our main focus was on the strongly

forced, or 'satuation' regime. In this regime, we found that, except for forcing profiles with zero or small curls, essentially all of the upper layer circumpolar flow was fed by a southward Sverdrup flux into Drake Passage latitudes. A fraction of this same Sverdrup flux also fed into a recirculation gyre lying above an eddy-driven gyre in the lower layer. What fraction fed the ACC and what fraction fed the gyre was found to depend strongly on both the bottom drag coefficient and on the addition of a uniform eastward wind stress to our reference forcing profile.

That zonal transport increases with bottom friction is counter-intuitive in that the opposite is true in the absence of topography. That this should be the case was well explained, however, in the framework of the analytic model proposed by NS09. More correctly, the dependence of transport on r was explained in that one of the assumptions made by NS09 does not hold in either the high or low bottom drag limit. For low drag, the abyssal recirculation extends significantly beyond the seperatrix geostrophic contour; whereas, for high drag, the opposite is true. Because of this, the fraction of the southward Sverdrup flux into the Drake Passage latitude band that was top-trapped did not correspond to the analytic prediction. Note also, that for high or low values of r, a 'saturation' was not observed in the strongly forced regime.

That zonal transport should increase with the application of an increased eastward wind stress is not counter-intuitive; rather it is anticipated by analogy with channel flows. It is perhaps counter-intuitive that, in the saturation regime, this added transport is linked to a change in the fraction of the Sverdrup flux that feeds the circumpolar flow (e.g., rather than to the addition of a 'channel portion' to the

total transport — i.e., a portion that is not linked to the basin-like flow to the north of the channel. Like with r, the dependancy of transport on the magnitude of the stress in the channel appears related to the recirculation gyre. Stronger winds implied a stronger eddy field, and hence a stronger abyssal recirculation. Associated with this is a deformation of the interface height field (i.e., the thermocline) which deformed potential vorticity contours so as to create an upper layer recirculation gyre. A stronger recirculation in the upper layer meant that a smaller fraction of the upper layer Sverdrup flux fed into the circumpolar transport. Note that, unlike in the simple model proposed by NS09, the division between recirculating and circumpolar streamlines did not correspond precisely to the division between top-trapped Sverdrup flux and Sverdrup flux which extended into the abyssal layer. Instead, for very weak stress in the channel, some of the top-trapped Sverdrup flux fed the recirculation gyre, and for strong stress, some of the southward Sverdrup flux which was not top-trapped nonetheless fed the circumpolar flow.

We also found that, although the transport is sensitive to the magnitude of the stress in the channel, it is also in part determined by the curl. Specifically, adding a wind stress curl (designed to only minimally affects the average stress at channel latitudes) to a uniform wind stress forcing profile tends to reduce the transport. Addition of a curl — in the form of a double gyre forcing — tended to increase eddy activity and the development of an abyssal recirculation in the lower layer. As above, the strength of this gyre appeared to control the partitioning of the Sverdrup flux into Drake Passage latitudes between circumpolar and recirculating flow.

The strength of the abyssal recirculating gyre was found i) to decrease with increasing bottom drag, ii) to be relatively insensitive to the stress in the channel, and iii) to increase with increasing curl. The level of stress in the channel did, however, affect the upper layer expression of the recircuation, with more stress implying less upper layer recircualation (and hence more transport). We also found that where the upper layer recirculation was more prevalent (e.g., either weak bottom drag, weak stress or strong curl), the bulk of the downward transfer of eastward momentum was accomplished mainly by an interfacial form drag associated with the large scale, time mean flow. In these regimes, mesoscale transients effected an upward momentum transfer. An additional upward momentum transfer, linked to stationary flow features over the topography was also found in these limits. In the limit(s) where the upper layer recirculation was weak (strong drag, strong stress, or weak curl), standing eddies contributed little to the interfacial form drag and mesoscale transients transferred eastward momentum downwards. Note, however, that in some cases (e.g., strong stress), Reynolds stresses also played an important role in the zonal momentum balance.

Retrospectively, we can draw a picture of the role of transient eddies in this system. In the first section, we saw that going from strong to weak bottom friction, small scale transient eddies went from a downward to an upward momentum flux. Associated with this was the appearance of the large scale recirculating gyre. This suggests that small scale transient eddies are needed to transmit momentum downward when no other mechanism is available. However, when the downward transmitting recirculating gyre becomes dominant in the momentum balance, small

scale eddies play a totally different role and transmit momentum upwards (note also, however, that the recirculating gyre is itself an eddy-driven phenomenon). This is also confirmed by the experiments of the preceding section. Starting from a constant wind stress and progressively increasing the wind stress curl allows for the development of a recirculating gyre and reverses the momentum flux of small scale eddies. Conversely, this can be changed when both wind stress and wind stress curl are strong. In Figure 3–8 c), we saw that going from zero stress in the channel to high wind stress in the channel without affecting the strength of the wind curl did cause a similar inversion of the small scale momentum flux which end up having a downward contribution at strong channel stress. We also saw in Figure 3–7 that this was associated with a reduction of the large scale recirculating gyre. This implies that the stress in the channel can eventually overcome the effect of the recirculating gyre if it is sufficiently strong. This reinforces the idea that small transient eddies do transmit momentum upward when the momentum balance in the channel is dominated by the large scale recirculation and transmit momentum downward when it is not.

CHAPTER 4

Stratification, topography and wind forcing effects on a idealized Antarctic Circumpolar Current

This chapter introduces the continuous stratification analytic model. It also presents a robustness analysis of this analytic model as well as further experiments to investigate the influence of Sverdrup circulation on the circumpolar transport. It is based on a paper in preparation.

4.1 Introduction

The second chapter of this thesis presents an analytic model of the circumpolar current based on the Sverdrup circulation in a simple 2-layer context. This analytic model was shown to be useful in describing many features of our idealized numerical model of the ACC. Its prediction of the zonal transport fits well the results of our numerical experiments in Chapters 2 and 3, except in cases where the wind stress is strong compared to the wind stress curl. It can be argued, however, that this special case goes beyond the parameter range of relevance to the ACC, since the zonally average wind stress blowing in the Southern Ocean is close to a $\sin^2(y)$ profile. In this final Chapter, we want to further investigate the influence of Sverdrup circulation on the circumpolar flow. Three main questions are asked: i) Can a generalized version of the 2-layer analytic model can be useful in describing the continuously stratified case? ii) How will use of a more realistic topography affect the transport? iii) Can the effect of the wind stress curl and Sverdrup circulation be important even when no meridional walls are present?

In the following, we first generalize our 2-layer analytic model to account for continuous stratification in Section 2. Following *Young and Rhines* [1982], potential vorticity (PV) is assumed homogeneous inside a large 'bowl' whose shape and extent is determined by the large scale limiting equations. We then discuss the vertical structure of wind driven gyres in light of this assumption. In parameter regimes appropriate to the Southern Ocean (e.g., small L_ρ, a large zonal extent and upper-intensified stratification), the depth of no motion predicted by *Young and Rhines* [1982] lies far below the ocean floor. As such, the theory formally breaks down;

however, motion at depths below typical heights of ocean ridges is extremely weak. In other words, although the depth of no motion is rather large, the gyres remain top-trapped in the sense that the vast majority of the flow is in the upper ocean. We then use this observation to extend the 2-layer analytic model of Chapter 2 to the case of a continuous stratification. An analog to the saturation transport level, T_{sat}, is found for the continuously stratified case to be dependent not only on L_ρ but also on whether the stratification is surface intensified or not.

Section 4 then presents three sets of numerical experiments designed to address our main questions. After briefly describing the numerical model in Section 4.1, we present results of varying the vertical resolution to test the validity of the continuously stratified analytic model in Section 4.2. We will see that while most of the assumptions made in the analytic model hold in the numerical experiments, a strong inertial recirculation over the topography, not accounted for in the analytic model, provides additional blocking in the Drake Passage area. Section 4.3 then shows results of using realistic basin dimensions and topography. This will demonstrate how using a topography that is distributed more uniformly over the path of the ACC greatly reduces the blocking effect of the topographic-driven recirculation metioned above. Finally, Chapter 4 ends by presenting the results of 2-layer experiments in a zonally reconnecting channel with a meridional ridge. We will see that even in this context, Sverdrup circulation applies over much of the domain, and plays a major role in the dynamics of the circumpolar flow.

4.2 Continuously stratified analytic model

Before developing the analytic model, we first review how PV homogenization helps to set the baroclinic structure of the circulation in the context of a closed gyre. We then revisit the analytic model of Chapter 2, using PV homogenization ideas to adapt it for contiuous stratification.

4.2.1 Continuously stratified gyres

Following *Young and Rhines* [1982], we consider wind-driven quasigeostrophic flow in a closed box ocean and assume i) the depth-integrated flow is given by the Sverdrup relation, ii) the large scale potential vorticity is homogeneous where the fluid is in motion and iii) the fluid is at rest where potential vorticity contours are blocked (i.e., where they extend back to the eastern boundary). This allows us to determine a depth of no motion, $z = -D(x, y)$ defining a "bowl" below which there is no circulation. The goal now is to determine D.

Large scale potential vorticity homogenization gives

$$q = \left(\frac{f_0^2}{N^2} \psi_z \right)_z + \beta y = \beta y_0 \qquad (0 > z > -D(x, y)) \tag{4.1}$$

where $\beta y_0(z)$ corresponds to the value of q at a given horizontal level. For simplicity, we consider the classic double gyre problem in a closed rectangular basin with dimensions $x \in [0, L_x]$ and $y \in [0, L_y]$, for which symmetry arguments imply $y_0(z) = L_y/2$.

We take the stratification to be exponential,

$$N = N_0 e^{\alpha z/2}. \tag{4.2}$$

This allows for a reasonably realistic representation the observed density profile, while remaining simple enough that analytic integration is tractable. The solution then follows from (4.1) and the Sverdrup relation for the barotropic streamfunction, ψ_B. Assuming the wind stress to be a function of y alone, ψ_B is given by

$$\psi_B(x,y) = (L_x - x)\ \frac{\widehat{k}\cdot\nabla\times\boldsymbol{\tau}}{\rho_0 H} \tag{4.3}$$

where the expression applies far from the western boundary region. Integrating (4.1) twice from $-D$ to z gives

$$\psi(x,y,z) = \lambda\left[\frac{1}{\alpha^2}\left((\alpha(z+D)-1)e^{\alpha z} + e^{-\alpha D}\right)\right], \tag{4.4}$$

where $\lambda(y) = \frac{\beta N_0^2}{f_0^2}\left(\frac{L_y}{2} - y\right)$. Further integrating (4.4) over the total water column gives an expression for the barotropic streamfunction

$$\psi_B(x,y) = \frac{\lambda}{\alpha^3}\left[\left((\alpha D+2)e^{-\alpha D} + (\alpha D - 2)\right)\right]. \tag{4.5}$$

The shape of the bowl, $D(x,y)$, then follows from combining (4.5) with (4.3). In the next section, we will be particularly interested in the structure of ψ at the northern latitude of Drake Passage, $y = y_{\mathrm{DP}}$, i.e. the southernmost latitude where one might expect Sverdrup dynamics to apply. We thus restrict discussion to the structure of the bowl intersecting the x–z plane at $y = y_{\mathrm{DP}}$.

Figure 4–1 shows the dependence of the shape of the bowl at y_{DP} on the decay scale $1/\alpha$ for two values of the Rossby radius. For a large Rossby radius (L_ρ =80 km) the level of no motion deepens as α goes to zero (for which a linear stratification is recovered). However, for a small Rossby radius (L_ρ =10 km), curves of D cross one

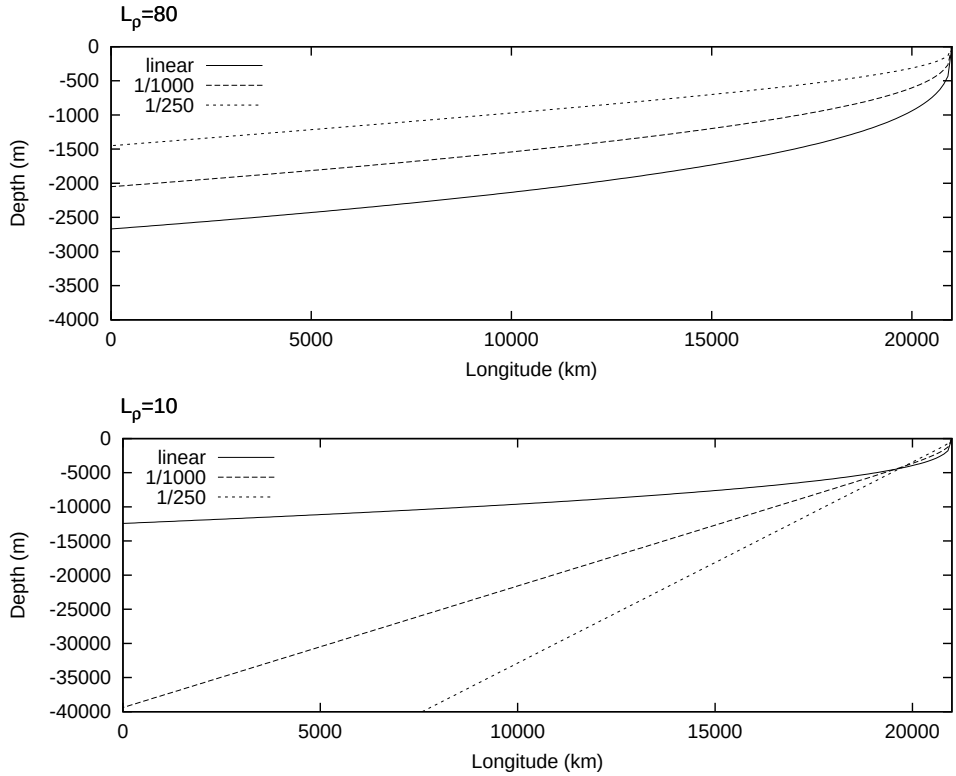

Figure 4–1: Level of no motion D for decay scales $1/\alpha$ =125 m, $1/\alpha$ =1000 m and $1/\alpha = \infty$ (equivalent to a linear stratification) using Rossby radii of 10 km and 80 km. Note that the vertical scale is ten times larger in the L_ρ =10km panel.

another at the eastern side of the basin, and the maximum depth of the circulation, $D_{\max}$, shoals as α goes to zero. Note that this crossing would also occur for L_ρ =80 km if the basin were much larger. Put another way, curves in the L_ρ =10 km case would be similar to those in the upper panel were we to zoom in to the easternmost 500 km or so of the basin — i.e., east of where the curves cross. In the case of a linear stratification ($\alpha = 0$), D goes like $x^{1/3}$, whereas in the exponential case, D becomes essentially linear with x at depths below the decay scale, $1/\alpha$. In this latter case, the slope, $\partial D/\partial x$ is much larger when L_ρ is small, so that if the values of D are

representative of the vertical penetration of the gyres in the $L_\rho = 80$km case, they become absurd for $L_\rho = 10$km. For example, we find $D_{\max} = 62$km on the western side of the basin for $1/\alpha = 250$m and $L_\rho = 10$km.

Formally, of course, the solutions become invalid when D is greater than the basin depth, H. It turns out, however, that even in cases where D lies far below the ocean bottom, the flow at $z = -H$ can be so weak as to be essentially negligible. Consider, for example, the curve $z = \ell_\mu(x)$ above which lies a given fraction, μ, of the circulation on the plane $y = y_{\rm DP}$. This fraction of the flow lying above ℓ_μ is the defined as

$$\int_{\ell_\mu}^{0} \psi(z) dz = \mu \psi_B. \tag{4.6}$$

Using ψ_B from (4.3) and $\psi(z)$ from (4.4) one finds

$$\frac{\lambda}{\alpha^3}\left[(\alpha D - 2) - (\alpha(D - \ell_\mu) - 2)e^{-\alpha \ell_\mu} + \alpha \ell_\mu e^{-\alpha D}\right] = \mu(L_x - x)\frac{\widehat{k} \cdot \nabla \times \boldsymbol{\tau}}{\rho_0 H}. \tag{4.7}$$

The transcendental equation (4.7) can then be solved numerically for ℓ_μ, using D from (4.5).

Figure 4–2 shows $\psi(x, y_{\rm DP}, z)$ calculated assuming an infinitely deep ocean, but plotted only for the upper 4 km. Two cases are considered: a) $L_\rho = 10$km with $1/\alpha = 250$m and b) $L_\rho = 30$km with $1/\alpha = 1000$m, while N_0 is kept constant. The vertical structure of the flow varies considerably from $L_\rho = 10$km to $L_\rho = 30$km. For the latter case, it is spread relatively uniformly inside the bowl, while for $\alpha = 1/250$m, the flow is much more surface intensified. For example, 99% of the southward transport across $y = y_{\rm DP}$ lies above 1147 m whereas $D_{\max}$ is 62 km. Moreover, while the maximum value of the velocity at the surface is $1.6 \cdot 10^{-2}$m/s, the

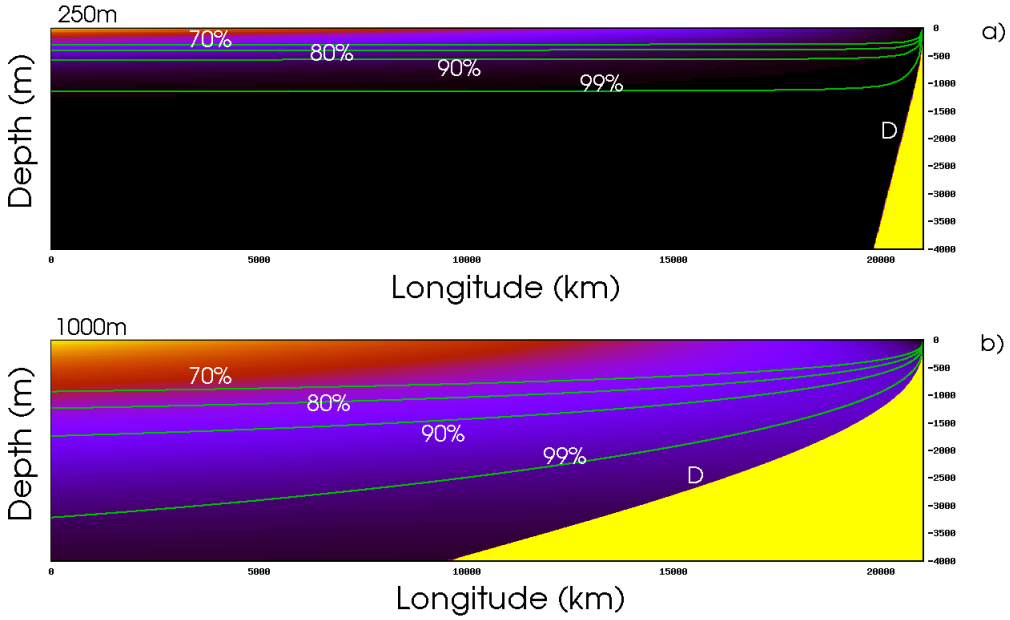

Figure 4–2: Lines $z = \ell_\mu(x)$ on the plane $y = y_{\rm DP}$ superposed on the field of $\psi(z)$ for two decay scales: a) $1/\alpha = 200$m $L_\rho = 10$km and b) $1/\alpha = 1000$m $L_\rho = 30$km. In each cases we choose $\mu = 70\%$, 80%, 90% and 99%.

maximum velocity at 4000 m is only $1.8{\cdot}10^{-9}$m/s so that, in this case, the parameter D is clearly a poor indicator of depth of the gyres. Because of this, we anticipate that the actual solutions (i.e., taking into account the finite ocean depth) will not differ significantly from that shown in Figure 4–2 away from the boundaries.

4.2.2 Analytic model for circumpolar transport

In the two layer model, the Sverdrup flux was divided into one part that resided solely in the upper layer and another that was distributed over both layers. The lower layer geostrophic contours were readily obtainable and determined the zonal position, x_0, separating the top-trapped part (to the east) from the rest of the Sverdrup flux across $y = y_{\rm DP}$. T_{basin} was then the zonal integral of the Sverdrup flux east of x_0.

Simulations showed this to be a reasonable estimate. Even in situations where eddies drove a weak abyssal flow east of x_0, the net basin contribution to the transport was nonetheless well represented by the simple theory when using a reference $\sin^2(y)$ wind profile.

In the continuously stratified case, typical values of D lie below the ocean floor, so that the Sverdrup flux is everywhere distributed throughout the water column. That said, velocities at or below the ridge height can be so small as to be negligible. To adapt the two layer model to the continuously stratified case, we replace "level of no motion" with "level of weak motion" to determine the depth of the circulation. When this level lies everywhere above the topography, the Sverdrup flux into Drake Passage latitudes is considered top-trapped. As such, it is available to feed the circumpolar transport, with only a small fraction of it instead adding to an abyssal recirculation[1] . However, when the level of weak motion descends below the ridge crest, the abyssal recirculation will be stronger, and one cannot rule out the possibility that this recirculation will be felt in the upper part of the water column — i.e., creating a recirculation there as well (cf. Fig. 4–3). In this case, all of the upper ocean portion of the Sverdrup flux across $y_{\rm DP}$ need not add to the ACC.

We thus redefine x_0 as the zonal position east of which the Sverdrup flux can be considered top-trapped. $T_{\rm basin}$ is then the zonally integrated Sverdrup transport

[1] That is, it is assumed that flow below the ridge crest forms a recirculation (i.e., because topography precludes circumpolar flow). When this is weak, isopycnals are not sufficiently deformed so as to also induce a recirculation in the upper part of the water column.

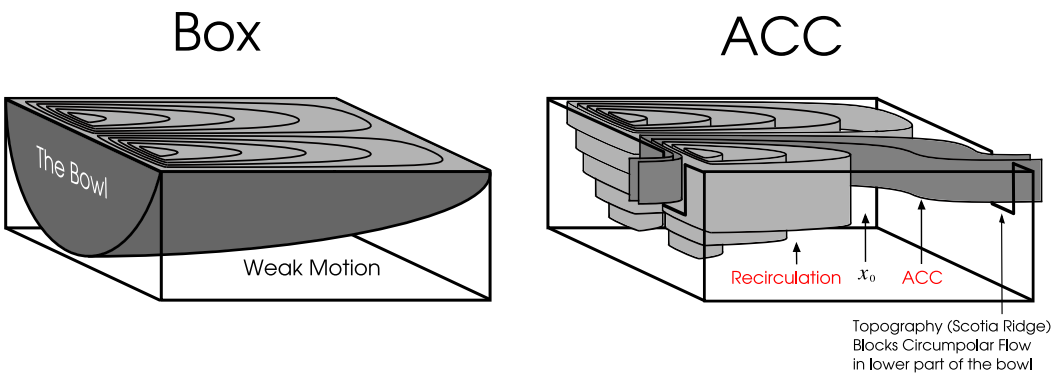

Figure 4–3: Sketch of the baroclinic circulation for the Box and ACC geometry for the continuously stratified case.

across y_{DP} to the east of x_0. For weak forcing, it may be that the Sverdrup flux can be considered top-trapped at all longitudes and in this case, T_{basin} is the zonal integral from a point, x_{west}, just east of the western boundary layer. Note that only a negligible fraction of this would typically lie below the ridge crest. Obviously, the choice of a threshold value below which motion is considered weak is arbitrary, and the continuously stratified model does not have any real predictive value. The goal of this model is rather to examine whether the recirculation phenomenon can be observed in a multi-layered system, and if the same kind of framework presented in the 2-layer case is also applicable in the continuously stratified case.

As shown in the previous section, even when D is quite large, the vast majority of the transport can lie in the upper 1000-2000 m of the water column. Recall (cf. Figure 4–2) that $\ell_\mu(x)$ is defined such that a fraction μ of the Sverdrup across y_{DP} is above $z = \ell_\mu(x)$. We define x_0 as the point at which ℓ_μ drops below the level of

the ridge. We thus estimate T_{basin} as

$$T_{\text{Basin}} \approx \begin{cases} T_{\text{Stommel}} = \psi_B(x_{\text{west}}, y_{\text{DP}}) & : \quad \ell_\mu(\max) < h_{\text{ridge}} \\ T_{\text{sat}} \approx \psi_B(x_0, y_{\text{DP}}) & : \quad \ell_\mu(\max) > h_{\text{ridge}} \end{cases} . \tag{4.8}$$

where x_0 is obtained using $\ell_\mu(x_0) = h_{\text{ridge}}$ in (4.7) and the approximation is that ψ_B includes a (very) small contribution from below the height of the ridge.

If we apply the model to estimate T_{basin}, we obtain the same kind of transport evolution as in the 2-layered system. There is a weak forcing regime where all of the Sverdrup flux across y_{DP} is top-trapped and T_{basin} increases linearly with the forcing amplitude. This is followed by a saturation regime at stronger forcing where T_{basin} becomes independent of the forcing amplitude. In Appendix 1, we show why this is expected using approximate solutions of (4.5) and (4.7). Thus, for a certain choice of level of weak motion, the continuously stratified model is equivalent to the 2-layered model. In the next section, we show that the analytic separatrix derived using the first baroclinic mode predicts well the position, x_0, separating recirculating from circumpolar streamlines in the multi-layered system. The major difference is that eddies are more energetic in the multi-layered system, and a strong inertial recirculation over the topographic ridge adds to the blocking effect of topography.

4.3 Numerical experiments

In this section, we present the results of three sets of experiments. In the first set, we want to verify the validity of the assumptions leading to the continuously stratified analytic model using a multi-layered numerical model with the same idealized basin configuration as Chapter 2 and 3. The second set of experiments aims to test the

robustness of our analytic model using realistic basin dimensions, bottom topography and wind stress profiles. This will highlight the importance of the specific topography chosen along with the crucial role of the wind stress curl in in this system. The third set of experiments is designed to further study this role of the wind stress curl in the context of a zonally reconnecting channel. Even without meridional barriers (but with blocking topography), the wind stress curl sets a Sverdrup circulation and abyssal recirculations cause the transport to saturate at much lower values than the case without wind stress curl.

4.3.1 Numerical model

The numerical experiments are performed using a N-layer quasi-geostrophic model based on the layered quasi-geostrophic potential vorticity equation [*Pedlosky*, 1996]:

$$D_t\left(q_k\right) \;=\; -A_h\nabla^6\psi_k - \delta_{N,k}\; r\nabla^2\psi_k + \delta_{1,k}\;\frac{\widehat{k}\cdot\nabla\times\boldsymbol{\tau}}{\rho_1 H_1}, \qquad\qquad k=1,2,...,N \tag{4.9}$$

where

$$q_k = \nabla^2\psi_k + F_{k,k-1}(\psi_{k-1}-\psi_k) - F_{k,k}(\psi_k-\psi_{k+1}) + \beta y - \delta_{N,k}\frac{f_0^2}{H_n}h_b, \tag{4.10}$$

is the potential vorticity, $D_t() = \frac{\partial}{\partial t}() + \mathrm{J}[\psi,()]$ is the total time derivative, $\psi_0 = \psi_{N+1} = 0$, $F_{1,0} = \frac{f_0^2}{gH_1}$, $F_{k,k-1} = \frac{f_0^2}{g'_{k-1}H_k}$, f_0 is the mean Coriolis parameter, β is the northward spatial derivative of the Coriolis parameter, g is the gravitational acceleration, $g' = g\frac{\Delta\rho}{\rho}$ is the reduced gravity, H_k are layer thicknesses, h_b is bottom topography, A_h is a lateral bi-harmonic viscosity coefficient, r is a bottom drag coefficient and $\boldsymbol{\tau}$ is the wind stress. The numerical implementation is similar to

the 2-layer model presented in Chapter 2 and 3. As the model configuration and parameter values will differ for each set of experiments, they will be discussed at the beginning of each following sections.

4.3.2 Vertical resolution

We begin our investigation by revisiting the 2-layer experiments of Chapter 2 by adding more vertical resolution. One fundamental requirement for the design of these experiments is to avoid circumpolar flow below the level of the topography, which is at the basis of our analytic model. This requirement is very restrictive in the quasigeostrophic context, where topography appears explicitly in the bottom layer equation only.[2] Even in cases where topography is higher than the bottom layer, circumpolar streamlines nevertheless can flow below this topography level . In order to avoid this, we chose to keep a coarser vertical resolution in the lower half of the water column. We thus compare a 2-layer model having equal layer thicknesses of 2000m with a 5-layer model where the upper 2000m is divided in four unequal layers. Model parameters for this set of experiments are shown in Table 4–1. For the 5-layer experiments, the first baroclinic Rossby radius of deformation is equal

[2] In the continuously stratified quasigeostrophic system, the influence of the topography is modeled by applying a boundary condition on the vertical velocity, $w = \frac{f_0}{N^2}\frac{D\psi_z}{Dt} = \frac{f_0}{N^2}\mathrm{J}(\psi, h_b)$, at the bottom. This becomes the last term of (4.10) in the multi-layered system. Note that bottom friction also appears only in the abyssal layer. If one takes the drag coefficient to increase inversely with the bottom layer thickness, then high vertical resolution in the deep ocean implies strong drag and hence weak horizontal velocities. A consequence of this is that $J(\psi, h_b)$ is small, and even large amplitude topography has only a weak effect on the circulation.

Table 4–1: Model parameters for vertical resolution experiments

Parameter		Value
First Rossby deformation radius		$L_\rho = 16$ and 32km
Horizontal resolution		$\Delta x = \Delta y = 15$km
Length of channel		$L_x = 9600$km
Width of channel		$L_y = 3840$km
Width of Drake passage		$L_{\text{gap}} = 240$km
Position of $\nabla \times \tau = 0$		$L_y/2 = 1920$km
Position of Cape Horn		$y_{\text{DP}} = 480$km
Coriolis parameter		$f_0 = -1.3 \cdot 10^{-4}\text{s}^{-1}$
Beta parameter		$\beta = 1.5 \cdot 10^{-11}\text{m}^{-1}\text{s}^{-1}$
Reference density		$\rho_1 = 1035\text{kg/m}^3$
Bottom friction coefficient		$r = 1$ and $10 \times 10^{-7}\text{s}^{-1}$
Bi harmonic dissipation coefficient		$A_h = \beta \cdot \Delta x^5$
	Layer depth	Reduced gravity$[L_\rho = 16, 32\text{km}]$
2-Layers experiments		
Top layer	$H_1 = 2000$m	$g = [9.8\ , 9.8\ ]\text{m/s}^2$
Bottom layer	$H_2 = 2000$m	$g' = [0.0044, 0.0175]\text{m/s}^2$
5-Layers experiments		
Layer 1	$H_1 = 261$m	$g = [9.8\ , 9.8\ ]\text{m/s}^2$
Layer 2	$H_2 = 380$m	$g' = [0.00285, 0.0114]\text{m/s}^2$
Layer 3	$H_3 = 553$m	$g' = [0.00284, 0.0113]\text{m/s}^2$
Layer 4	$H_4 = 805$m	$g' = [0.00237, 0.0095]\text{m/s}^2$
Bottom layer	$H_5 = 2000$m	$g' = [0.00219, 0.0088]\text{m/s}^2$

to the Rossby radius of the equivalent 2-Layer experiment. Two Rossby radii are considered: $L_\rho = 16$ and 32km. For the $L_\rho = 16$ km experiments, baroclinic Rossby radii are 16, 8, 5.7 and 4.4 km whereas for the $L_\rho = 32$ km experiments, they are 32, 17, 11 and 8.9 km. Since the horizontal resolution is 15 km for all experiments, only mode 1 is resolved for the $L_\rho = 16$ experiments whereas mode 1 and 2 are resolved for $L_\rho = 32$. This difference between $L_\rho = 16$ and $L_\rho = 32$ will be crucial for the

circumpolar transport. As we will see in the following, better resolution of the high modes enhances the influence of bottom topography in the upper layers, increasing its blocking effect on the circumpolar flow. The topography is taken to be a 2000m Gaussian ridge, mimicking the Scotia Ridge blocking Drake Passage. The reference wind forcing takes the form of

$$\boldsymbol{\tau} = \widehat{i}\ \tau_0 \sin^2(\pi y/L_y). \tag{4.11}$$

In Chapter 3, we saw how adding a constant wind stress profile or removing wind stress curl can affect the transport evolution significantly. Here we do not consider these effects and only study the wind profile of Equation 4.11, which is a good approximation of the averaged zonal wind stress in the Southern Ocean if $\tau_0 \sim 0.1$ N/m^2.

Figure 4–4 shows results obtained for the transport above topography at $L_\rho =$

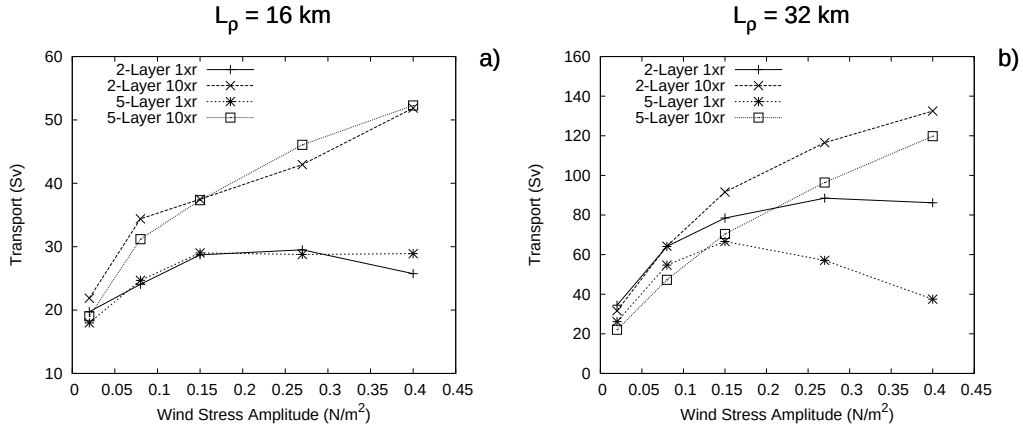

Figure 4–4: Time average transport above topography obtained with 2-layer and 5-layer in a) the $L_\rho = 16$ case and b) the $L_\rho = 32$ case. For each stratification profile, results obtained with two values of bottom friction coefficient are plotted 1×r=1 $\times 10^{-7}$ and 10×r= 10×10^{-7}s^{-1}.

16 and 32km for the 2-layer and 5-layer experiments. Two values of the bottom friction coefficient, $r = 10^{-7}$ and $10^{-6}\mathrm{s}^{-1}$, are considered. The analytic saturation values obtained from the 2-layer model is 26 Sv for $L_\rho = 16$ and 103 Sv for $L_\rho = 32$, which is close to the 2-layer solutions obtained with the reference $10^{-7}\mathrm{s}^{-1}$ bottom friction coefficient in Figures 4–4 a, b. When vertical resolution is added, transport is unaffected at $L_\rho = 16$ whereas significant changes are observed at $L_\rho = 32$. In the following, we first use the $L_\rho = 16$ experiment to examine the validity of the assumptions made to derive the continuously stratified model. We will then examine how a better representation of the high baroclinic modes induces the observed changes in transport at $L_\rho = 32$.

Case L_ρ=16km

In the basin region, the assumptions of the analytic model where: i) the vertically integrated Sverdrup relation applies, ii) the potential vorticity is homogeneous inside the level of weak motion, iii) the fluid is at rest where potential vorticity contours are blocked and iv) abyssal recirculation is expected to be strong enough to be felt in the upper part of the water column when the level of weak motion descends below the ridge crest. Figure 4–5 shows the vertical structure of the time averaged potential vorticity field of the 5-layer case. Note that the scale of the first layer potential vorticity is ten times that of the other layers (which is $\beta L_y/2$). In this first

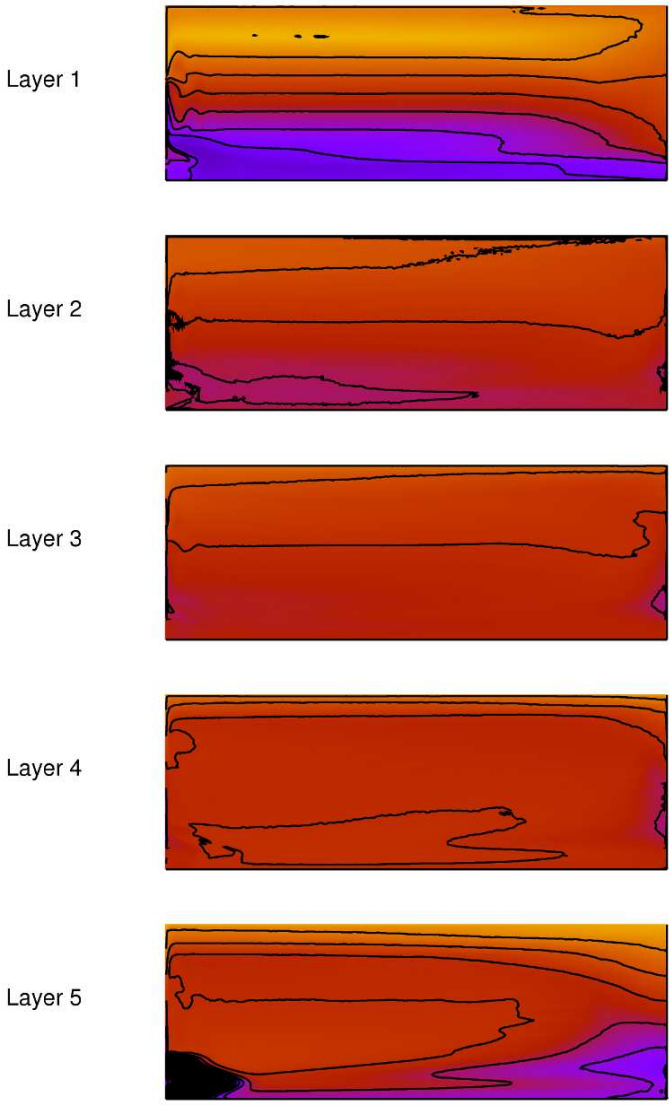

Figure 4–5: Time averaged potential vorticity field at each vertical level for the 5-layer experiment in the $L_\rho = 16$ case at $\tau_0 = 15$ N/m^2. The scale of the upper layer PV panel is ten times higher than the scale of others panels (which is $\beta L_y/2$).

layer, a strong PV gradient is observed due to the direct action of the wind stress[3] . Below the upper layer, in the basin region north of Drake passage, potential vorticity homogenization takes place because of the action of geostrophic eddies. A large bowl of homogeneous potential vorticity can be observed in Figure 4–5 between layers 2 and 5. This homogenization has been discussed by *Marshall et al.* [1993] in a similar quasigeostrophic context.

To investigate the circuation inside this region of homogeneous PV, we show the vertical structure of the streamfunction in Figure 4–6. The baroclinic structure shows close similarities with the sketch of Figure 4–3. North of the channel region and away from the western boundary, vertically averaged solution obeys Sverdrup relation (not shown). The vertical distribution of the Sverdrup flow is divided into two main regions. Where the bottom layer recirculation is strong enough, a recirculation is observed in all the water column (gray shaded region in Figure 4–6). Where the bottom circulation is negligible over y_{DP}, the Sverdrup flux into the channel region is free to go into Drake passage, and indeed this forms most of the circumpolar current. The longitude x_0 marks the division between the recirculating and the circumpolar streamlines. Note also that regions of no motion fit well those of blocked PV contours in Figure 4–5. In sum, all the assumptions leading to the analytic model apply well in this context. One of the main unknowns of the analytic model

[3] An alternative interpretation is that PV is essentially homogeneous in the upper layer, and that the distribution observed here corresponds to a surface temperature field.

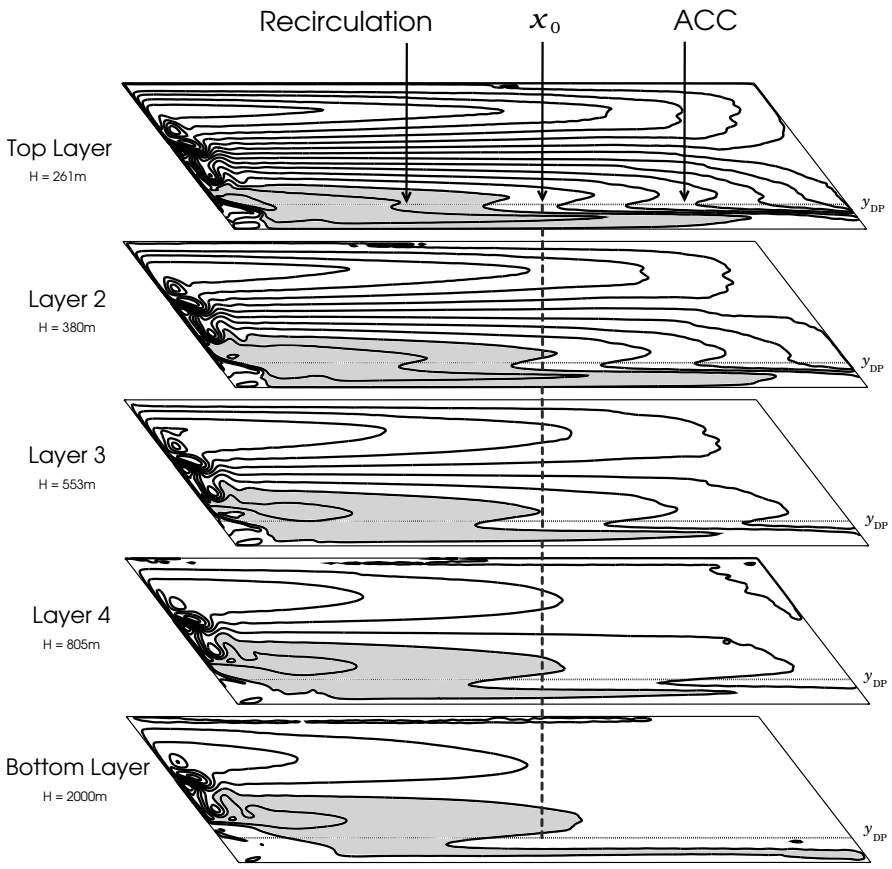

Figure 4–6: Time averaged streamfunction at each vertical level for the 5-layer experiment in the $L_\rho = 16$ case at $\tau_0 = 15$ N/m^2. The the gray shaded area marks the extent of the gyre-like recirculation. The point x_0 on the latitude y_{DP} marks the division between recirculating and circumpolar streamlines.

is the choice of the level of weak motion determining where the Sverdrup flux into Drake Passage can be considered top-trapped. Here, the position, x_0, separating recirculating and circumpolar streamlines does not change when going from 2 to 5 layers (not shown) and, as a consequence, the transport is insensitive to the increase of vertical resolution. This suggests that the level of weak motion is well represented

by the equivalent analytic 2-layer separatrix obtained with the first baroclinic Rossby radius.

Coming back on Figure 4–4, we can see that when the bottom friction is increased, much higher transport values are obtained. This is consistent with what was observed in Chapter 3: a reduction of the bottom layer recirculation shrinks the recirculation in all the water column, and allows for more top trapped streamlines to go into Drake Passage (not shown).

Case L_ρ=32km

In Figure 4–4, we showed how adding more vertical resolution changes the transport significantly for the reference bottom drag at $L_\rho = 32$km. This difference becomes more and more visible as the wind forcing increases. For the 5-Layer case, transport begins to decrease instead of reaching a constant value in the saturation regime (as was the case with 2-layer). In the following, we argue that this phenomenon is due to an increased recirculation over the topography, which enhances its blocking effect. Figure 4–7 shows the time averaged barotropic sreamfunction, ψ_B, the difference between the barotropic and Sverdrup streamfunction, ψ_{diff}, and the bottom layer streamfunction, ψ_{bottom}, for both vertical resolutions at $L_\rho = 32$km, and in the saturation regime. In all 5-layer panels, the western boundary recirculation is more intense than in the 2-layer case. Even if the Sverdrup solution still applies away from the western boundary and north of the channel region, it can be seen that inertial recirculation now occupies a greater portion of the domain in the ψ_{diff} field. This phenomenon is due to the effect of resolving high baroclinic modes [*Barnier et al.*, 1991]. Resolving these higher modes enhances the inertial mode and the penetration

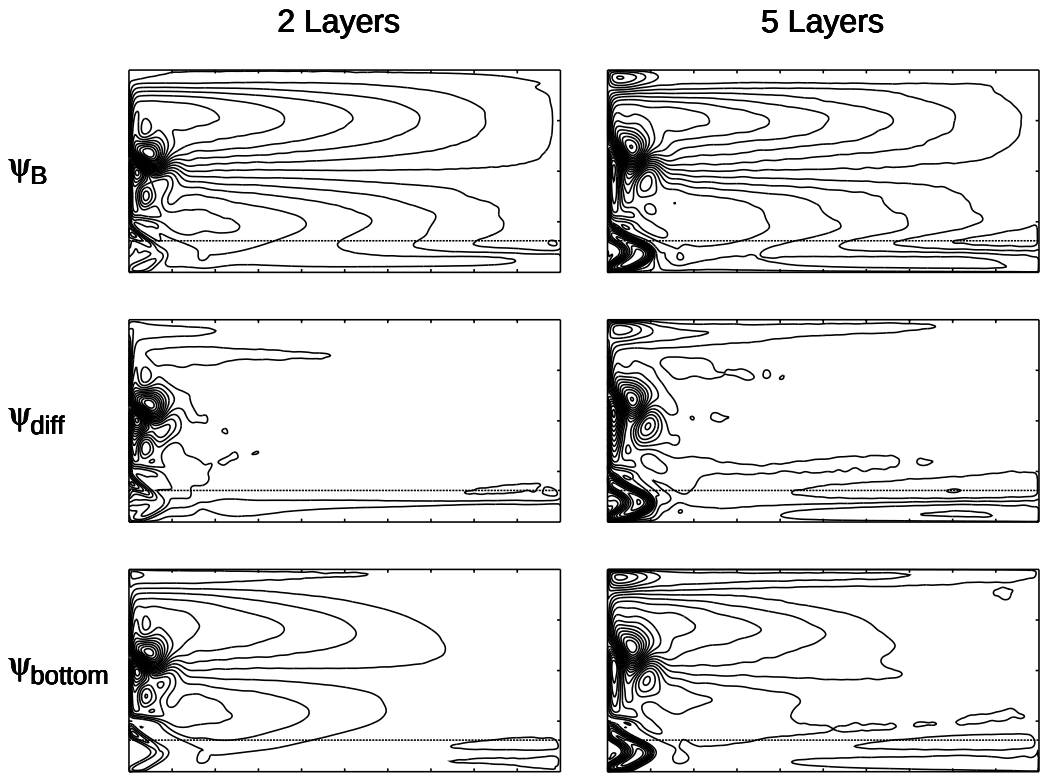

Figure 4–7: Time averaged barotropic sreamfunction, ψ_B, difference between barotropic and Sverdrup streamfunction, ψ_{diff}, and bottom layer streamfunction, ψ_{bottom} for the 2- and 5-layer experiments in the $L_\rho = 32$ case at $\tau_0 = 0.4$ N/m^2.

scale of mid-latitude jet, but leaves the large scale interior modes of circulation unaffected. Here, in the context of an open Drake Passage with topography, not only the western boundary inertial recirculation but also topographically-driven recirculation is more energetic. This can be seen in the southwest corner of the ψ_{bottom} panels of Figure 4–7. Note that the height of the ridge is half the total depth of the ocean conflicts with the quasigeostrophic assumption of the numerical model. It

is thus possible that the topography may be over represented in these experiments. In Chapter 3, we saw that the bottom topography has a strong upward momentum transfer signature in the scale decomposition spectrum of the form drag term. Here, this effect is even more pronounced (not shown) and as a consequence, the topographically driven recirculation is felt by the upper layers — and its signature can clearly be observed in the barotropic streamfunction. This recirculation blocks some of the outflow of Drake Passage, thus creating an additional barrier to the upper layer circumpolar flow and causing a reduction of the number of circumpolar streamlines (see ψ_{diff} panels of Figure 4–7). That this topographically-driven recirculation has an inertial origin also explains why transport is effected mainly in the saturation regime, where the forcing is strong. When bottom friction is increased, this effect vanishes and transport in the saturation regime increases in a similar manner to the 2-Layers case (see Figure 4–4).

In sum, the vertical resolution experiments show that the basic elements put forth in the analytic model can be observed using numerical simulations. However, inertial effects add to this picture, making analytic predictions hard to obtain. In the following section, we argue that the influence of these inertial effects on the zonal transport is less important when the topography is distributed more uniformly along the path of the circumpolar current.

4.3.3 Realistic dimensions and topography

We now investigate the effect of better representing bottom topography in this system. The topography used is a linear unsmoothed interpolation of the ETOPO5 data to a Cartesian grid. Topography data from 33^o-67^o S is interpolated on a

20000 km by 4000 km rectangular domain. To reduce the effects related to violating quasigeostrophic approximation, the topography is truncated at ±800 m from the mean depth of the bottom layer. Following other similar studies [e.g., *Marshall et al.*, 1993; *Hogg and Blundell*, 2006], we choose three unequally spaced layers. Model parameters for this set of experiments are shown in Table 4–2. Three stratification

Table 4–2: Model parameters for realistic dimensions and topography experiments

Parameter	Value	
Horizontal resolution	$\Delta x = \Delta y = 12.5$km	
Length of channel	$L_x = 20000$km	
Width of channel	$L_y = 4000$km	
Width of Drake passage	$L_{\text{gap}} = 600$km	
Position of $\nabla \times \tau = 0$	$L_y/2 = 2000$km	
Position of Cape Horn	$y_{\text{DP}} = 1213$km	
Depth of Layer 1	$H_1 = 300$m	
Depth of Layer 2	$H_2 = 1100$m	
Depth of Layer 3	$H_3 = 2600$m	
L_ρ = 16 km experiments ($\Delta x = 12.5$km)		
Reduced gravity (10^{-2} m/s^2)	$g_1' = 0.5$	$g_2' = 0.45$
Baroclinic Rossby radius (km)	$L_{\rho 1} = 16$	$L_{\rho 2} = 8$
L_ρ = 32 km experiments ($\Delta x = 12.5$km)		
Reduced gravity (10^{-2} m/s^2)	$g_1' = 3$	$g_2' = 1.7$
Baroclinic Rossby radius (km)	$L_{\rho 1} = 32$	$L_{\rho 2} = 19$
L_ρ = 48 km experiments ($\Delta x = 25$km)		
Reduced gravity (10^{-2} m/s^2)	$g_1' = 8.2$	$g_2' = 3.7$
Baroclinic Rossby radius (km)	$L_{\rho 1} = 48$	$L_{\rho 2} = 31$

profiles are considered. They are labeled as $L_\rho = 16$ km, $L_\rho = 32$ km and $L_\rho = 48$ km, in reference to their first baroclinic Rossby radius of deformation. All baroclinic

modes are resolved except for the second mode of the $L_\rho = 16$ km experiment. The reference wind forcing profile is the same as the preceding section Equation. (4.11).

In the following, we will examine the impact of the realistic topography by comparing with a Gaussian ridge similar to the ones used in Chapters 2 and 3. Following this, we will revisit some of the experiments of Chapter 3 to further investigate the role of the wind stress curl in this system.

Comparison between Gaussian ridge and realistic topography

Figures 4–8 a) and c) show zonal transport in the upper two layers obtained for both the realistic and Gaussian ridge topographies. Also shown the are predictions of the analytic two layer model. For realistic topography, the experiments fit well with the analytic prediction, except for $L_\rho = 16$ km, where transport is higher than expected. In this experiment, however, the second baroclinic mode is not resolved. As disscussed earlier, a higher resolution increases the eddy field and may enhance the bottom layer recirculation and lower the transport.

At very low wind stress, transport is unaffected by the change of topography. However, as the wind stress increases, experiments with the Gaussian ridge show much lower values of transport for all stratification profiles. This can be partly explained when looking at the vertical distribution of the kinetic energy. Figures 4–8b,d show the ratio of the time averaged bottom layer kinetic energy to the averaged upper layers kinetic energy. As was the case in Chapter 3, the ratio is a good indicator of the zonal transport strength. For a given wind stress, a low ratio implies strong transport whereas circumpolar flow weakens as the ratio increases.

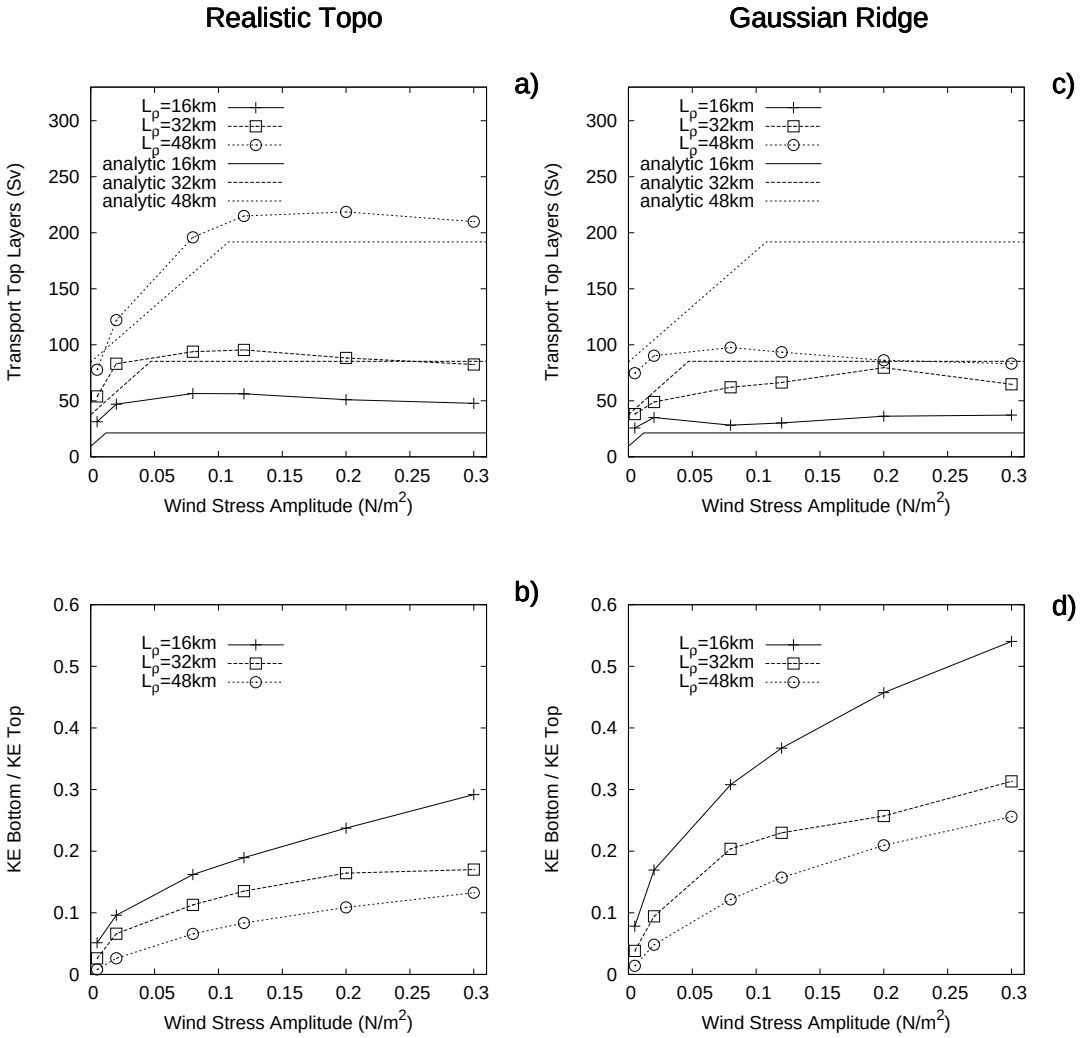

Figure 4–8: Average zonal transport in the upper two layers obtained a) with the realistic topography and c) Gaussian ridge topography for different stratifications profiles. Also shown are the predictions of the 2-layer analytic model of Chapter 2 using the first baroclinic radius of deformation. Panels b) and d) show the ratio of the bottom layer to the upper layers time averaged kinetic energy, $2\mathrm{KE}_3/(\mathrm{KE}_1 + \mathrm{KE}_2)$.

In Chapter 3, we saw that increasing the ratio between bottom and top layer KE implied a more intense bottom layer recirculation, which significantly decreased

the zonal transport. Here the picture seems different. Table 4–3 shows the detailed vertical distribution of the kinetic energy for different wind stress at $L_\rho = 32$ km. For every wind stress, the bottom layer kinetic energy is nearly independent of the

Table 4–3: Vertical distribution of the domain averaged kinetic energy at $L_\rho = 32$ km.

	$\tau_0 = 0.02$ N/m^2		$\tau_0 = 0.12$ N/m^2		$\tau_0 = 0.2$ N/m^2	
	Gaussian	realistic	Gaussian	realistic	Gaussian	realistic
Layer 1	.00720	.01561	.03753	.07849	.06917	.11240
Layer 2	.00088	.00175	.00780	.01057	.01567	.01668
Layer 3	.00038	.00057	.00521	.00602	.01090	.01061

topography. However, major changes occur in the upper layer, where the average kinetic energy has doubled in the case of a realistic topography. This can be seen by looking directly at instantaneous fields of the upper layer velocity magnitude, $\sqrt{u^2 + v^2}$, in Figure 4–9 and 4–10. In both figures, the wind stress amplitude is τ_0=0.08 N/m^2, for which the sinusoidal wind profile (Eq. 4.11) is close to the time and zonally averaged wind stress in the southern ocean. For a Gaussian ridge, most of the interior solution is dominated by coherent zonal jet structures, intensifying in the western portion of the basin (see Figure 4–9). The width, strength and spacing of these jets increases with the Rossby radius. The inertial region is limited to a small area at the western boundary of the domain. For each Rossby radius, zonal jets emanate from this western boundary inertial region. When realistic topography is used, this picture changes drastically, even if the wind stress is relatively small. Secondary inertial regions are appearing, distributed along the path of the circumpolar current where it crosses major topographic obstacles (see Figure 4–10). Zonal jets seem to be locked between these different inertial regions. Moreover, jet structures are not as

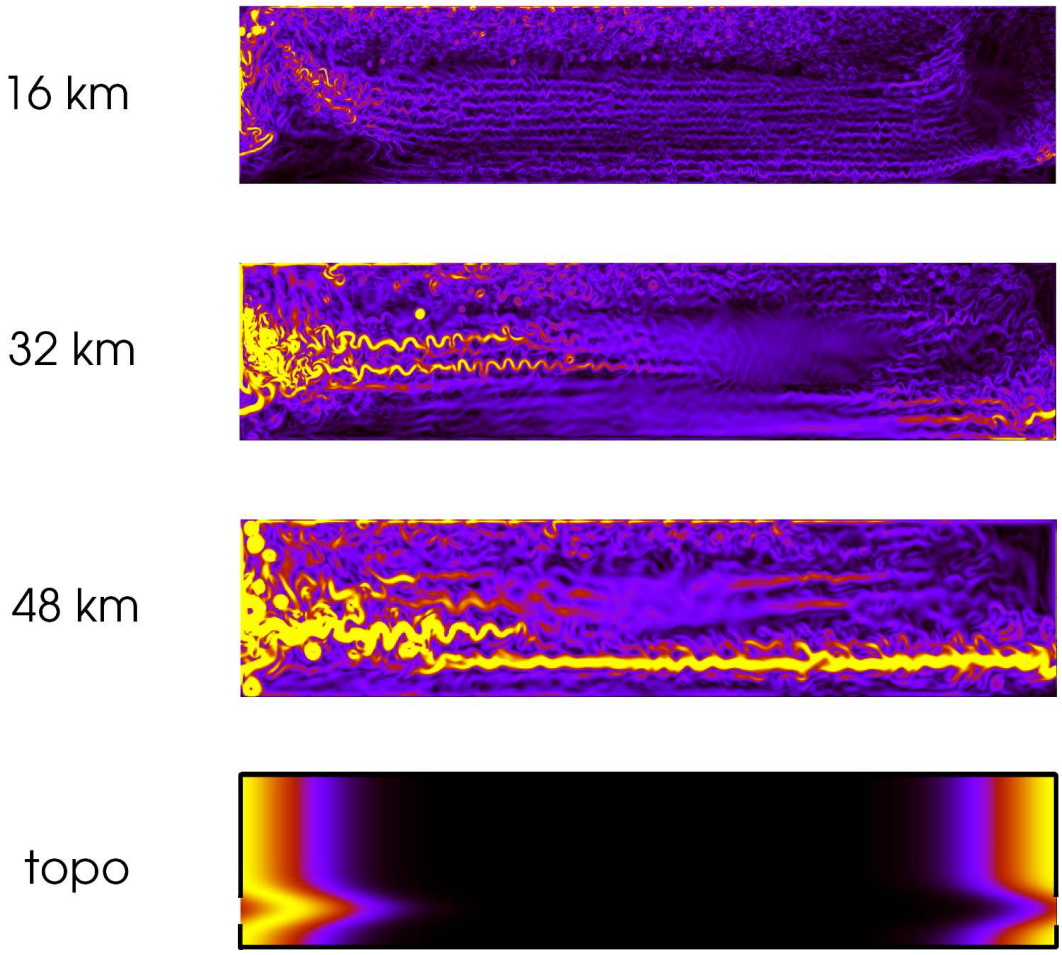

Figure 4–9: Instantaneous upper layer velocity magnitude field, $\sqrt{u^2 + v^2}$, obtained with the Gaussian ridge topography using different stratifications at τ_0=0.08 N/m^2.

zonally coherent as those of Figure 4–9. One of the most striking feature of Figure 4–9 and 4–10 is the global enhancement of the upper layer eddy field for all Rossby radii when realistic topography is used.

To further investigate the role of topography in the energetics of this system, we now look at the spatial distribution of the bottom layer kinetic energy. Figures 4–11a,b,c,d show the mean and eddy kinetic energy obtained with both topography

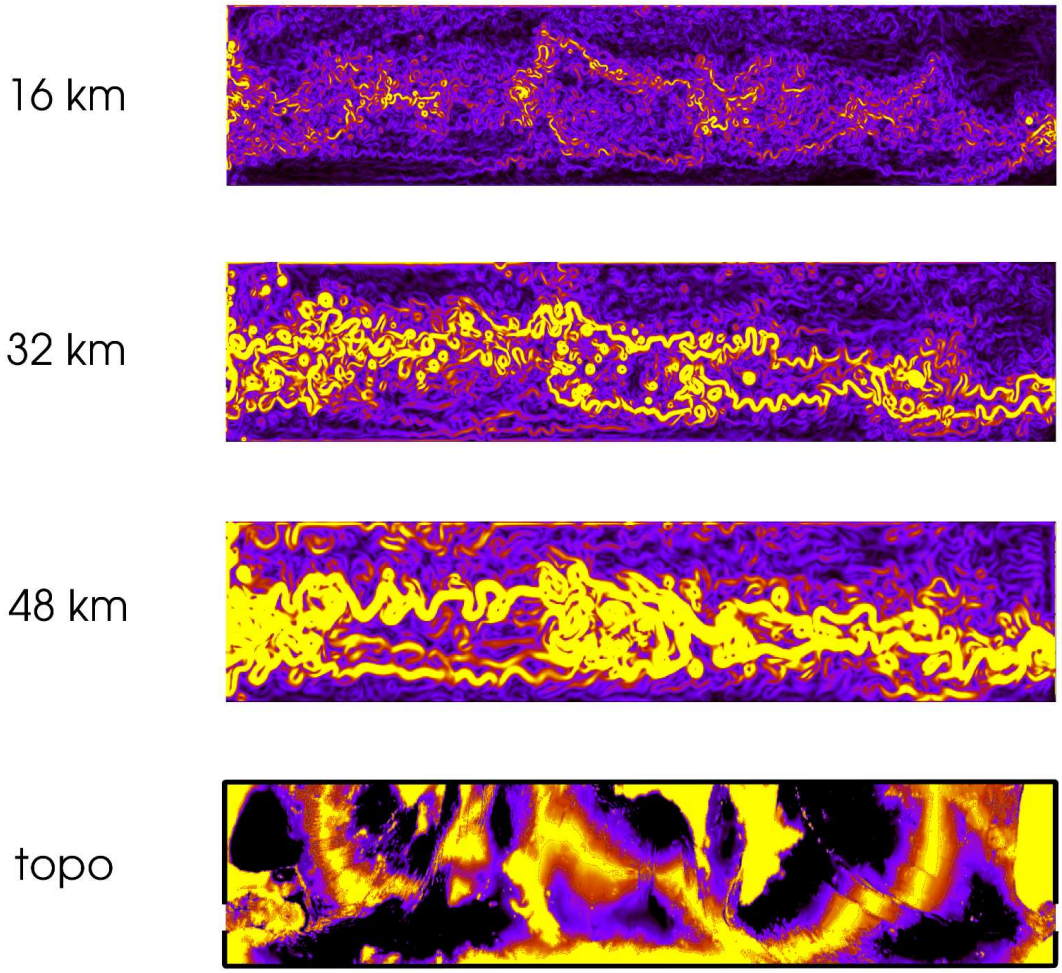

Figure 4–10: Same as Figure 4–9 but using realistic topography.

fields. With the Gaussian ridge, most of the kinetic energy is concentrated at the western part of the basin (see Figure 4–11a,c). The eddy kinetic energy is much more intense than the mean kinetic energy. Fields obtained with the realistic topography show a much richer structure. The eddy activity is significantly reduced in the western boundary region and distributed more uniformly along the path of the ACC. The kinetic energy of the mean flow is now of the same order of magnitude

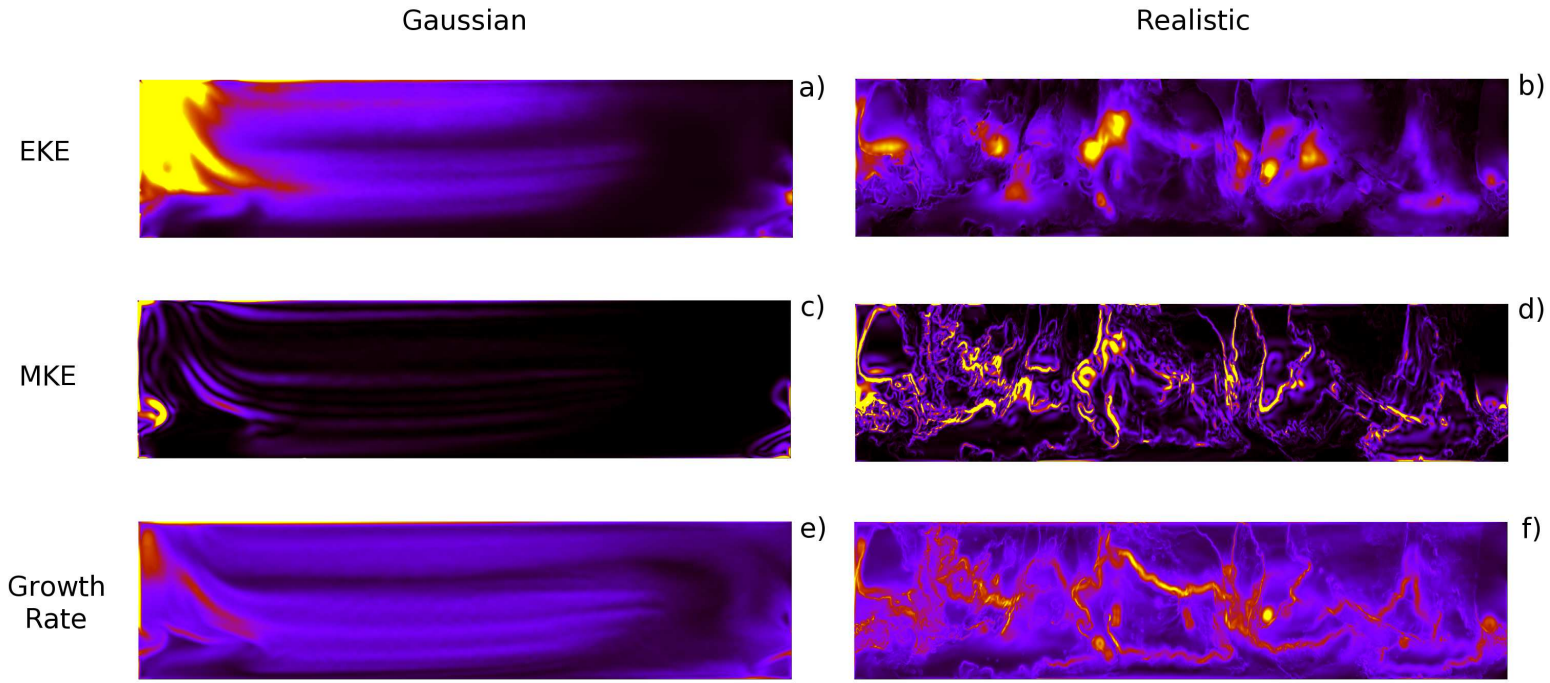

Figure 4–11: Comparison between time averaged fields of a), b) eddy kinetic energy $\frac{1}{2}\overline{\boldsymbol{u}\cdot\boldsymbol{u}} - \frac{1}{2}\overline{\boldsymbol{u}}\cdot\overline{\boldsymbol{u}}$, and c), d) mean kinetic energy, $\frac{1}{2}\overline{\boldsymbol{u}}\cdot\overline{\boldsymbol{u}}$ in the bottom layer for both topographies at $L_\rho = 32$ km and τ_0=0.2 N/m^2. Also shown is e), f) the Eady growth rate parameter, $\sigma \sim \sqrt{u_z^2 + v_z^2}$, at the interface between the two lowest layers.

as the eddy kinetic energy and its fine structure follows closely major topographic gradients. Figures 4–11e,f show the Eady growth rate parameter [*Eady*, 1949] obtained at the interface between the two lowest layers. This can be interpreted as a local measure of the baroclinic instability. Intense baroclinic instability occurs only in very narrow zones in the western and north western boundaries when using a Gaussian ridge. On the contrary, baroclinic instability occurs everywhere along the path of the circumpolar current when realistic topography is used.

Recall that the bottom layer domain-averaged total kinetic energy does not depend on the topography used whereas the top layer does (see Table 4–3 for $\tau_0 = 0.2$ N/m^2). This suggests an important role for the horizontal distribution of bottom kinetic energy in the vertical distribution of the circulation. As discussed in Chapter 3, the bottom layer kinetic energy is affected by the bottom friction. Since the bottom layer kinetic energy is proportional to the energy dissipation (neglecting the small amount dissipated by our biharmonic friction), it follows that abyssal kinetic energy to be equal in both experiments, provided the wind power source is equivalent. This appears to be the case here. The horizontal distribution of this bottom layer kinetic energy may then be affected by the topography. In the case with realistic topography, this implies more deep baroclinic instability and thus more kinetic energy in the upper layer. This suggests a mechanism whereby topographically-driven instabilities are propagated to the surface where they enhance the upper layer eddy field significantly.

To understand why the zonal transport is increased when using realistic topography, we show the barotropic streamfunctions for different wind stress amplitudes in Figure 4–12. Streamfunctions obtained using a Gaussian ridge have been discussed

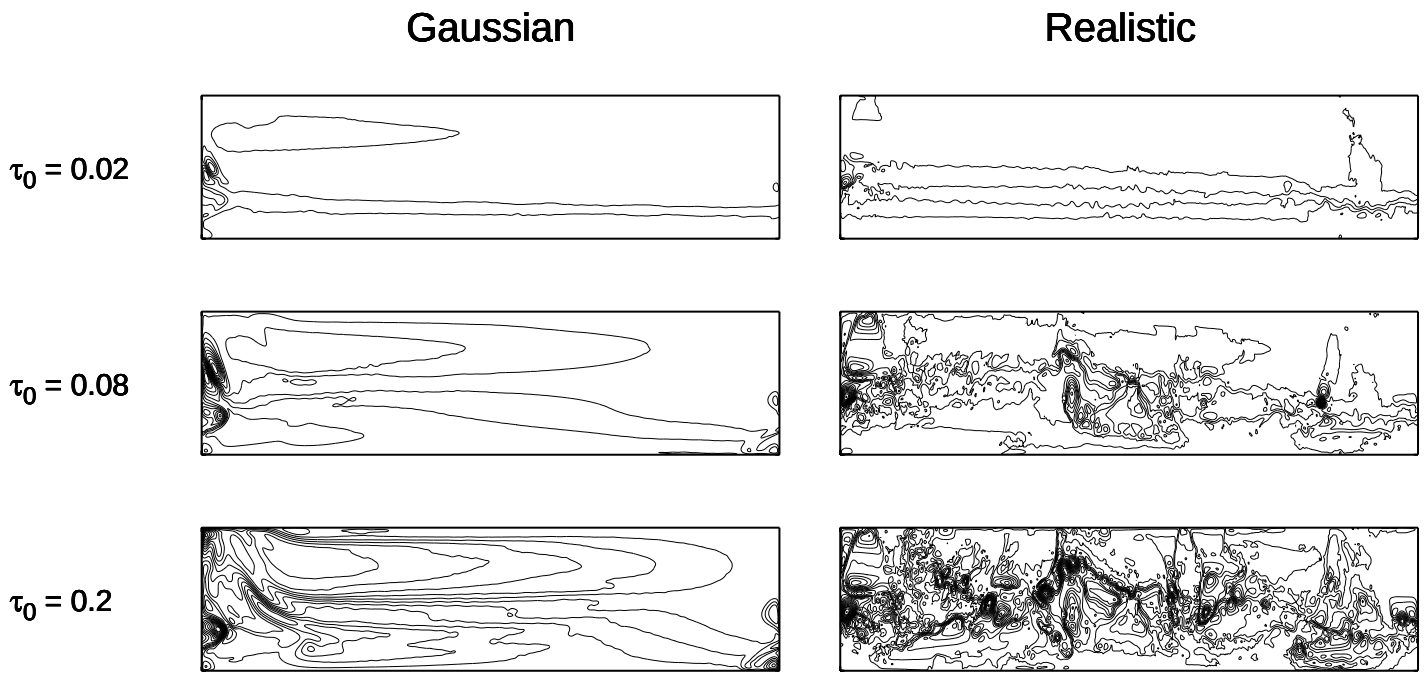

Figure 4–12: Time averaged barotropic streamfunction at different wind forcing amplitude for both topographies at L_ρ=32km.

extensively during this thesis. Here again, Sverdrup balance applies in the basin region and a recirculating Sverdrup gyre increasing with the wind stress is observed in the channel region. Moreover, an intense topographically driven recirculation is observed over the ridge in the bottom layer, as in Section 4.3.2 (not shown). Its signature can be observed in the barotropic streamfunctions, where all the streamlines follow the shape of the Gaussian ridge topography (bottom left corner of the domain). On the other hand, vertically averaged streamfunctions obtained using realistic topography look dramatically different. Sverdrup gyres are not evident and recirculations are divided into much smaller, more intense ones. The topographically-driven recirculations do not block Drake Passage as it was the case for the Gaussian ridge case. In a zonally reconnected channel, *Treguier and McWilliams* [1990] showed that the form stress increases with the wavelength of the topography. Here, when meridional walls are added, the horizontal distribution of the topography also seems to play significant role in the zonal momentum budjet. When the topography is distributed more uniformly along the path of the circumpolar current, the horizontal distribution of bottom layer kinetic energy is also more uniform. As a consequence, bottom layer topography driven recirculations are not concentrated in the Drake Passage region, and their blocking effect, described in Section 4.3.2, is reduced. Without this additional blocking of the channel, the numerical results are much closer to the transport values predicted by the analytic model (see Figure 4–8). This is despite the fact that Sverdrup circulation is not discernable in the barotropic streamfunction. That the transport matches well with our simple theory suggests that Sverdrup

recirculating gyres, even fractionated, still play an important role in the transport saturation.

Effect of the wind stress

We now study the effect of the wind on the zonal transport in this context of a realistic bottom topography. In a recent publication, *Hutchinson et al.* [2010] have shown that using a relative velocity wind stress representation increases the zonal transport in a zonally reconnecting channel using realistic topography, similar to the one used here. This representation of the wind stress is more realistic, and is known to damp the surface eddy field and reduce the wind power input to the circulation [*Duhaut and Straub*, 1994]. In the following, we revisit the experiment considered by *Hutchinson et al.*, except that we add partial meridional barriers mimicking Patagonia and Antarctica that were absent in thier simulations. In addition, we further investigate the effect of the wind stress by comparing this to a constant wind stress experiment similar to that of Chapter 3.

In the experiments using the relative velocity stress parametrization, we replace the reference wind forcing Equation (4.11) with

$$\boldsymbol{\tau}_1 = \rho_a C_d |\boldsymbol{u}_a - \boldsymbol{u}_o| (\boldsymbol{u}_a - \boldsymbol{u}_o), \tag{4.12}$$

where ρ_a is the air density at sea level, C_d is the air drag coefficient, $\boldsymbol{u}_o$ is the ocean surface velocity and $\boldsymbol{u}_a$ is the 10-m altitude atmospheric velocity. The atmospheric velocity is determined using the reference forcing (4.11) and the relative velocity stress 4.12 with $u_o = 0$

$$\boldsymbol{\tau}_{\text{ref}} = \rho_a C d |\boldsymbol{u}_a| \boldsymbol{u}_a = \widehat{i}\ \tau_0 \sin^2(\pi y / L_y). \tag{4.13}$$

In the experiments using a constant wind profile, we use the value of the reference wind stress in the middle of the channel and apply it over the entire domain. Note that since the middle latitude of the channel is approximately equal to $L_y/4$, this value is close to the meridional average of the reference wind stress. As such, all experiments in this section have approximately the same average wind stress in the channel.

Transport results for the experiments using the relative velocity stress parametrization and the constant wind profile are compared to the reference wind forcing in Figure 4–13 a). At very low wind stress, transport is equal for all experiments and fits

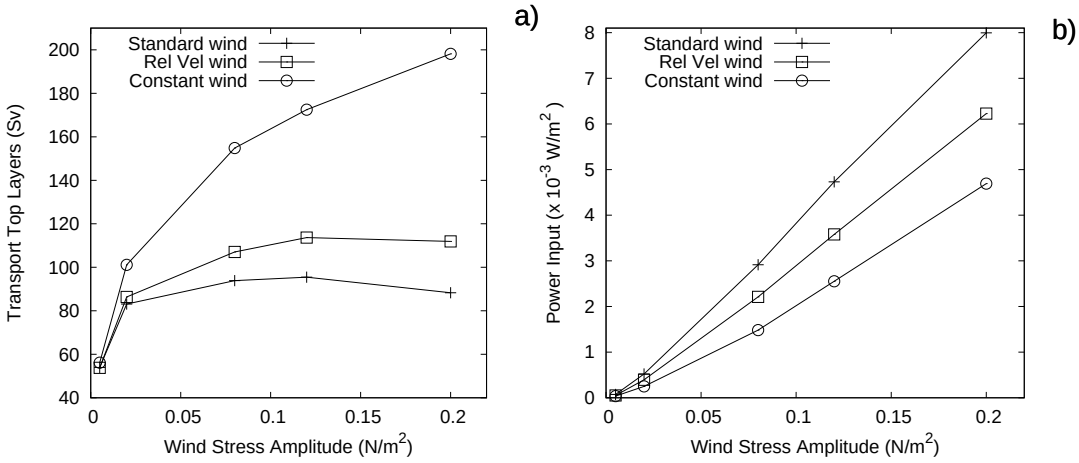

Figure 4–13: Results for the relative velocity stress and constant wind stress experiments compared with the standard $\sin^2(y)$ wind stress for a) the time-mean average zonal transport in the two upper layers and b) the time-mean domain averaged power input in function of the wind stress amplitude.

well the minimum channel contribution of *Straub* [1993]. For increasing wind stress, curves rapidly diverge. Experiments using the relative velocity stress parametrization

have a saturation value about 20 Sv higher than those using the reference wind. This behavior is consistent with the observations of *Hutchinson et al.* [2010]. Experiments without wind stress curl do not saturate and continue increasing as in Chapter 3. In both experiments, the total kinetic energy is reduced compared to the reference wind, the constant wind having the greater reduction (not shown). This again suggests an important role of the bottom layer recirculations. As discussed in chapter 3, for a given wind stress in the channel, reducing kinetic energy implies a weaker eddy field and a weaker momentum transfer to the bottom layer recirculations. Their influence to the upper layers circumpolar flow is then reduced consequently.

The domain averaged power input from the wind to the ocean, $P = \boldsymbol{u}_o.\boldsymbol{\tau}$, is shown in Figure 4–13b. The reference wind simulation has the strongest power input and weakest transport, whereas the constant wind stress experiment has the lowest power input and highest transport. This is consistent with the idea that weaker power input is associated with a weaker eddy field and that this reduces the influence of the abyssal recirculations, allowing for stronger circumpolar flow. However, for a given wind stress, the power input increases linearly for the different experiments, whereas this is not the case for the transport. Transport values obtained with the constant wind stress are significantly higher than the other experiments.

Comparison with a zonally reconnecting channel

We now begin the investigation of the third main subject of this chapter, which is the effect of the wind stress curl and Sverdrup circulation in a zonally reconnecting channel without meridional walls. We thus remove the peninsulas, i.e. we repeat the experiments at $L_\rho = 32$km using the same basin configuration except that L_{gap}

is now equal to the width of the channel ($L_y = 4000$km). To study the effect of the wind stress curl with and without peninsulas, two wind stress profiles are selected: i) the reference wind Equation (4.11), where $\boldsymbol{\tau}_{\text{ref}} \sim \tau_0 \sin^2(y) = \tau_0(0.5 - 0.5\cos(2y))$ and ii) half the reference wind stress curl, i.e. $\boldsymbol{\tau}_{\text{half}} \sim \tau_0(0.5 - 0.25\cos(2y))$. Transport results for these experiments are shown in Figure 4–14. With peninsulas, results are

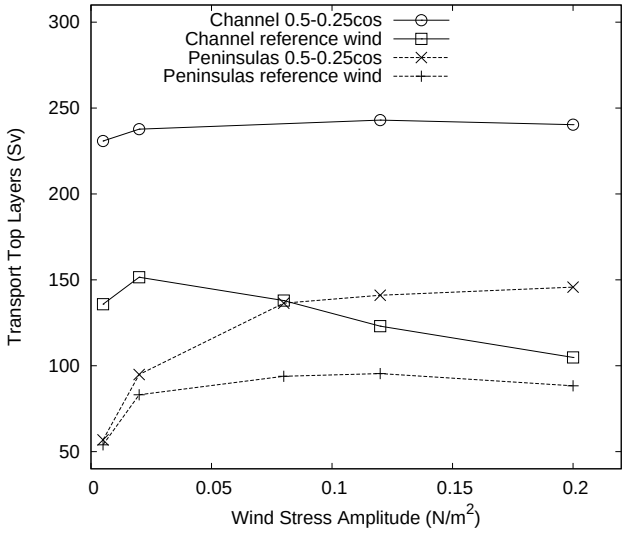

Figure 4–14: Time-mean zonal transport in the two upper layers for the experiments with and without meridional peninsulas using the reference wind and half wind stress curl profiles.

equivalent to those of Figure 4–13 a), i.e. both transports are equal at very low wind forcings and transport increases much faster in experiments with less curl. Without peninsulas, results with weaker wind curl are much higher than those obtained with the reference wind for all wind stress. In the saturation regime, tranport gradually decreases, and seems to converge to the value obtained with peninsulas. This is consistent with our results in chapter 2 which suggests that the width of Drake

Passage matters at low wind forcing whereas the wind stress curl seems to be the dominant parameter at strong forcing.

Upper layer streamfunctions obtained with and without peninsulas at weak and strong reference wind forcing are shown in Figure 4–15. In the the weak wind case, $\tau_0 = 0.02\text{N/m}^2$, the difference between the two geometries is obvious. A recirculating gyre in the northern half of the basin develops when peninsulas are present, and the number of circumpolar streamlines is reduced accordingly. In the the strong wind case, however, the difference between the two geometries is more difficult to distinguish. The bottom panel of Figure 4–15 shows the difference of these two streamfunctions. Most of the differences are localized at the eastern and western boundaries, close to the peninsulas. In the interior differences are small, except for a circumpolar streamline in the northern part of the domain. It thus appears that topography is acting in a similar way to solid boundaries when the eddy field is strong enough to allow the bottom recirculations to be felt by the upper layers. In the following section, we further investigate this phenomenon in a much simpler context of a two layer fluid in a zonally reconnecting channel partially blocked by a Gaussian ridge.

4.3.4 Sverdrup circulation in a zonally reconnecting channel

We now come back to the two layer model of Chapters 2 and 3, with the same 4000×10000 km rectangular basin, except that the peninsulas are now removed. The topography is a 2000m Gaussian ridge (half of the ocean depth) which is high enough to block the lower layer geostrophic contours. The upper layer depth is 1200m and lower layer 2800m. Three wind profiles are considered: i) our usual

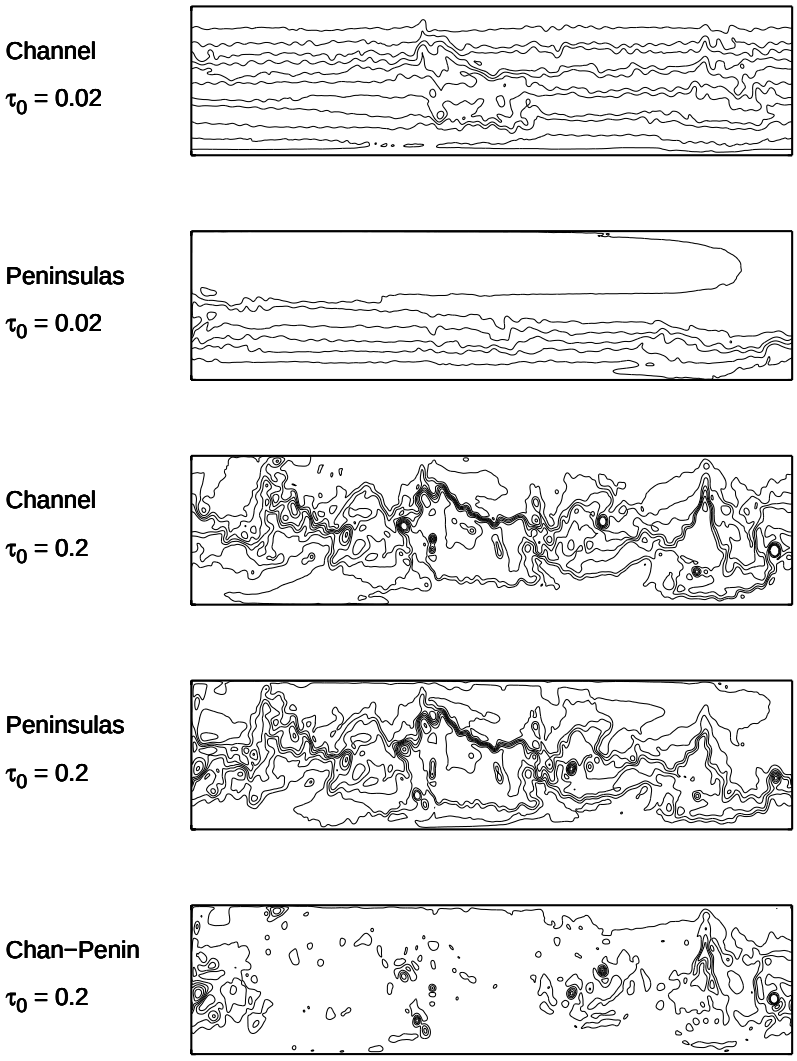

Figure 4–15: Comparison of the time averaged barotropic streamfunction with and without meridional peninsulas at weak and strong wind stress amplitude. Also shown is the difference field, $\psi_B^{\text{channel}} - \psi_B^{\text{peninsulas}}$, at strong forcing.

reference wind, where $\boldsymbol{\tau} \sim \tau_0(0.5 - 0.5\cos(2y))$, ii) half the wind reference stress curl, $\boldsymbol{\tau} \sim \tau_0(0.5 - 0.25\cos(2y))$ and iii) a constant wind stress $\boldsymbol{\tau} \sim \tau_0(0.5)$ equal to the average of the reference wind stress. All three profiles have the same average stress value; only the wind stress curl is varying.

Transport results for these experiments at $L_\rho = 16$km and $L_\rho = 32$km are shown in Figure 4–16. At each Rossby radius, transport obtained with the reference

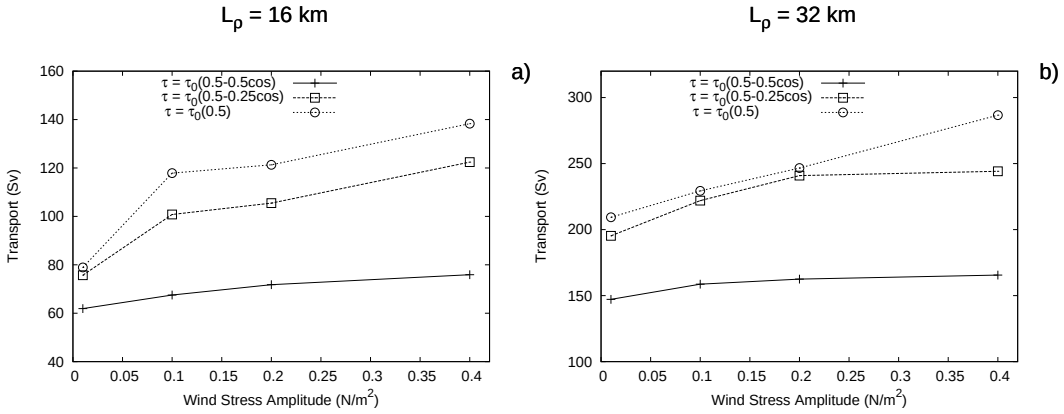

Figure 4–16: Upper layer average zonal transport obtained with the 2-Layers model at a) the $L_\rho = 16$km and b) the $L_\rho = 32$km for the wind stress curl reduction experiment.

wind is near its saturation value even for very low wind stress. This saturation behavior using a similar wind stress curl forcing in a zonally reconnecting channel partially blocked by a Gaussian ridge has also been observed by *Tansley and Marshall* [2001]. Experiments with half the wind stress curl show much higher transport values. Experiments with constant wind stress have even higher transport values, but much closer to the half curl experiment. This suggests a fast response of the transport when reducing the curl starting from the reference wind profile.

Figure 4–17 shows the evolution of barotropic srteamfunctions obtained using the reference wind stress at different amplitudes for $L_\rho = 16$km. At very low wind stress, streamlines are zonal, and the effect of the meridional topographic ridge is not evident. As the wind stress increases. the flow becomes less zonal and the position of the topographic ridge is clearly visible on the sides of the figure pannels. In the "interior", where the topography is flat, a Sverdrup circulation appears in the vertically averaged solution. This can be seen by looking at the right panels of Figure 4–17, where the analytic Sverdrup solution has been removed (the ridge crest was used as an eastern boundary to calculate the Sverdrup circulation analytically). At very low wind amplitude, this difference streamfunction, ψ_{diff}, is equal to ψ_B, which is represented by three zonally-oriented streamlines. As the wind amplitude increases, ψ_{diff} remains essentially the same with three zonally oriented circumpolar streamlines in the channel "interior". Here again, the topography acts as an effective meridional wall when the wind stress is strong enough. This suggests that the channel circulation is a superposition of a free channel mode — roughly independent of the wind forcing — and a Sverdrup circulation in which is injected all additional wind power input.

The idea that Sverdrup balance may apply in a zonally reconnecting channel has been proposed by *Wang and Huang* [1995]. In their linear barotropic channel model, the transport was expected to increase linearly with the wind stress. Here however, transport is saturated from very weak wind forcing. To better understand this phenomenon, we show the vertical structure of the flow in Figure 4–18. Recirculating gyres are clearly visible in the bottom layer solution. Signatures of these recirculating

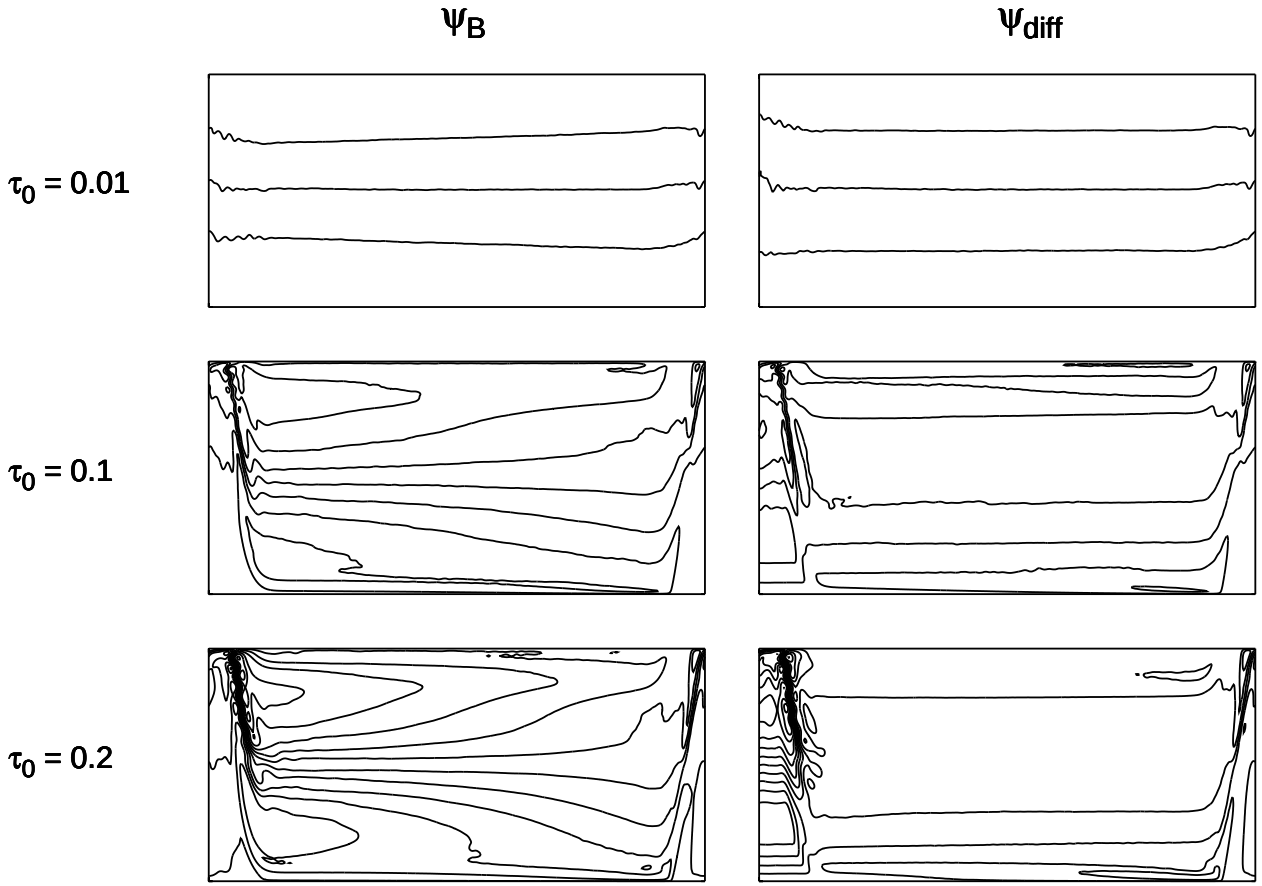

Figure 4–17: Time-mean barotropic streamfunction obtained with the reference wind stress at different amplitudes. Also shown is the difference field, ψ_{diff}, between the barotropic and the analytic Sverdrup streamfunctions.

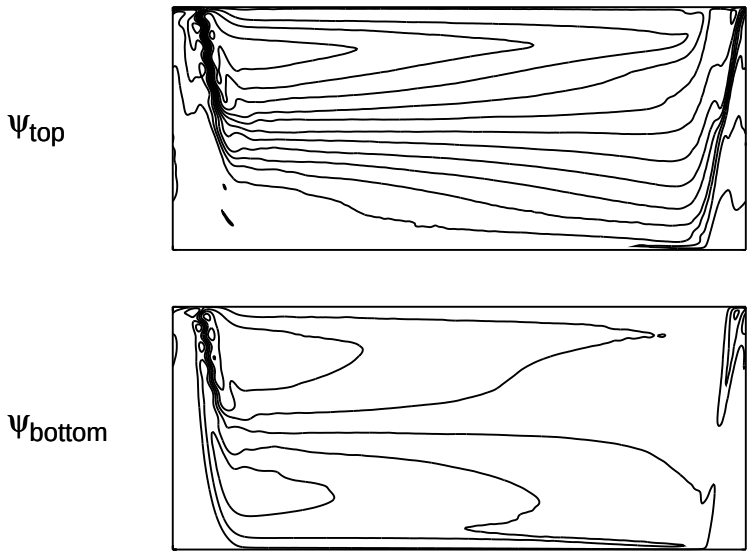

Figure 4–18: Time-mean streamfunction in each layers obtained with the reference wind stress at τ_0=0.2 N/m^2 and $L_\rho = 16$km.

gyres are also visible in the upper layer. Except over the ridge, a direct analogy with the vertical structure of the solution using peninsulas is possible. As was the case with meridional walls, recirculating gyres develop in the bottom layer, and those are felt by the upper layer, creating a recirculation there as well. This reinforces the idea that Sverdrup recirculating gyres act to reduce circumpolar flow in the saturation regime.

We emphasize that the wind stress curl is a fundamental parameter to this system. Figure 4–19 shows how the Sverdrup circulation gradually vanishes in the vertically averaged solution under a wind stress curl reduction. Keeping constant the average wind stress value, and reducing the wind curl, increases the number of circumpolar streamlines significantly. As the curl of the wind stress goes to zero,

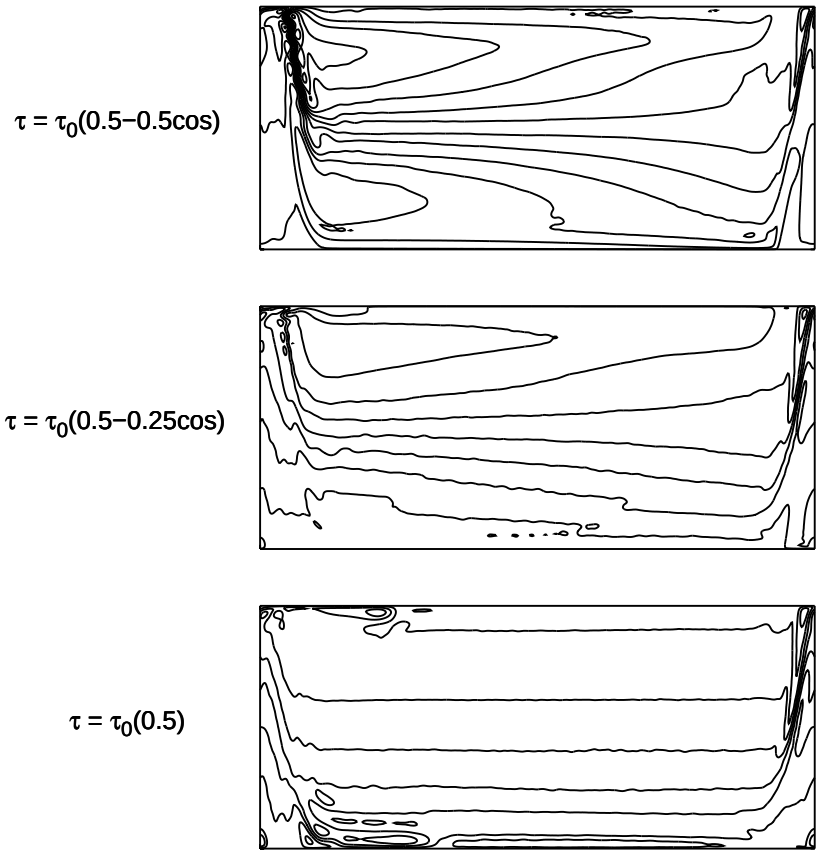

Figure 4–19: Time-mean barotropic streamfunction for different wind stress curl at τ_0=0.2 N/m^2 and L_ρ = 16km.

streamlines become more and more zonal, and a free mode similar to the one obtained in the low wind stress case is observed in the ocean interior. In the constant wind experiment, meridional deflection of the flow is localized over the topographic ridge. This suggests that when the wind stress curl is negligible, the downward interfacial momentum transfer is focalised over the topographic ridge itself. On the other hand, when the curl is turned on, bottom layer recirculating gyres are appearing downstream of the ridge and provide an additional means for transfering

momentum downward in regions where there is no topography. We hypothesize that it is this additional mechanism that explains the difference between the experiments with and without wind stress curl in the previous section (experiments using realistic topography).

4.4 Conclusion

In this chapter, we presented an analytic model of the basin contribution to the circumpolar current. This model assumes that the vertically integrated Sverdrup relation applies in the basin part of the domain, and that the potential vorticity is homogeneous inside a bowl. This defines a level of weak motion on $y = y_{\mathrm{DP}}$. Although this was calculated for a closed basin, it is taken to apply, at least approximately, for the case of a basin-like region adjacent to a channel south of $y = y_{\mathrm{DP}}$. When it descends below the ridge crest, this level of weak motion is then used to specify where the abyssal recirculation is strong enough to be felt in the upper part of the water column. Qualitatively, this produces a behavior similar to that of the 2-layer analytic model. Since choosing a level of weak motion is somewhat arbitrary, however, a quantitative estimate of the saturation value is not predicted.

Numerical experiments varying the vertical resolution show that the features assumed in the analytic model are observed in an idealized basin geometry. When inertial effects are weak, the solution with more vertical resolution gives transports similar to the 2-layer model. This suggests that the point, x_0, separating recirculating from circumpolar streamlines is well represented by the 2-layer analytic prediction using the first baroclinic mode (at least in the stratification tested). However, when

inertial effects are strong, the solution with more vertical resolution differs significantly from the 2-layer case and the transport is much reduced in the saturation regime. This is due to additional inertial effects not foreseen in the analytic model. The topographically-driven inertial recirculation blocks the outflow of Drake Passage, providing an additional barrier to the circumpolar current in the upper layer.

Numerical experiments using realistic topography show that this blocking effect of topographically-driven recirculation is much reduced when topography is more distributed. In this case, inertial recirculations also develop over major topographic obstacles; however, they do not form a meridional barrier to the circumpolar current in Drake Passage. Upper layer kinetic energy is increased significantly by the effect of the secondary zones of inertial dynamics in the basin interior. The result is that Sverdrup flow is hard to distinguish in the vertically averaged solution. However, the fact the the observed saturation value fits well the prediction of the analytic model suggests that Sverdrup gyres still play an important role in this system.

Numerical experiments using different wind stress specifications and realistic topography show that, for a given wind stress in the channel, any modification of the wind stress that reduces the eddy field seems to increase the transport. This again highlights the importance of bottom layer recirculating gyres in the zonal momentum budget of the circumpolar current. This is also true when meridional walls are removed. In this case, we find that meridional walls are crucial to determining the zonal transport at weak forcing, but become less and less important as the eddy field is more vigorous. In this stronger forcing regime, topography acts as an effective meridional wall through the indirect effect of the bottom layer inertial recirculations.

This, however, is only true when the wind stress curl is strong enough to drive these recirculations.

Numerical experiments using a 2-layer model in a zonally reconnecting channel geometry show how Sverdrup circulation can be an important part of the dynamics of circumpolar flows, even if there is no basin region. These experiments show how the fundamental assumptions of our analytic model might still hold in a channel flow partially blocked by topography. The circulation appears to be formed by the superposition of a free channel mode plus recirculating Sverdrup gyres. These Sverdrup gyres are locked over bottom layer recirculations forming downstream of the topography. When the wind profile is $\sin^2(y)$, the circumpolar transport is saturated from very low wind stress and all further increase of the wind profile amplitude goes in increasing the strength of the Sverdrup circulation. When using a reduced curl, but keeping the same averaged wind stress in the channel, transport saturation is much higher and is reached only at stronger wind stress values. In this case, increasing the amplitude of the wind profile enhance the free channel mode.

In sum, this chapter helps us to further understand the role of the wind stress curl and Sverdrup circulation on the circumpolar current. It clearly demonstrates that one cannot rule out the influence of recirculating gyres in the ACC dynamics in general and the zonal momentum budjet in particular. Our experiments show how adding a wind stress curl drastically changes the dynamics of the circumpolar flows. The ACC is of course far more complex than our simple idealized model. Nevertheless, we expect this recirculation phenomenon to apply a in more realistic model setting.

CHAPTER 5
Conclusion

In this thesis, the idea that Sverdrup dynamics may influence or control the circumpolar current has been investigated using idealized analytic and numerical models. The initial idea comes from the observation that Sverdrup gyres are clearly visible in the basin region of the time averaged solution of our idealized numerical model. An analytic model was developed based on this observation. Stommel's original idea has been modified to take into account that the Sverdrup balance is not directly applicable to the open Drake Passage latitudes and that not all of the Sverdrup flux into Drake Passage latitudes need necessarily feed the ACC. The circumpolar current is considered as a superposition of channel and basin contributions. The channel contribution follows from a momentum balance argument in the channel part, whereas the basin contribution follows from a potential vorticity balance argument in the basin region. The necessary condition for baroclinic instability is quickly reached at very weak wind forcing, and the transport stabilizes at a minimum value given by the earlier study of *Straub* [1993]. At stronger wind forcing, we assume that the additional source of eddies needed to close the momentum budget and meridional circulation in the channel part of the domain is provided by the adjacent basin-like flow. As such, this channel contribution need not increase significantly with the wind. Then, depending on the strength of the wind forcing, essentially two regimes are predicted for the basin contribution: i) the linearly increasing Stommel

regime, where all Sverdrup flux into the channel region is top trapped (and feeds the circumpolar flow) and ii) the saturation regime, where a certain a portion of the Sverdup flux instead feeds a recirculation, which extends throughout the water column. The vertical distribution of the Sverdrup flux into the channel region is then a fundamental element of this analytic model. This vertical structure is given essentially by the separatrix line between blocked and unblocked geostrophic contours in the abyss.

Reference wind stress

Using our reference wind stress, $\boldsymbol{\tau} \sim \sin^2(y)$, numerical experiments agree well with the general picture of the analytic model. In a 2-layer context, we carried out numerical simulations varying the basin length, the gap width, and the Rossby radius and found results to fit with the analytic predictions, except for an offset of the saturation regime. Essentially, it is found that this offset is sensitive to factors changing the vertical distribution of the circulation. More precisely, factors that can enhance or inhibit the bottom layer recirculating gyre will respectively decrease or increase the transport. Two examples of this are presented in this thesis: i) the effect of a continental ridge topography along the western boundary and ii) the effect of bottom friction. A continental ridge topography at the western boundary enhances the eddy activity in the basin interior. Manifestations of this phenomenon are visible as zonal jets emanating from the boundary region. As a result, enhanced vortex stretching drives a stronger bottom layer recirculation, without affecting the barotropic Sverdrup solution. The bottom layer flow is then observed to extend east of the analytic separatrix, and saturation is reached at lower forcing amplitudes than

what is predicted by the analytic model. The other example relates to the effect of the bottom drag coefficient. This parameter has a direct impact on the lower layer circulation. Increasing the bottom drag reduces the strength of the bottom layer recirculating gyre, but again does not affect the vertically integrated Sverdrup solution. This implies a more top trapped Sverdrup flux into the channel region, and therefore a stronger ACC. In other words, stronger bottom drag leads to an extended Stommel regime and an incomplete saturation at higher values of forcing. Decreasing the bottom drag has the opposite effect, with a shorter Stommel regime and a lower saturation.

Wind stress vs wind stress curl

In Chapter 3, experiments where a constant wind stress is added to the reference wind profile show an increased zonal transport. However, the addition of constant wind does not affect either the bottom layer recirculating gyre or the barotropic Sverdrup circulation in the basin region. Its effect is instead limited to the upper layer in the channel region. Essentially, changing the wind stress in the channel (without changing the wind stress curl) affects how much of the Sverdrup flux into the Drake Passage latitude band feeds circumpolar flow and how much feeds a recirculation gyre. We had originally assumed the top trapped portion of the Sverdrup flux would feed circumpolar flow, whereas the remainder would not. Our simulations suggest, however, that this partitioning depends on the strength of the wind stress at channel latitudes. Thus, while a significant channel part of the transport (in the sense of circumpolar streamlines that do not connect to the Sverdrup interior) is not evident in our simulations, it seems likely that what determines how much of the Sverdrup

flux feeds into the circumpolar current may well be determined by considerations such as those made in channel theories of the transport. Specifically, it is well known that transient eddies are needed to close the meridional circulation across zonally reconnecting potential vorticity contours. In our analytic model, we assumed that, except for very weak forcing, the gyre would provide an adequate source of these eddies. This appears not to be the case in the regime where the wind stress is dominant relative to the curl.

Experiments without meridional barriers in Chapter 4 provide some hints as to how to incorporate the wind stress amplitude into the analytic model. In these experiments, there is obviously no basin contribution; however, Sverdrup gyres were nonetheless observed (with a blocking ridge taking the place of meridional boundaries). The total circulation can then be thought of as the sum of a Sverdrup part (which has zero transport) and what appears similar to a free mode (and contains all of the circumpolar transport). Determining the transport (in our open channel simulations) is then equivalent to determining the amplitude of this mode. Our experiments show it to depend critically on the relative amplitudes of the wind stress and wind stress curl. When the curl is sufficiently strong, a saturation regime is observed, much as in our experiments with meridional walls. When the curl is set to zero, the Sverdrup gyres disappear and the transport is enhanced significantly. (Addition of a double gyre forcing then reduces the transport.) We speculate that this behaviour relates to the interface slopes associated with the gyres and the circumpolar mode, which add so that the flow in the centre latitudes of the domain are more baroclinically unstable than would be the case with one or the other by itself. If

one considers that transport saturates when an adequate source of baroclinic eddies is available, then it is natural that the transport should depend on both the stress and the curl, since both affect the interface height field slope.

We suspect that a similar argument could also explain the behaviour seen in experiments of Chapter 3, discussed above. The analytic model includes a 'basin part' and a 'channel part', with the latter determined by the necessary condition for baroclinic instability. Other channel models assume that stronger stress implies the need for more baroclinic instability, and therefore a steeper interface height field tilt, implying more transport. We suggest that a more global analysis of baroclinic instability may be fruitful. In other words, it may be that the increase in baroclinic instability needed upon adding a wind stress does not occur locally in the channel latitudes, or even along the path of the ACC. Moreover, the presence of both Sverdrup gyres, and possibly of the structure of a free circumpolar mode would have to be taken into account.

Continuous stratification

The generalization of the analytic model to the continuously stratified case is not straightforward. Starting from the framework of *Rhines and Young* [1982], we make the following assumptions: i) the Sverdrup balance applies in the barotropic solution, ii) the potential vorticity homogenizes inside a bowl defined by the level of no — or weak — motion, iii) flow is negligible where potential vorticity contours are blocked. We also assume that when the level of weak motion descends below the ridge crest, the abyssal recirculation is sufficiently strong to drive a recirculation in the upper part of the water column. The transport associated with the basin contribution in

the this extension to our original model has a similar structure as before, i.e., with a Stommel regime and a saturation regime set by a level of weak motion. In the numerical experiments, most of the assumptions of the analytic model do apply. Simulations show that the Sverdrup flux into the channel region is still divided into a recirculating gyre and a "top-trapped" circumpolar part. When inertial effects are small, the position x_0, separating these two parts does not change when going from 2 to 5 layers and the transport is insensitive to the increase of vertical resolution. This suggests that x_0 is well represented by the equivalent analytic 2-layer separatrix obtained with the first baroclinic Rossby radius. However, when the eddy field is more vigorous, the solution with more vertical resolution diverges from the 2-layer solution. A better representation of the high baroclinic modes enhances the vortex tube stretching, which drives a strong inertial recirculation over the Scotia ridge. This recirculation extends through all the water column, and is seen by the circumpolar current as an additional barrier—so that transport is significantly reduced. Referring back to the experiments with reduced bottom drag of Chapter 3, it is possible that this phenomenon also plays a role in the decrease of the transport in the saturation regime. That is, a similar recirculation is also observed and reduction of the transport in the saturation regime is also observed there (cf, the 0.5×r case in Figure 3–3).

Realistic topography

The use of realistic topography has a significant impact on the flow pattern and transport of the numerical solution. A global enhancement of the upper layer eddy field is observed when using realistic topography compared to the Gaussian ridge case. With realistic topography, baroclinic instability occurs everywhere along the

path of the ACC, whereas this occurs mainly in the western boundary region in the Gaussian ridge case. This suggests an important role of the horizontal distribution of the bottom layer kinetic energy in the vertical distribution of the flow.

More relevant to us is the fact that topographically driven recirculations no longer block Drake Passage, but rather, are distributed more uniformly along the path of the ACC. A result of this is that the simulated transport fits well with the prediction of our analytic model. This suggests that the mechanisms for transport saturation described in this thesis can apply even in situations where the Sverdrup gyres are not directly visible in the vertically averaged solution.

Future work

The main goal of this thesis was to better identify the mechanisms controlling the dynamics and transport of an idealized fixed stratification ACC. A general conclusion of this study is that both momentum and vorticity dynamics should be considered when theorizing on this current. This study also highlights the perhaps not surprising fact that a simple theory describing transport as a function of forcing and model parameters is difficult to obtain, even in the quasigeostrophic context that we considered. A fundamental question is to know how to generalize the analytic model to a framework where the meridional density profile is allowed to change with the increasing wind. This is the main weakness of the analytic model presented here. Another important problem is the influence of a meridional or variable wind stress component. Is the eddy field enhanced when adding such components? If so, how does transport react? As mentioned above, more work remains to be done to incorporate the amplitude of the channel wind stress into our model. Throughout

most of this thesis, we focused on explaining the basin dynamics to the north of the ACC and how they might influence or determine the transport. It may prove equally, or more fruitful to redefine what we mean by 'basin' and 'channel' parts of the overall circulation. If the 'basin part' is taken to be the closed gyres (which can be influenced by Sverdrup dynamics even in the absence of meridional boundaries, but which by definition to not contribute to the transport), then the problem becomes to understand what sets the amplitude and structure of the 'channel mode'. For example, it may be that this mode is interpretable as a free mode of the system. What sets its amplitude is clearly a function of both the wind stress and the wind stress curl, and may be related to the baroclinic instability properties of the larger domain, i.e., as opposed to the stability properties along the path of the ACC per se.

It is likely, however, that an extended version of our analytic model that takes these factors into account would loose much of its simplicity. Moreover, it is worth pointing out that the time averaged wind stress blowing over the Southern Ocean has the shape of a zonal jet, similar to the shape of our reference wind profile. Moreover, for this profile, our numerical simulations agree reasonably well with our simple analytic model. In other words, the effect of the wind stress curl is likely to be more important in the ACC, and some of the subtleties relating to the wind stress mentioned above may be less important.

Recent publications on the ACC often begin with a statement to the effect that the absence of meridional boundaries implies that the Sverdrup balance does not apply in the Southern Ocean, although it may apply locally in certain parts of the

domain. This has led to Sverdrup, or more generally, basin dynamics being dismissed as irrelevant to the dynamics of the ACC. Our experiments show examples where the Sverdrup balance does apply over most of the domain — even in the absence of meridional boundaries — when the wind stress curl is dominant. Moreover, we have shown that the presence of Sverdrup gyres and eddy-driven abyssal recirculations can have a profound influence on the circumpolar transport.

Appendix A: 2-Layered Quasi-Geostrophic Cirulation

When we consider the 2-layer qasigeostrophic potential vorticity quetations for large scale steady state circulation and neglect dissipation and relative vorticity, they reduce to

$$\begin{aligned} \mathrm{J}\left[\psi_1, (F_1\psi_2 + \beta y)\right] &= \frac{\widehat{k}\cdot\nabla\times\tau}{\rho_0 H_1} \qquad (5.1) \\ \mathrm{J}\left[\psi_2, (F_2\psi_1 + \beta y)\right] &= 0\ , \qquad (5.2) \end{aligned}$$

where $F_1 = \frac{f_0^2}{g'H_1}$ and $F_2 = \frac{f_0^2}{g'H_2}$. Then, let us consider the two following solutions to the system of equations (5.1) and (5.2):

Barotropic solution

If we compute $\frac{H_1\cdot\text{Eq.(5.1)}+H_2\cdot\text{Eq.(5.2)}}{H_1+H_2}$, the strectching terms cancels and we obtain

$$\beta\frac{\partial\psi_B}{\partial x} = \frac{\widehat{k}\cdot\nabla\times\tau}{\rho_0 H}, \qquad (5.3)$$

where $\psi_B = \frac{H_1\psi_1+H_2\psi_2}{H_1+H_2}$ is the barotropic stream function. Note that this is the same equation that the Sverdrup Balance (Equation 1.2).

Baroclinic solution

On the other hand, if we define the baroclinic stream function as $\psi' = \psi_2 - \psi_1$ and substract Equations (5.1) and (5.2), we obtain

$$\beta\frac{\partial\psi'}{\partial x} + \frac{f_0^2}{g'}\left(\frac{1}{H_1}+\frac{1}{H_2}\right)\mathrm{J}(\psi_2,\psi_1) = -\frac{\widehat{k}\cdot\nabla\times\tau}{\rho_0 H}. \qquad (5.4)$$

Then, we can write this result in terms of ψ_B and ψ'

$$\beta\frac{\partial\psi'}{\partial x} - \frac{1}{L_\rho^2}\mathrm{J}(\psi_B,\psi') = -\frac{\widehat{k}\cdot\nabla\times\tau}{\rho_0 H}, \tag{5.5}$$

where $L_\rho = \frac{\sqrt{\frac{g' H_1 H_2}{H_{\mathrm{Tot}}}}}{f_0}$ is the Rossby radius of deformation. After some algebra, we can rearrange Equation (5.5) to obtain

$$\mathbf{c}\cdot\nabla\psi' = L_\rho^2\frac{\widehat{k}\cdot\nabla\times\tau}{\rho_0 H}, \tag{5.6}$$

where the vector $\mathbf{c}$ is the characteristic velocity

$$\mathbf{c} = \mathbf{u}_B - L_\rho^2\beta\,\widehat{i}. \tag{5.7}$$

The lines of characteristics are then defined by the stream function of the characteristic velocity $\mathbf{c} = \widehat{k}\times\nabla\Phi$

$$\Phi = \psi_B + \beta L_\rho^2 y. \tag{5.8}$$

As disscussed in the introduction section, when the wind forcing is weak, the characteristics are straight latitudinal bands of $\beta L_\rho^2 y$. As the wind stress becomes stronger, ψ_B slowly increases and distort these straight latitudinal bands. To see the link between these characteristics contours and the circulation of the second layer, we can come back in Equation (5.2) and replace ψ_1 by $\frac{H_{\mathrm{Tot}}\psi_B - H_2\psi_2}{H_1}$, we obtain

$$\mathrm{J}\left[\psi_2,(\psi_B + L_\rho^2\beta y)\right] = 0, \tag{5.9}$$

which implies that

$$\mathrm{J}\left[\psi_2,\Phi\right] = 0. \tag{5.10}$$

The only way that Equation (5.10) can be satisfied is that $\psi_2 = \psi_2(\Phi)$. Hence, it is clear that in regions of blocked Φ contours, ψ_2 must equal zero to satisfy the no normal flow condition at the boundaries.

Appendix B: Approximate solution for $T_{\rm sat}$

We find numerically that once x_0 is to the east of $x_{\rm west}$, our estimate, $T_{\rm sat}$, of $T_{\rm basin}$ appears to become constant. It is not obvious a priori that this should be the case. Here, we consider two limits in which the equations can be simplified considerably and show that $T_{\rm sat}$ is constant in each. That is, we show that x_0 is inversely proportional to the forcing amplitude. We consider the case of a small Rossby radius (L_ρ ∼10km) — corresponding to that of the Southern Ocean — and distinguish between 1) $\alpha \to 0$, corresponding to linear stratification, for which D and ℓ_μ are of the same order and 2) a surface intensified stratification, for which $D \gg \ell_\mu$ (cf. Figure 4–2).

Linear stratification

The barotropic streamfunction for a linear stratification,

$$\psi_B = \frac{\lambda}{6} D^3, \tag{5.11}$$

is obtained solving (4.1) with $N = N_0$. The fraction μ of the flow lying above ℓ_μ,

$$\mu\psi_B = \frac{\lambda}{6}[D^3 - (\ell_\mu - D)^3], \tag{5.12}$$

is obtained similarly solving (4.7). Combining (5.11) and (5.12) gives

$$\mu D^3 + 3D^2\ell_\mu + 3D\ell_\mu^2 + \ell_\mu^3 = 0. \tag{5.13}$$

Since $\mu \sim 1$, this can be written as $(D + \ell_\mu)^3 \approx 0$ so that

$$D \approx -\ell_\mu. \tag{5.14}$$

Combining this with (4.3) and (5.11) gives that

$$\ell_\mu^3 \sim \frac{1}{\lambda(y)}(L_x - x)(\nabla \times \boldsymbol{\tau}). \tag{5.15}$$

Further taking the point $x = x_0$ to be where $\ell_\mu = h_{\text{ridge}} = \text{const}$ and $y = y_{\text{DP}}$, we get that $x_0 \sim (\nabla \times \boldsymbol{\tau})^{-1}$, implying $T_{\text{sat}} \approx \text{constant}$.

Exponential stratification

For an exponential stratification and small L_ρ, we have that $D \gg \alpha$ so that $e^{-\alpha D} \to 0$ in (4.5) and (4.7). Combining these two approximated equations gives

$$(1 - \mu)(\alpha D - 2) - (\alpha(D - \ell_\mu) - 2)e^{-\alpha \ell_\mu} = 0, \tag{5.16}$$

which can be rearranged as

$$D = \frac{2(1 - \mu) - (\alpha \ell_\mu + 2)e^{-\alpha \ell_\mu}}{(1 - \mu) - e^{-\alpha \ell_\mu}}. \tag{5.17}$$

Evaluating this at $x = x_0$ defined as above (i.e., such that $\ell_\mu(x_0, y_{\text{DP}}) = h_{\text{ridge}}$) gives that $D \approx \text{constant}$. Then, using (4.3), $e^{-\alpha D} \to 0$ and $\alpha D \gg 2$ in (4.5) gives

$$D \sim \frac{1}{\lambda}(L_x - x_0)(\nabla \times \boldsymbol{\tau}) \tag{5.18}$$

Since $D \approx$ constant, we again find that x_0 is inversely proportional to the forcing strength.

Finally, recall that in this limit, ℓ_μ is nearly independent of x (cf. Figure 4–2a),

except near the eastern boundary. It is straightforward to derive an approximate expression for the level at which this occurs as a function of μ. Using $D \gg \ell_\mu$, $D \gg 1/\alpha$ and $e^{-\alpha D} \to 0$ in (4.7) gives

$$\mu\psi_B \approx \frac{\lambda}{\alpha^2} D(1 - e^{-\alpha \ell_\mu}). \tag{5.19}$$

Then combining $\psi_B \approx \frac{\lambda}{\alpha^2} D$ from (4.5) and (5.19) gives

$$\ell_\mu \approx -\frac{1}{\alpha} \ln(1 - \mu), \tag{5.20}$$

which agrees with Figure (4–2).

References

Allison, L. C., H. L. Johnson, D. P. Marshall, and D. R. Munday, Where do winds drive the antarctic circumpolar current?, *Geophysical Research Letters*, *37*, 2010.

Arakawa, A., Computational design for long-term numerical integrations of the equations of atmospheric motion, *J. Comput. Phys.*, *1*, 119–143, 1966.

Baker, D. J., A note on sverdrup balance in the southern ocean, *Proc. Natl. Atl. Acad. Sci.*, *40*, 21–26, 1982.

Barnier, B., B.L., and C. Le Provost, On the catalytic role of high baroclinic modes in eddy-driven large-scale circulations, *Journal of Physical Oceanography*, *21*, 976–997, 1991.

Becker, J. M., and R. Salmon, Eddy formation over a continental slope, *Journal of Marine Research*, *55*, 181–200, 1997.

Briggs, W. L., V. E. Henson, and S. F. McCormick, *A Multigrid Tutorial*, second ed., SIAM, 2000.

Dewar, W. K., Topography and barotropic transport control by bottom friction, *Journal of Marine Research*, *56*, 295–328, 1998.

Doos, K., and D. J. Webb, The deacon cell and other meridional cells of the southern ocean., *Journal of Physical Oceanography*, *24*, 429–442, 1994.

Duhaut, T., and D. Straub, Wind stress dependence on ocean surface velocity: Implications for mechanical energy input to ocean circulation, *Journal of Physical*

Oceanography, *36*, 202–211, 1994.

Eady, E., Long waves and cyclone waves, *Tellus*, *1*, 33–52, 1949.

Gent, P., W. Large, and F. Bryan, What sets the mean transport through Drake Passage?, *Journal of Geophysical Research*, *106*, 2693–2712, 2001.

Gill, A., A linear model of the antarctic circumpolar current, *Journal of Fluid Mechanics*, *32*, 465–488, 1968.

Gnanadesikan, A., and R. W. Hallberg, On the relationship of the circumpolar current to southern hemisphere winds in coarse-resolution ocean models., *Journal of Physical Oceanography*, *30*, 2013–2034, 2000.

Hallberg, R., and A. Gnanadesikan, An exploration of the role of transient eddies in determining the transport of a zonally reentrant current., *Journal of Physical Oceanography*, *31*, 3312–3330, 2001.

Hallberg, R., and A. Gnanadesikan, The role of eddies in determining the structure and response of the wind-driven southern hemisphere overturning: Results from the modeling eddies in the southern ocean (MESO) project, *Journal of Physical Oceanography*, *36*, 2232–2252, 2006.

Henning, C. C., and G. K. Vallis, The effects of mesoscale eddies on the stratification and transport of an ocean with a circumpolar channel., *Journal of Physical Oceanography*, *35*, 880–896, 2005.

Hogg, A. M., and J. R. Blundell, Interdecadal variability of the southern ocean., *Journal of Physical Oceanography*, *36*, 1626–1645, 2006.

Hughes, C. W., Sverdrup-like theories of the antarctic circumpolar current, *Journal of Marine Research*, *60*, 1–17, 2002.

Hutchinson, D., A. Hogg, and B. J.R., Southern ocean response to relative velocity wind stress forcing, *Journal of Physical Oceanography*, *40*, 326–339, 2010.

Johnson, G. C., and H. Bryden, On the strength of the circumpolar current, *Deep-Sea Res.*, *36*, 39–53, 1989.

Karsten, R., H. Jones, and J. Marshal, The role of eddy transfer in setting the stratification and transport of a circumpolar current, *Journal of Physical Oceanography*, *32*, 39–54, 2002.

Killworth, P. D., An equivalent-barotropic mode in the fine resolution antarctic model., *Journal of Physical Oceanography*, *22*, 1379–1387, 1992.

Krupitsky, A., and M. A. Cane, A two-layer wind-driven ocean model in a multiply connected domain with bottom topography., *Journal of Physical Oceanography*, *27*, 2395–2404, 1997.

MacCready, P., and P. B. Rhines, Meridional transport across a zonal channel: Topographic localization, *Journal of Physical Oceanography*, *31*, 1427–1439, 2001.

Marsh, R., A. J. G. Nurser, A. P. Megann, and A. L. New, Water mass transformation in the southern ocean of a global isopycnal coordinate gcm., *Journal of Physical Oceanography*, *30*, 1013–1045, 2000.

Marshall, J., and T. Radko, Residual-mean solutions for the antarctic circumpolar current and its associated overturning circulation, *Journal of Physical Oceanography*, *33*, 2341–2354, 2003.

Marshall, J., D. O. Olbers, H. Ross, and D. Wolf-Gladrow, Potential vorticity constraints on the dynamics and hydrography of the southern ocean., *Journal of Physical Oceanography*, *23*, 465–487, 1993.

Maximenko, N. A., B. Bang, and H. Sasaki, Observational evidence of alternating zonal jets in the world ocean, *Geophysical Reasearch Letters*, *32*, 2005.

Mazloff, M. R., P. Heimbach, and C. Wunsch, An eddy-permitting southern ocean state estimate., *Journal of Physical Oceanography*, *40*, 880–899, 2010.

McWilliams, J., A note on a consistent quasigeostrophic model in a multiply connected domain, *Dyn. Atmos. Oceans*, *1*, 427–441, 1977.

McWilliams, J. C., W. R. Holland, and J. H. S. Chow, A description of numerical Antarctic Circumpolar Currents., *Dyn. Atmos. Oceans*, *2*, 213–291, 1978.

Munk, W., and E. Palmén, Note on the dynamics of the Antarctic Circumpolar Current., *Tellus*, *3*, 53–55, 1951.

Nadeau, L.-P., and D. Straub, Basin and channel contributions to a model antarctic circumpolar current, *Journal of Physical Oceanography*, *39*, 986–1002, 2009.

Nadiga, B., On zonal jets in oceans, *Geophysical Research Letters*, *33*, 2006.

Nakano, H., and H. Hasumi, A series of zonal jets embedded in the broad zonal flows in the pacific obtained in eddy-permitting ocean general circulation models, *Journal of Physical Oceanography*, *35*, 474–488, 2005.

Olbers, D., and M. Visbeck, A model of the zonally averaged stratification and overturning in the southern ocean., *Journal of Physical Oceanography*, *35*, 1190–1205, 2005.

Olbers, D., D. Borowski, C. Voelker, and J.-O. Wolff, The dynamcal balance, transport, and circulation of the antarctic circumpolar current., *Antarctic Science*, *16*, 439–470, 2004.

Panetta, R. L., Zonal jets in wide baroclinically unstable regions: Persistence and scale selection, *Journal of the Atmospheric Sciences*, *50*, 2073–2106, 1993.

Patra, P. K., S. Maksyutov, M. Ishizawa, T. Nakazawa, T. Takahashi, and J. Ukita, Interannual and decadal changes in the sea-air CO2 flux from atmospheric CO2 inverse modeling., *Global Biogeochemical Cycles*, *19*, 2005.

Pedlosky, J., *Ocean Circulation Theory*, Springer, 1996.

Press, W. H., S. A. Teukolsky, W. T. Vetterling, and B. P. Flannery, *Numerical Recipes in Fortran 90*, vol. 2, Cambridge, 1996.

Rhines, P., Waves and turbulence on a beta-plane, *J. F. Mech.*, *69*, 417–443, 1975.

Rhines, P., and R. Schopp, The wind-driven circulation: Quasi-geostrophic simulations and theory for nonsymmetric winds, *Journal of Physical Oceanography*, *21*, 1438–1469, 1991.

Rhines, P., and W. Young, A theory of wind driven circulation. **I**. Mid-ocean gyres, *Journal of Marine Research*, *40*, 1982.

Rintoul, S., C. Hughes, and D. Olbers, *Ocean circulation and climate*, chap. The Antarctic Circumpolar Current system, p. 271–302, Academic Press, New York, 2001.

Stommel, H., A survey of ocean current theory, *Deep-Sea Res.*, *6*, 149–184, 1957.

Straub, D. N., On the transport and angular momentum balance of channel models of the Antarctic Circumpolar Current, *Journal of Physical Oceanography*, *23*, 776–782, 1993.

Tansley, C. E., and D. P. Marshall, On the dynamics of wind-driven circumpolar currents, *Journal of Physical Oceanography*, *31*, 3258–3273, 2001.

Treguier, A., and J. C. McWilliams, Topographic influences on wind-driven, stratified flow in a β-plane channel: An idealized model for the antarctic circumpolar current, *Journal of Physical Oceanography*, *20*, 321–343, 1990.

Wang, L., and R. Huang, A linear homogeneous model of wind-driven circulation in a β-plane channel, *Journal of Physical Oceanography*, *25*, 587–603, 1995.

Warren, B., J. LaCase, and P. A. Robbins, On the obscurantist physics of form drag in theorizing about the circumpolar current., *Journal of Physical Oceanography*, *26*, 2297–2301, 1996.

Webb, D., A simple model of the effect of the Kerguelan Plateau on the strength of the Antarctic Circumpolar Current., *Geophys. Astrophys. Fluid Dynamics*, *70*, 57–84, 1993.

Wolff, J.-O., E. Maier-Reimer, and D. J. Olbers, Wind-driven flow over topography in a zonal -plane channel: A quasi-geostrophic model of the antarctic circumpolar current., *Journal of Physical Oceanography*, *21*, 236–264, 1991.

Wunsch, C., The work done by the wind on the oceanic general circulation., *J. Phys. Oceanogr.*, *28*, 2332–2340, 1998.

Wyrtki, K., The antarctic circumpolar current and the antarctic polar front., *Deutsche Hydrographische Zeitschrift*, *13*, 153–174, 1960.

Young, W. R., and P. B. Rhines, A theory of the wind-driven circulation II. gyres with western boundary layers., *Journal of Marine Research*, *40*, 849–872, 1982.